CFD Analysis of a Generic Inspection Robot within Crude Oil Pipelines

Guillermo Alonso Jimenez Alvarado

Submitted in accordance with the requirements for the degree of MPhil in Mechanical Engineering

The University of Leeds

School of Mechanical Engineering

August 2024

Intellectual Property and Publication Statements

The candidate confirms that the work submitted is his own and that appropriate credit has been given within the thesis where reference has been made to the work of others. This copy has been supplied on the understanding that it is copyright material and that no quotation from the thesis may be published without proper acknowledgement.

This work is dedicated to my beloved family,
for your constant love and support.

Acknowledgments

I would like to express my sincere gratitude to my supervisors, Dr Carl Gilkeson, Dr Natalie Gilkeson, Professor Richard Barker, and Dr Jordan Boyle.

I would also like to thank CONAHCYT for sponsoring me during the first four years of my studies.

This work was undertaken on ARC3 and ARC4, part of the High Performance Computing facilities at the University of Leeds, UK.

Abstract

Crude oil is a critical global energy resource, with pipelines being the primary mode of transportation. These pipelines require regular inspections to detect defects and ensure safe operations. The most common in-pipe inspection method is pigging, which consists of inserting a cylindrical device called Pipeline Inspection Gauge (PIG) that relies on blocking the flow to create a pressure difference, traverse the pipeline, and detect damages with sensors. However, PIGs have limited adaptability to varying pipe diameters and reduced manoeuvrability in complex configurations. Other alternative robotic platforms employ locomotion methods such as wheeled, tracked, or snake-like mechanisms. These offer greater adaptability but still depend on pipe walls, limiting their versatility. Therefore, this thesis explored the feasibility of a wall-independent self-propelled robot for non-destructive pipeline inspections, focusing on flow dynamics using Computational Fluid Dynamics (CFD) simulations.

Initial validation studies utilised CFD simulations to replicate prior experimental and computational results to ensure an accurate prediction of the drag coefficient and pressure distribution. Then, two CFD studies analysed the effects of pipe diameter, fluid viscosity, robot body geometry, and positioning. The first study investigated a spherical robot (0.2 m diameter) in five pipe diameters (0.508–1.0668 m) and six viscosities (0.001003–0.4 Pa·s). The second study evaluated the sphere from study 1 and three ellipsoids (lengths: 0.4 m, 0.6 m, and 0.8 m) and their vertical positions (centred, 0.1 m, and 0.2 m offsets) within a pipe (0.762 m diameter, 0.011 Pa·s viscosity).

The results of the first study showed that reducing pipe diameters and increasing viscosity both led to higher drag forces. The second study proved that elongating the robot reduces drag, with the 0.6 m ellipsoid achieving the lowest value. Additionally, positional offsets introduced lift forces, pushing shorter ellipsoids away from the wall while the sphere and longest ellipsoid

moved closer. These findings provide insights into designing stable, adaptable, wall-independent inspection robots for pipeline applications.

Table of Contents

List of Figures

List of Tables

Abbreviations

2D: Two-Dimensional

3D: Three-Dimensional

3RPS: 3 Revolute, Prismatic, and Spherical

3SPR: 3 Spherical, Prismatic, and Revolute

BR: Blockage ratio

CAD: Computer Aided Design

CFD: Computational Fluid Dynamics

DC: Direct Current

DOF: Degrees of Freedom

ECDA: External Corrosion Direct Assessment

EMAT: Electromagnetic Acoustic Transducer

ICDA: Internal Corrosion Direct Assessment

INI: In-line Inspections

LDV: Laser Doppler Velocimetry

LiPo: Lithium-ion Polymer

MFL: Magnetic Flux Leakage

NDT: Non-Destructive Testing

PIG: Pipeline Inspection Gauge

PM: Parallel Manipulator

SIMPLE: Semi-Implicit Method for Pressure Linked Equations

SST: Shear Stress Transport

UPVC: Unplasticized Polyvinyl Chloride

UT: Ultrasonic Testing

VAMP: Vacuum-actuated Muscle-inspired Pneumatic

Nomenclature

A: Cross-section area

A1, A2, A3: Pipe mesh for Chapter 4

a_x: Acceleration in the x-axis

C_d: Drag coefficient

C_l: Lift coefficient

C_p: Pressure coefficient

D: Pipe diameter

d: Sphere diameter

D1 - D5: Pipe name

E0 – E3: Ellipsoid name

E1.1 – E3.3: Ellipsoid mesh name

F_D: Drag force

F_x: Force in the x-axis

H0 – H2: Ellipsoid vertical position

k: Thermal conductivity of the fluid

l: Characteristic length

Ld: Distance from centre of the sphere to outlet

Lu: Distance from inlet to centre of the sphere

m: Mass

μ: Dynamic viscosity

μ1 - μ6: Viscosity name

ν: Kinematic viscosity

p: Pressure

P1 - P6: Pipe mesh for Chapter 3

R: Pipe radius

r: Sphere radius

Re: Reynolds number

Re_g: Reynolds number of the gap

Re_p: Reynolds number of the pipe

Re_s: Reynolds number of the sphere

ρ: Density

T: Temperature

T1, T2, T3: Tank mesh

t: Time

τ: Shear Stress

u, v, w: Local velocity components for the location

u: Centreline flow velocity behind the sphere.

U∞: Free stream velocity

V: upstream velocity

x, y, z: Cartesian coordinates

y+: Dimensionless wall distance

Chapter 1 Introduction

Oil may be one of the most important raw materials we have because we use it for many different purposes and because of it, it has become a cornerstone of our economy. Fossil fuels fulfil 80% of the energy demand, with oil and gas representing 50%-60% of that [1]. However, the resources of most of the giant oil fields in the world are shrinking because they are almost 50 years old [2]. Because of this, it has become necessary to look at reservoirs in extreme environmental conditions that represent new challenges to the environment and human lives [2]. Due this, transporting and distributing oil over long distances to where it is required is a major issue in the oil industry. The most common method to distribute oil is through pipelines, because it is the most safe, economical and efficient option [3]. Nevertheless, these pipelines can be affected by material and construction defects, mechanical damage, incorrect operation, corrosion, creep, cracking, malfunctions, and geological forces [4]. A method to find these defects before they cause a major problem is through in-pipe inspection robots. Currently, there are plenty of robots on the market that can inspect all kinds of pipe configurations. As a result, it might be possible to inspect an entire pipeline network. However, since most of these robots are designed for a very specific pipe configuration, and their ability to adapt to different conditions is limited, a wide variety of robots would be required to inspect the entire network. Therefore, inspections are a complex and infrequent event.

A solution to this issue might to design a robot whose locomotion does not depend on the pipe walls to perform its motion. The locomotion style that fulfils such characteristics is the propeller type. Nonetheless, the high viscosity of oil, and thus, low Reynolds number (Re) associated with the locomotion dynamics, increases the complexity of movement when using a propeller. This may be why, to the best of the author’s knowledge, there have been few

attempts to design an in-pipe inspection robot capable of navigating through oil pipelines through this locomotion method.

1.1 Aim

The aim of this research is to design an in-pipe robot able to carry out inspections inside pipelines by performing Non-Destructive Testing (NDT). Such a robot should have the ability to adapt and manoeuvre through a wide range of complex pipelines configurations such as vertical pipes, elbows, valves, reducers. By achieving this, in-line inspections could become a more frequent event, and it may be possible to increase the accuracy of the detection of current and future damage in the pipes. This will reduce the possible damage to the environment and the required personnel. Thus, by reducing the personnel, the inspection costs will also be reduced and the personnel safety will be increased.

In order to accomplish this, the propeller type has been chosen as locomotion method for the robot. Thus, the robot will not depend on the pipe walls to move and will be able to overcome a wider range of pipe configurations. Additionally, the robot should be autonomous to reduce the required personnel to carry out the inspections. This means that it should be capable of locating itself inside the pipeline and deciding the best approach to move towards its objective. It should be wireless to eliminate the limitation in the inspected distance because of the length of the cable. Moreover, the designed robot should be less intrusive than the current approaches. It will comply with requirements to work in explosive environments, so it will be able to carry out the inspection without stopping the production. By considering the points mentioned before, the robot should be able to overcome most of the obstacles presented in pipeline networks.

1.2 Scope of research

The anticipated contributions of this project span fundamental science, engineering design and the oil and gas industry, and are as follows:

1. Improving the fundamental scientific understanding of robotic movement through oil within confined pipelines.
2. Combining these findings to propose a new robot design for the purpose of inspecting pipelines in highly viscous fluids such as crude oil.
3. Proposing design considerations to enable new robots to function effectively within the unique environment inside oil pipelines.

1.3 Thesis Structure

This thesis is divided in 6 chapters. Firstly, Chapter 1 gives the introduction and aim of the project. Secondly, Chapter 2 is a literature review to further understand the state of the art and gaps in knowledge to which this project can contribute. Thirdly, Chapter 3 will validate and explain Computational Fluid Dynamics methods that will be used during this research. Fourthly, Chapter 4 will study the effects the pipe diameter and the viscosity have on the drag and pressure distribution. Then, Chapter 5 will study the effects the geometry and position of the robot. Finally, Chapter 6 will discuss the findings, recommendations, future work, and give a final conclusion.

Chapter 2 Background

In order to develop the expected robot, it is necessary to understand the state of the art of this field. Then, it may be possible to understand gaps to which this project attempts to contribute. This chapter will be divided into the following sections: Firstly, I will briefly explain the functioning of the oil industry, and how pipeline inspections are performed nowadays. Secondly, I will explain the fundamentals of fluid dynamics which are required to understand the problematic that self-propulsion presents at low Reynolds number (Re). Thirdly, I will explain how microorganisms swim at low Re and how micro-robots took inspiration from them. Finally, I will explain the fundamentals of computational fluid dynamics (CFD) which will be needed to understand the simulations that will be carried out in the following chapters.

2.1 Oil industry background

In the past decade there were approximately 330,000 km and 260,000 km of crude oil and production pipelines respectively [5]. The reason is that they are the safest, most economical, and efficient method to transport oil [3] [6]. However, these pipelines are not flawless, corrosion, cracking, construction defects, mechanical damage, incorrect operation, creep, and geological forces are some of the possible causes of pipeline failure [4]. Thus, causing a leak, and putting the environment and the population in danger. Therefore, to avoid a possible failure, it is essential to carry out inspections to ensure the perfect state of the pipelines.

2.1.1 Pipeline inspection

The purpose of inspections is to detect defects in pipelines before these cause the pipeline to fail. Examples of methods to detect this defects are: hydro-testing, where the pipes are filled with water, and pressure is monitored to detect pressure losses; external corrosion direct assessment (ECDA), where

sections in which external corrosion could be occurring are identified, to later carry out excavations to inspect pipelines directly; internal corrosion direct assessment (ICDA), where, similarly to ECDA, sections in which internal corrosion could be occurring are identified, to later perform excavations for direct inspections; and pigging, where a cylindrical device called PIG (pipeline inspection gauge) is inserted in the pipeline and, while pushed by the pressure of the fluid, detects damages using specialized sensors [4]. It is in this last method where the potential to improve inspections through robotics is.

Currently, PIGs are the principal instruments to maintain pipelines in optimal conditions, by cleaning and performing non-destructive inspection procedures inside the pipelines [6]. These pipelines require special traps for inserting, launching, receiving, and removing the PIGs (figure 2.1). These inspections follow certain standard process and considerations to increase the possibility of success [7]. The procedure to launch the PIG goes as follows:[1]

1. The main line trap valve must be closed, followed by the kicker trap valve (figure 2.1);
2. The PIG should be inserted in the launcher;
3. The kicker trap valve should be partially open;
4. The main line trap valve should be open;
5. The kicker trap valve should be completely open;
6. Finally, the main line bypass valve should be partially closed.

The procedure to receive the PIG goes as follows:

1. Receive the PIG;
2. The main line bypass valve should be open;
3. The main line trap valve and the bypass kicker/trap valve should be closed;
4. After the run, it is necessary to inspect the PIG to ensure that the sensors are not damaged to guarantee that the data obtained is reliable [7].

[1] Pipeline launcher and receiver animation (2010) YouTube video, added by T.D. Williamson [Online]. Available at https://www.youtube.com/watch?v=CDHtL-J1Xxo [Accessed 26 August 2024].

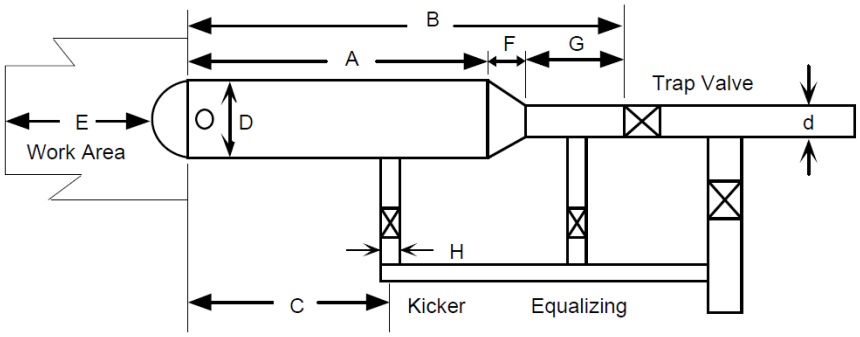

Figure 2.1 Diagram of a PIG trap (from [7]).

Despite the crucial purpose of PIGs, these devices are relatively simple, which makes their manufacture and usage extremely inexpensive compare to other types of robots. Nevertheless, there are several issues with these devices, for example, there is a minimum required flow rate, and the vibrations caused by the collision between sealing discs and girth welds during operation could lead to a failure in the PIG [8] [9]. Moreover, their major flaw may be their limited manoeuvrability and adaptability. Pipelines can have different configurations such as horizontal, vertical, elbow, t-section, valve, and diameter reducer which considerably hinder the PIGs ability to move through the pipelines, making them unpiggable [10]. These unppigable pipelines are estimated to represent only the 0.5% of the total, but they are the most important because they are above ground installations [10]. However, although inspections are essential to ensure the integrity of pipelines and avoid endangering the environment and population, such problems make the in-line inspections (INI) an infrequent event [6]. Therefore, the frequency and safety of pipeline inspections could be increased by developing a new robotic platform capable of manoeuvring through complex pipe configuration.

2.1.2 Design considerations

Nowadays, there are under development robots with a higher manoeuvrability capable of move though complex pipe configurations. However, these robots are still designed to work in specific environments and search for specific types

of defects. To ensure that the desired pipeline will be successfully inspected, when designing these robots it is necessary to take into account certain characteristics that describe the way they will interact with their environment. These are: propulsion mechanism, steering mechanism, shape and size mechanism, sensing technology, and control mechanism [2]. By understanding these characteristics of the robots currently under development, it may be possible to design a robot with a higher adaptability.

Propulsion Mechanism

The propulsion mechanism allows the robots to navigate inside the pipelines by the combination of a traction method and a locomotion method [10]. Traction methods are the ones used by the robot for gripping the pipe walls, such as gravity, wall-press, adhesion (magnetic or suction) and fluid flow [10]. One the other hand, the locomotion method refers to the strategy the robot will use to move inside the pipeline. The basic ones are PIG, wheeled, tracked, screw, walking, inchworm, snake, and propeller [2, 10]. The functioning, advantages and disadvantages of these locomotion methods will be further explain in Subchapter 2.1.3.

Steering Mechanism

The steering mechanism is responsible for allowing the robot to control its direction and move through more complex pipe configurations [2]. These mechanisms are divided in articulated, which allows the robot to steer using a pivot, and differential, which allows the robot to steer by making the different wheels or tracks go at distinct speeds relative to each other [2]. Some in-pipe robots, as PIGs, might not have a steering mechanism.

Shape and Size Mechanism

Depending on the pipe to be inspected, the required shape and size of the robots can vary. To allow the shape and size of the robot to change, and hence

adapt to a wider range of pipe geometries, two types of mechanism can be used. These are active linkage, which uses actuators to control the joints and press against the walls, and passive linkage, which uses elastic components to adapt to the diameter [2].

Sensing Mechanism

In order to detect and predict damages before they can cause an accident, inspection robots obtain information of the internal conditions of the pipelines through a variety of sensors. These sensors can be divided depending of the method, which refers to the technology that is being used, and the technique, which refers to the usage of such technology [7]. The methods are magnetic flux leakage (MFL), ultrasonic, eddy current, cameras, X-ray, geometry tools, and mapping tools [7].

Control Mechanism

The control mechanism is the method used to command the robot. It can be done through two methods: tethered cable or wireless. The first one, in addition to the data transmission, also can act as power supply and a safety rope [2]. However, the cables physically limit the distance and configurations the robot can pass through [2]. On the other hand, the second method has a wireless communication systems for data transmission, but it has the problem of being unable to penetrate a steel pipe wall and the robots would need to carry rechargeable batteries [2].

The previous parameters describe how in-pipe inspection robots interact with their environment. All the parameters are important and should be taken into account to a certain extent when designing a robot. However, as mentioned before, the biggest flaw of current in-pipe inspection robots may be their limited adaptability and manoeuvrability. Therefore, identifying a method to improve the propulsion mechanism, and thus, the traction and locomotion methods was one of the objectives of this project.

2.1.3 Inspection robots

In-pipe inspection robots currently being used or in development can be divided by their locomotion method. These methods are: PIG, wheeled, tracked, screw, walking, inchworm, snake, propeller and hybrids [10]. Except for propeller type, where no in-pipe inspection robots were found for oil pipelines, several examples of each locomotion methods will be reviewed in this section. Thus, it will be possible to identify the advantages and disadvantages of each method.

PIGs

PIG type robots have a cylindrical shape with a diameter large enough to block the pipe, they are unable to control their own movement direction, and instead are controlled by the pressure difference of a liquid [11]. Therefore, this type perform poorly in low pressure pipes and pipes with complex configurations [12]. However, the fact that they do not use active propulsion, steering, shape and size, and control mechanisms, reduces considerably their manufacturing costs. Thus, instead of increasing their capabilities, the trend in new PIGs seems to be to simplify them even more. For example, creating low-cost inspection PIGs by combining cleaning PIGs with inspection technology [6, 13-15]. Cleaning PIGs have no sensors, they are smaller than inspection PIGs, and they are used before inspections to clean the pipes, so their bigger counterparts will not get stuck. Thus, when compared with inspection PIGs, cleaning PIGs are less intrusive with the operations and can be run by operators [15].

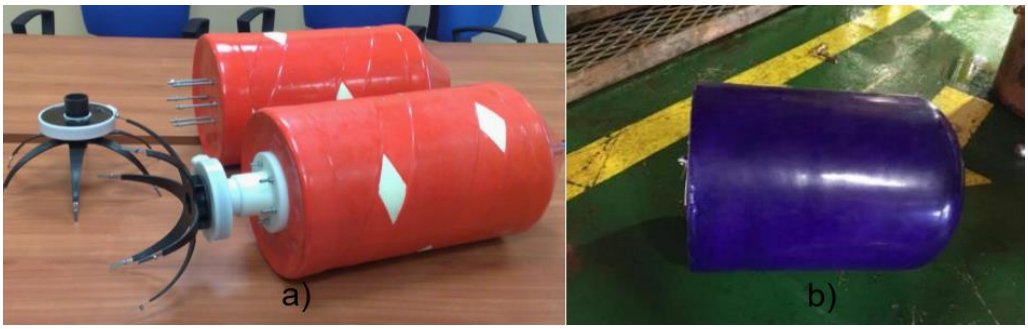

Figure 2.2 Examples of low cost PIGs. a) Low-cost foam PIGs with a six arms calliper (From [6]). b) Cleaning PIG (From [15]).

In [6] [13] a low-cost PIG was developed to clean and inspect at the same time thanks to the inclusion of a calliper (figure 2.2a). The calliper had six arms whose bending was detected by foil strain gauges, which can measure deformation by a relationship between the strain gauges response and the arm bending. Tests showed that it was possible to detect pipe characteristics such as curves, T-junctions, changes in diameters, and defects as obstructions and cracks. However, a drawback found was that the temperature affects the response of the strain gauges. Another example can be seen in [14], where cleaning PIGs were equipped with temperature, pressure and acceleration sensors to detect zones where wax accumulates. With the data given by acceleration sensor it was possible to know when the PIG stopped, and such stops were attributed to an accumulation of wax. In addition, with the pressure sensors it was possible to know the amount of accumulated wax, because in the case of large amount of deposits, the pressure would considerably increase. A final example of this approach is the design of smart sensors that could be mountable in cleaning PIGs (figure 2.2b) [15]. The idea was to create a standard cleaning PIG with enough space to mount sensors that utilised the eddy current technology to detect defects.

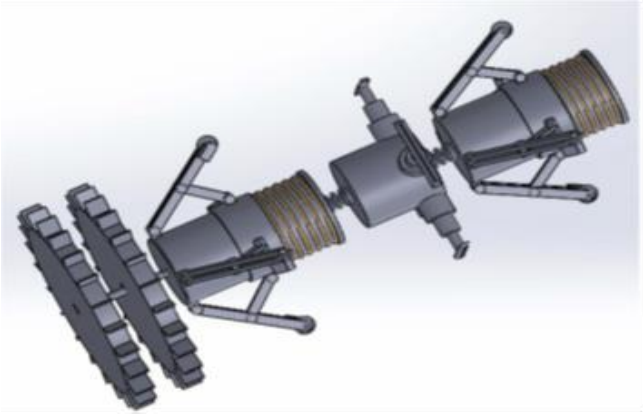

Figure 2.3 PIG with a modular structure (From [16]).

A different approach was followed in [16], where a 3D model of a PIG capable of adapting to different pipe diameters was designed (figure 2.3). The model has three units, and was designed to clean and inspect pipelines with diameters from 6” to 14”. The first unit has four wall-pressing arms that can

vary their length, and a DC motor that rotates the cleaning brushes mounted on the front. Then, the middle unit has four arms with ultrasonic sensors to detect defects. Finally, the back unit has four wall-pressing arms and it is used to store the batteries. Despite the increased adaptability to different pipe diameters, this is still limited to diameters must be between 6” and 14”. Furthermore, the prototype does not include a steering mechanism navigating at will inside the pipeline.

Despite the limitations in their manoeuvrability, PIGs are still the most used type because of their relatively low cost of production. This may be why, rather than reducing the limitations of the PIG type, they were more interested in improving its advantage (low cost) by using improved cleaning PIGs [6, 13-15]. Such cleaning PIGs include less advanced sensors than inspection PIGs. None of them attempted to solve the problem of manoeuvrability, and only [16] attempted to increase the adaptability to different diameters. Nonetheless, this allows them to maintain the cleaning PIGs cheaper, smaller, and easier to handle and carry out inspections.

Wheeled type

Wheeled type, as its name indicates, use wheels to move inside pipelines. Because of its ability to be combined with other locomotion and traction methods, this is the most commonly used method when trying to increase the manoeuvrability of in-pipe inspection robots [10]. A common design for this type is the tri-legged, which is more adaptable and has better traction compared to other wheeled designs [17, 18]. In [17, 18] the designed robots have three legs connected to the main body (figure 2.4a). In both cases, each leg has two wheels and its own motor and, by controlling their speed independently, it is possible to move through complex pipe configurations. In these, two and many other examples of tri-legged robots the main difference is the mechanism used to control the traction and length of the legs. In [17] a scissor mechanism was used that, when tested, was shown to be able to move through a horizontal pipe with a diameter of 12”, and a vertical pipe with a diameter of 8”. On the other hand, in [18] the robot has a flexible clutch

mechanism that can be adjusted to move through pipelines with diameters between 450 to 575 mm.

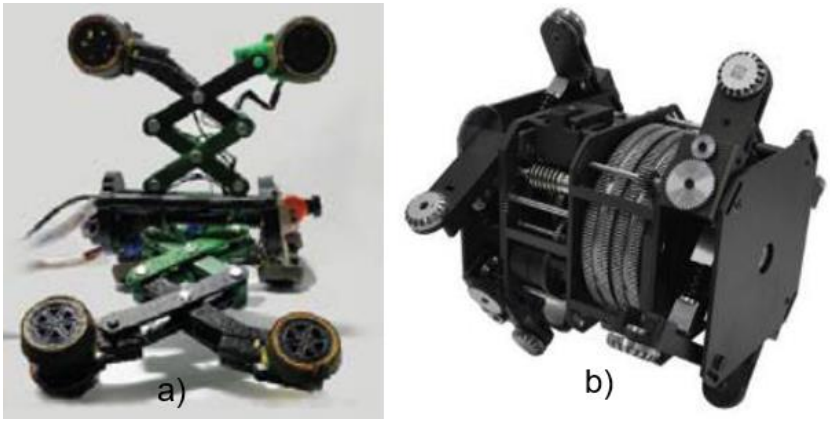

Figure 2.4 Examples of wheeled in-pipe inspection robots. a) Tri-legged robot with a scissor mechanism (from [17]). b) MRINPECT VI++ robot with the wheels unfolded (Adapted from [19]).

A completely different and more interesting approach was followed in [19], where it was designed a robot named MRINSPECT VI++ (figure 2.4b). The robot has a front and a rear section, each one with four wheels. The innovation of this robot is that, through a series of gears, the wheels can rotate at different speeds between them. As a result, the entire robot can be controlled by just one actuator. Additionally, the robot has an adhesion section composed of an adhesion mechanism and a rescue mechanism. The first one can change the reach of the wheel mechanism to adapt to different diameters. Moreover, the second one can release the lock of the wheels to reduce the size of the robot so it can be pull out.

As shown in the previous examples, the robots with this locomotion method have a higher manoeuvrability and adaptability when compared to PIGs. They have mechanisms that allow them to control the length of their legs, and they can control their direction by moving their wheels at different speeds. Nevertheless, the disadvantage of these robots is the higher complexity of its steering mechanism when compared to PIGs and, despite this increased complexity, they are unable to overcome sharp corners and changes of diameter if the transitions are not smooth [2].

Tracked type

Tracked locomotion is similar to wheeled locomotion but tracks provide more traction, gives a better payload capacity, are more stable, and more suitable for rough surfaces when compared to the wheeled locomotion [10] [20]. For example, a tracked robot was designed for pipelines made of UPVC with an inner diameter of 14” [21]. The robot is very simple and only consist of a chassis with tracks and sensors. It is expected to inspect and clean pipes, with the main advantage of being cheaper than the other options on the market. However, during the experiments only the locomotion system was tested, where it was shown to be able to pass through horizontal pipelines and pipelines with an inclination of 30°. Another example of the tracked is a robot with a similar three-legged structure that the ones observed in the wheeled section (figure 2.5a) [22]. It consists of a main body, and three 3-bar belt powered chains each one with a tracked crawler. Each track can be controlled independently to navigate through the pipeline. Additionally, each belt-powered chain has a motor that controls the linkage clutch mechanism to vary the diameter between 30 and 45 cm. A final example of the tracked type is the robot in [23], which consists of several modules arranged linearly (figure 2.5b). The modules have flexible connections to attach them to each other and tracks that can be extended. The innovation of this design is not in the locomotion method, but in its modular design. These modules can be mobilized separately and assemble at the inspection site. To carry out inspections the robot uses an ultrasonic testing (UT) electromagnetic acoustic transducer (EMAT), high-definition cameras for visual inspection, and an umbilical cord to transmit information in real time.

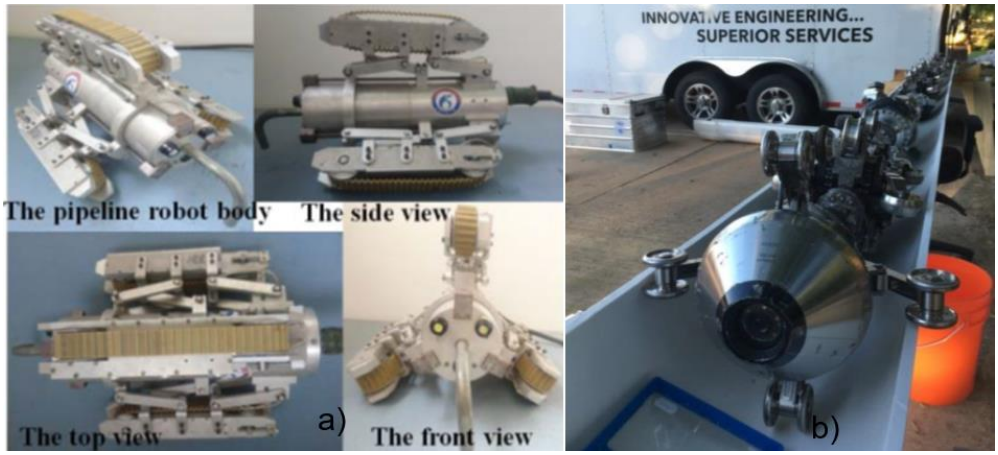

Figure 2.5 Examples of tracked type robots. a) Tracked robot with a tri-legged mechanism (from [22]). b) Modular tracked robot (without the tracks) (From [23]).

Both wheeled and tracked types showed similar designs with great adaptability. By using differential driving, both types can handle relatively complex pipe configurations. Furthermore, by using wall-press mechanisms to push their wheels or tracks against the walls to adapt to various diameters and generate traction, with the difference that tracked types can generate a higher traction. However, as mentioned before, the variation of the diameter is limited by the mechanism, and this makes them unable to overcome sudden changes of diameter and sharp corners [2].

Screw type

Screw type robots are composed of a front and a rear section. The front section of these robots has a rotor and wheels at a certain angle to move like a screw (figure 2.6) [10]. The advantages of this type are that it only requires one actuator to generate forward movement and is difficult to be pushed back for the flow [10, 24]. Nevertheless, the main drawback of this type is that it has no steering mechanism, which makes it unsuitable for complex pipe configurations [2]. Two examples of this type can be seen in [25, 26]. The first one is a basic design of a screw type robot (figure 2.6a). It has a fore leg system with a motor and a rotor connected to the three legs, each leg with a wheel at the end at an angle of 15° to generate forward motion. While the rear

legs are kept straight to perform linear movement. The robot is designed to move through straight pipes, elbows, and reducers, with diameters between 230 mm and 300 mm. Furthermore, a prototype was manufactured and was able to move at a speed of 0.1262 m/s. The second example has four supporting arms to move through obstacles, and each one has a force sensor at the end to feed the control system (figure 2.6b). This system controls a motor to adjust the extension of the arms. During the experiments, the robot was tested in a pipe with an outer diameter of 127 mm. In such experiments, it was shown to have a maximum traction force of 1620 N. However, the robot was not tested in pipes with complex configurations.

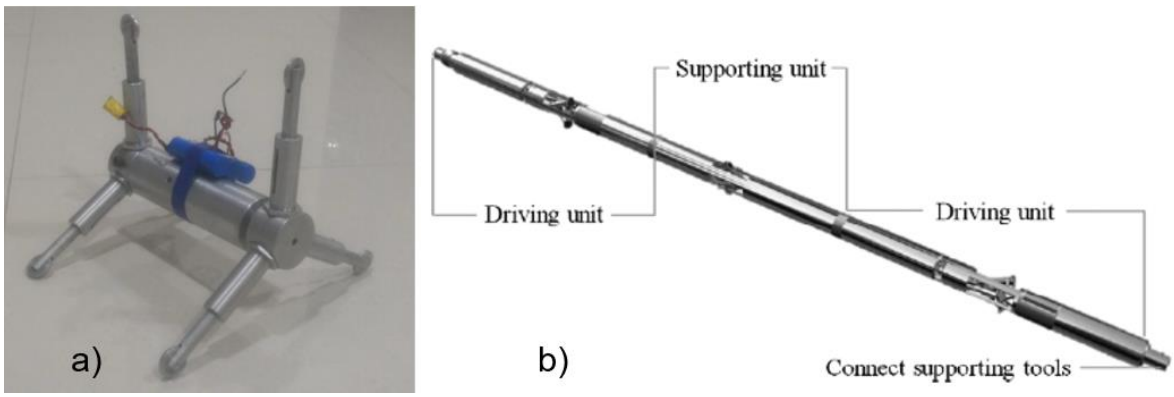

Figure 2.6 Examples of screw type locomotion. a) Screw-type robot designed to inspect pipelines (From [25]). b) Self-balancing in-pipe robot. The driving units contain the driving wheels, two motors, and a planetary gear. The supporting unit includes the supporting arms and the fore sensors. (From [26]).

When compared to wheeled and tracked types, screw type showed more limitations like only being capable of moving forwards and at a lower speed. However, their design gives them a great traction and stability, and allows them to generate motion with only one actuator.

Walking type

Walking type uses legs to press against the walls and move. This type has the required adaptability to pass through obstacles, but the legs have a high number of DOF that increase the complexity of the structure and movement

[20]. Examples of this type can be seen in [27-30]. In [27] the 3D modelled robot is a 3SPR/3RPS-type (spherical, prismatic, and revolute) parallel manipulator (PM) (figure 2.7a). When the mechanism moves forwards it becomes 3SPR and when it does backwards it becomes 3RPS. The robot has 6 legs each one with 1 DOF and two holes to connect different toes. Those toes can be used to increase the length of the legs and adapt to different diameters. Therefore, by changing the toes it is possible to increase the friction with the walls and increase the load carrying capacity. However, these changes need to be done manually, making it impossible for the robot to adapt while is inside the pipe. Additionally, the several legs and DOF considerably increase the complexity of the robot.

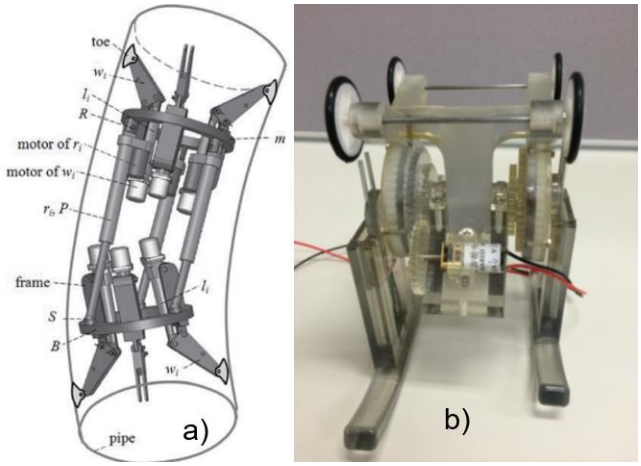

Figure 2.7 a) CAD design of a 3SPR/3RPS-type robot inside a pipe (From [27]). b) Prototype of a walking robot manufactured using Vero Clear as a material (From [28]).

Certainly, the complexity of the walking type designs can be reduced. However, this also reduces their mobility. For example, the robot in [28] consists of three sections: supporting unit, driving unit, and walking unit (figure 2.7b). The supporting unit on the top of the robot has four wheels connected to a platform, which at the same time is connected to the driving unit through a spring. Such spring is the mechanism by which the robot can adjust to different pipe diameters. The driving unit has a motor and fourteen gears that transmits the motion to two axes. The walking unit consists of two planetary gears that move two legs. The main issue with this design is that the robot

cannot move through vertical pipelines because the springs and wheels cannot create enough friction with the pipe-wall. Another example of a simplified walking robot can be seen in [29], where a two-wheg miniature climbing robot called ORION-III was proposed (figure 2.8a). The robot has two whegs each one with four legs with an adhesive layer, and a tail helps to reduce the torque requirements for transitions. A final example is the one proposed in [30], which is the design of a robot with a fluidic control system (figure 2.8b). The robot has a circuit that is a two-state machine with a fluidic NOT gate, a fluidic NAND gate, a normally closed gate, and uses three pneumatic lines: vacuum, clock, and control. By alternating the clock and the input between high and low, it is possible to control the movement of the robot. However, instead of a fully designed robot, this is rather a proof of concept to avoid the risk of ignition in oil and gas environments.

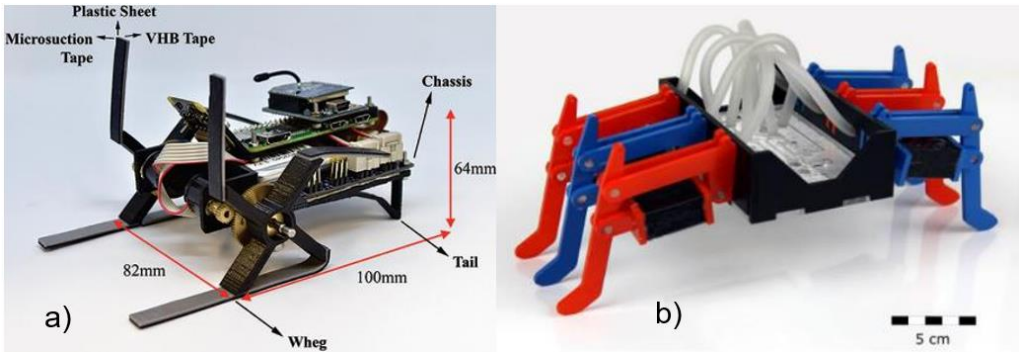

Figure 2.8 a) ORION-III prototype (From [29]). b) Walking robot with a fluidic control system. The circuit is a two-state machine with a fluidic NOT gate, a fluidic NAND gate, and a normally closed gate (From [30]).

In the case of the walking type, it seems to be necessary to find the equilibrium between mobility and complexity. The design of the 3SPR/3RPS-type robot [27] seems to have a great adaptability to the different obstacles that could be encountered in a pipeline. However, the design and control is rather complex. On the other hand, the robots presented in [28], [29], [30] were simpler in design but their mobility was reduced.

Inchworm type

Inchworm is a limbless locomotion method that imitates the peristaltic movement of earthworms to generate motion. Robots with this locomotion method need certain flexibility in their structure, so it is common for this type to use soft materials. Moreover, some of these robots do not have electrical components, and use pneumatic components instead, making them safer to be use in explosive environments [2]. Examples of soft robots can be seen in [31, 32]. These robots consists of several sections that can be pressurized independently through several pneumatic control channels. As a result, these robots move by performing a sequence of inflating and deflating the different sections of themselves to emulate the peristaltic movement of the earthworms.

Although, the forward movement of these robots follows the same sequence, depending on the number and location of the chambers it is possible to achieve movements that are more complex. For example, in [31] the soft robot called VAMP (vacuum-actuated muscle-inspired pneumatic structure) consists of three sections: two ring-shaped positive-pressure pneumatic actuators, one at the top and one at the bottom, and a middle section called VAMP (figure 2.9a). This structure allows the robot to adapt to pipe diameters between 60 and 64 mm by expanding the top and bottom sections. In another example, in [32] was designed a soft robot with an extension module consisting of three chambers parallel to each other, and two clampers which function is to stick to the walls (figure 2.9b). If a chamber expands while the other two stay the same, the head will bend to the opposite direction of the expanded chamber. Thus, it is possible to control the direction of the head of the robot.

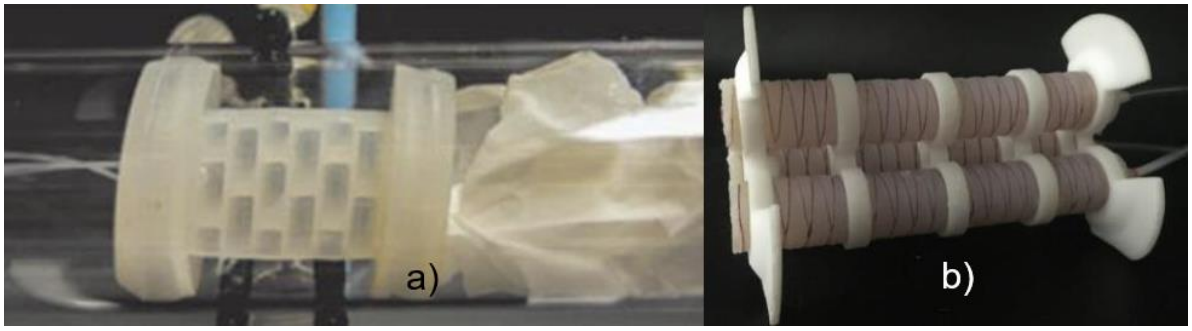

Figure 2.9 Soft inchworm robots. a) VAMP moving through a pipe while removing a tissue paper (adapted from [31]). b) Worm-like soft robot with three chambers and two clampers (from [32]).

Nonetheless, not all the inchworm type robots are made with soft materials. The robot in [33] has a series of cylindrical modules connected to each other by universal joints, and performs inchworm locomotion by a combination of gripping mechanisms and linear actuators (figure 2.10a). The robot is connected to the user through a tether cable for power supply and for communication. Another example is in [34], where the robot has three compliant modules connected by passive joints (figure 2.10b). Each module has chain-sprocket power transmission pairs to generate motion and two active hinge joints to achieve the module compliance.

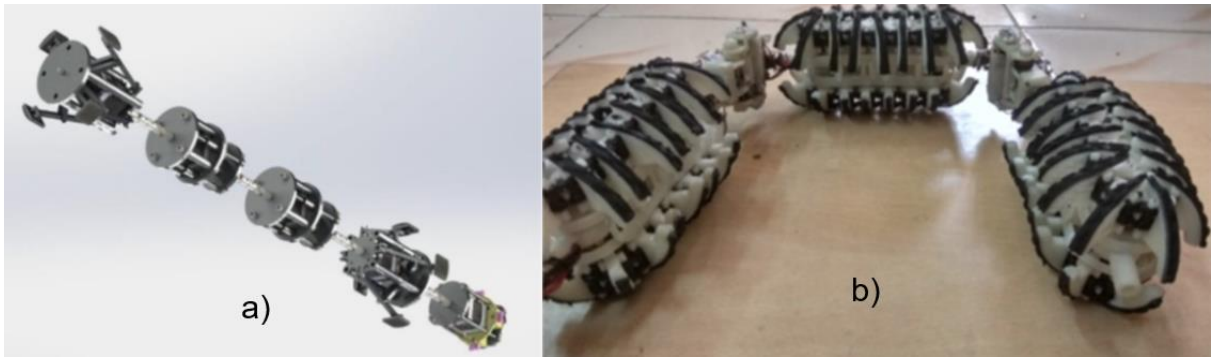

Figure 2.10 Hard inchworm robots. a) CAD model of the inchworm type modular robot (from [33]). b) The OmniCrawler robot consisting of three modules (from [34]).

Inchworm type robots could be divided into soft robots and hard robots. The main advantage of the soft robots in [31] and [32] is their lack of electronic components, which makes them capable of working in explosive

environments. This should allow them to carry out inspections in oil pipelines without stopping the product flow. Nevertheless, the need of a tethered cable for air supply makes this impossible because an opening would be needed for the cables to exit to an external pump. The hard robot in [34] avoids this problem of needing a tethered cable, but it has the disadvantage that all the inchworm type robots have, which is their low speed. Such low speed would make impossible for these robots to inspect a pipeline of several kilometres in a reasonable amount of time.

Snake type

Inspired by snakes, these robots are composed of various modules joined by articulations to imitate their locomotion [35]. Some of these robots move using contact forces by pressing their modules against the walls of the pipes [36]. These robots use concertina locomotion to navigate through the pipes. In this locomotion, the snake firstly pushes the rear section of its body against the wall, and moves the front section of its body. Then, the snake pushes the front section of its body against the wall, and contracts the rear section [37].

An example of a snake type robot is in figure 2.11a. This robot is called SniPE and consists of 11 spherical links, each one with a microcontroller to control the servomotor and detect its position [36]. Additionally, the rear link has a microcontroller in a master position that controls the motion through a potential field method. In summary, this control method generates potential functions which create an attractive filed in the desired positions, and a repulsive field in obstacles that need to be avoided. Then, the master microcontroller sends the required positions to the microcontrollers in the links. Another example of this type of snake robots can be seen in [38]. The innovation of this robot is that each module includes a translational joint, in addition to the rotational joint most snake robots have [38]. When the robot performs concertina locomotion, while the rear part of the body is pushing against the wall, the translational joints of the middle part extent to increase the travelled distance.

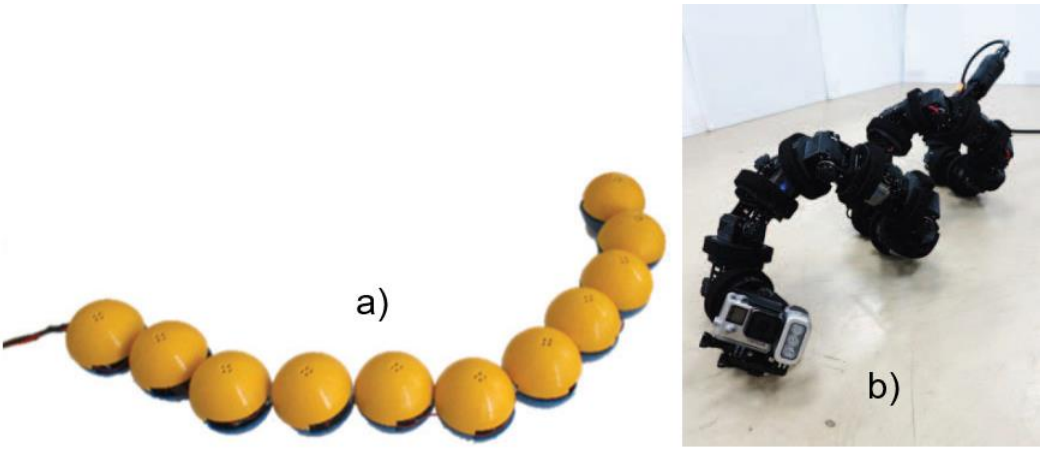

Figure 2.11 Snake type robots. a) Full body of the SniPE robot with the modules covered (from [36]). b) Prototype of a snake robot performing helical motion (From [39]).

A different type of snake robots has wheels on the modules. These robots move through horizontal pipes like a normal wheeled type, but in the case of vertical pipes they use their articulations to push against opposite walls to generate motion [12]. For example, the robot called Slyder consists of ten modules, each one with servomotors and wheels to reduce the friction with walls when inspecting square shaped ducts [40]. On the other hand, a different approach to motion was followed by the robot in figure 2.11b. This robot consists of 20 modules connected through yaw and pitch joints [39]. These joints are used to adopt a helical shape, and then, the robot moves by performing a helical movement.

As seen in literature, snake type robots have the ability to perform different types of motion which confers them a high adaptability to the environment. Moreover, they can adapt to different diameters by controlling the number of modules in contact with the wall. Nonetheless, to achieve such adaptability each joint must be able to move independently. Thus, these robots required more actuators and, as a result, they are less energy efficient [12]. However, the biggest challenge for snake type robots may be their control. At all times the software requires to know the shape of the pipe, and the position of each module relative to such pipe. Therefore, it can decide the best course of action, and execute it.

Hybrids

Hybrid robots combine different locomotion methods to overcome their individual limitations, and increase the overall versatility of the inspection robots. For example, the robot in figure 2.12 combines tracked and PIG types [41]. It has two traction modules with three tracks and a mechanism to vary the length for different diameters. Additionally, it has a return mechanism with gates that can be closed to block the flow like a PIG. Thus, it can be pushed back when going against the flow. In this case, the combination of PIG and tracked allows the robot to travel passively and save energy like a PIG, and to adapt to a change in diameter by extending the track's mechanism. However, as in other tracked robots, this change in diameter is still limited by the mechanism used to control the extension of the tracks. Furthermore, if the diameter changes considerably, the PIG method may lose efficiency as it requires to block the flow to work. Another example is the robot in figure 2.13 combines snake and inchworm types to inspect gas pipelines [42]. The robot has a front and rear block connected through a joint that allows the robot to turn. Each block has a frame with legs that can move forward and backwards to generate motion, and each leg has a wheel that can lock and unlock. Therefore, the robot can move by performing a sequence that imitates the peristaltic movement of earthworms. However, despite its increased versatility thanks to the inclusion of the joint, this robot has a slow displacement velocity as other inchworm type. Additionally, despite the fact that the locking mechanism of the legs allows the robot to adapt to different diameter, this adaptability is limited.

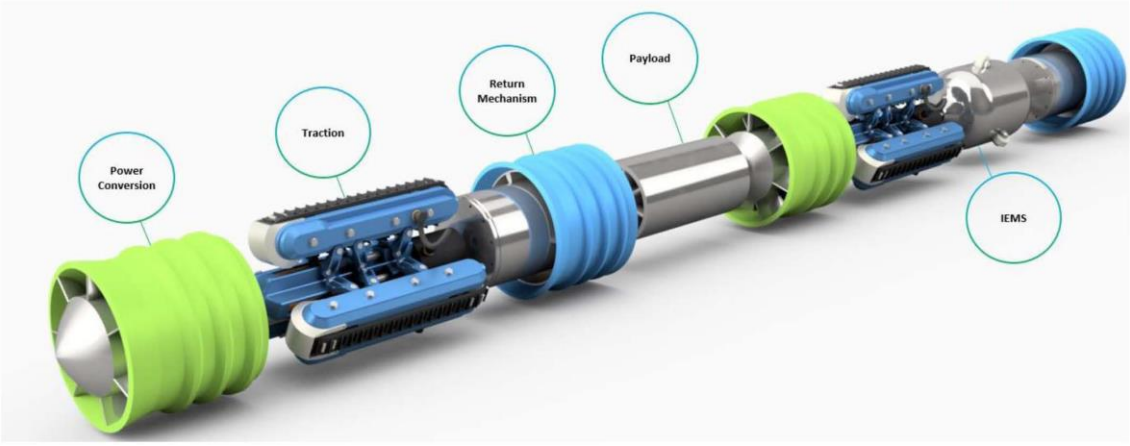

Figure 2.12 Illustration of a modular hybrid robot that combines tracked and PIG type (From [41]).

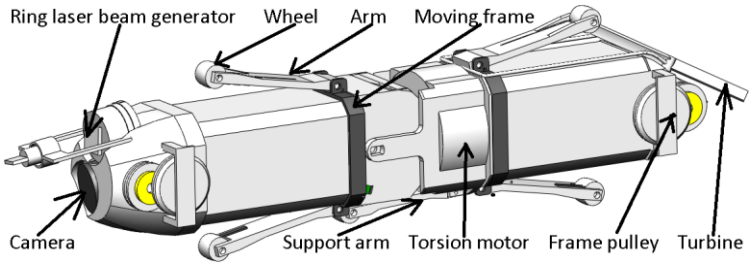

Figure 2.13 In-pipe inspection robot for gas pipelines that combines snake type and inchworm type locomotion (From [42]).

Despite the limitations of the basic locomotion methods, most of the designs previously reviewed completely rely in one of them. This is because most in-pipe inspection robots are designed for specific pipelines and situations. Due to this specific design approach, several robots are necessary to inspect an entire pipeline network. As a result, the complexity and cost of the inspections are increased. Nonetheless, by combining different locomotion methods, one can create a hybrid robot that will perform better than the original ones in a greater variety of pipe configurations [24]. Therefore, increasing the efficiency of pipeline inspections. However, as seen in the examples given here, hybrid robots still have a limited adaptability to a change in diameter. The solution may be to design a robot with a locomotion method that does not depend on the pipe walls. Thus, making the diameter of the pipe irrelevant for the locomotion.

Propeller type

Propeller or swimming type robots have mechanisms that allow them to use the fluid to generate motion, such as turbines or fins. This locomotion method is the most unusual for in-pipe inspection robots [10]. The advantage of these robots is that they do not need to contact walls to generate motion, making them able to move in different pipe diameters and configurations [10]. All in-pipe inspection robots with propeller type locomotion found were designed to inspect water pipelines. Examples of such robots are figures 2.14a and 2.14b [43, 44]. This last one has an oval shape with two ducts on the front, each duct containing a thruster that can be controlled independently [45]. Furthermore, thanks to its design, the buoyancy and gravity forces cancel each other. Thus, it is not required to control the movement in the z-axis. On the other hand, the design in figure 2.14a has a modular design, where each cubic module has a thruster on each face from where the water can flow in every direction [43]. When several modules are connected the thrusters align with each other, and the robot propels itself by [43]. However, this is more of a proof of concept than an actual attempt to design an inspection robot.

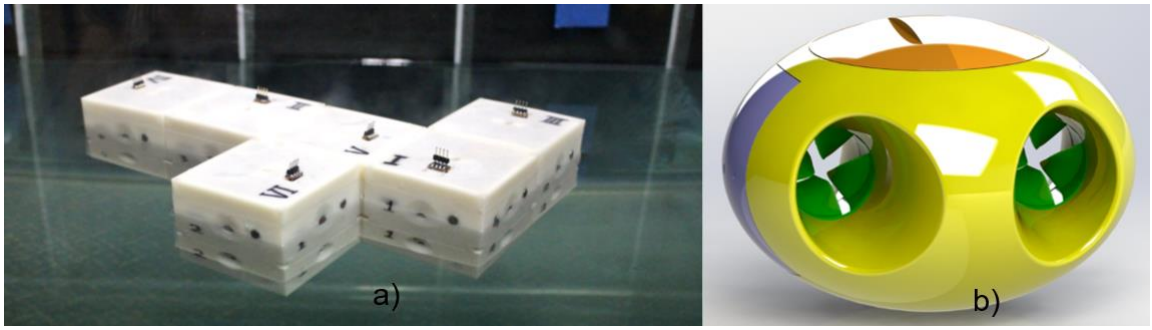

Figure 2.14 Propeller type robots. a) Prototype of a 2D modular robot with 6 modules (from [43]). b) Propeller type robot with two thrusters (from [44]).

Conventional locomotion methods and their combinations have shown to be able to satisfactory adapt to complex pipe configurations except to considerable increases in diameter. Propeller type locomotion may be the solution to this issue, either as the only method of locomotion or combined with another. By not using the walls, propeller or swimming type can manoeuvre through pipelines with any diameter as long as the robot is small enough to fit.

Thus, it may be possible to design a robot capable of inspecting any oil pipeline. Nevertheless, it is important to make a remark. Previous locomotion methods were relying on the pipe walls to generate traction and move. Thus, it was not relevant what fluid was flowing through the pipeline. And in the case of the two propeller type examples given here, they were designed to work in water. However, the purpose of this project was to create a robot to inspect pipelines carrying crude oil. The different properties of crude oil, in particular the high viscosity, makes it more difficult to achieve propulsion by reciprocal motion (the reasons for this will be further expanded in Subchapter 2.2). This might be the reason why, to our knowledge, no propeller type robot has been designed for the in-pipe inspection of oil pipelines.

2.2 Physics background

To design a propeller type robot capable of navigating inside oil pipelines, it is important to first understand the properties of the fluid and how higher viscosity affects the underlying physics. The discipline of fluid dynamics is extensive and to fully explain it would require more than this section. Therefore, for the purpose of this thesis, this section will only address the properties of a highly viscous fluids like crude oil, and how these affect the dynamics of bodies inside such fluids. Furthermore, these properties are required to understand the governing equations of fluid dynamics. These equations are a fundamental part of Computational Fluid Dynamics (CFD). CFD will be further explained in Subchapter 2.4, since it plays a key role in this research. Unless otherwise stated, the information in Subchapter 2.2.1 was taken from the book “Mechanics of Fluid” by B. S. Massey [46], and information in Subchapter 2.2.2 from “Computational Fluid Dynamics A Practical Approach” by Tu, J. [47]

2.2.1 Properties of Fluids

A fluid is a substance that cannot resist shear forces, and if these are applied to it, its shape will change. Or to say it in another way, it will flow. There are three properties of fluids that need to be taken into account. The first property

is density represented by ρ (rho) and measures the mass per unit of volume. The second property is pressure represented by the letter p. Pressure results from the constant collision of the molecules of the fluid with each other and with the molecules of external boundaries. Thus, exerting a force against the walls of these boundaries. Pressure cannot be directly measured and what is usually measured is a difference between the pressure of the fluid and an external pressure. The third property is the dynamic viscosity, or just viscosity, and is represented by μ (mu). When a force applied to a fluid makes a layer of this fluid to move relative to another layer, there will be an opposing frictional force to this movement called viscosity. Therefore, viscosity is the resistance of a fluid to flow. It is caused by the friction of the molecules of the fluid. This is given by the formula

$$\tau = \mu \frac{\partial u}{\partial y} \quad (1)$$

When solving problems involving viscosity, a common relation is the ratio of viscosity to density, which is called kinematic viscosity. It is given by the formula

$$\nu = \frac{\mu}{\rho} \quad (2)$$

Where ν (nu) is the kinematic viscosity. A consequence of viscosity that must be mentioned is the non-slip condition. This is, if there is a flow in contact with a solid boundary and the velocity of this flow is measured, then the closer the measured point is to the boundary, the slower the flow is. Where the particles that are in direct contact with the boundary have a velocity of zero. This area close to the boundary where this effect becomes significant is called boundary layer.

Finally, there are several classifications of fluid flows, but the one that will be useful throughout this explanation is whether the flow is laminar or turbulent. In laminar flow, the viscous forces dominate over the inertial forces, thus the fluid particles move in a relatively straight line (no turbulence). In contrast, in turbulent flow the inertial forces are more important than the viscous forces, thus the fluid particles have an erratic movement. It is possible to know the rime of a flow through the concept of Reynolds number (Re). This number

represents the ratio of inertial forces to viscous forces of the flow. It is calculated with the formula

$$Re = \frac{\rho l u}{\mu} \quad (3)$$

Where ρ (rho) is the density of the fluid, l is the characteristic length, u is the velocity, and μ is the viscosity. The numerator represents the inertial force and the denominator represents the viscous force. If Re < 2000, then the flow would be laminar. On the other hand, if Re > 4000, then the flow would be turbulent. Additionally, if 2000 < Re < 4000, this flow would be transitional, and it would show characteristics of both laminar and turbulent.

2.2.2 Governing Equations of Fluid Dynamics

The behaviour of a fluid flow can be described by three equations known as the governing equations of fluid dynamics. Firstly, the continuity equation is based on the concept of conservation of mass, which states that matter cannot be created nor destroyed. If this concept is applied to a fluid flowing through a pipe. It means that, if an arbitrary section of the pipe is chosen, then the mass that enters in this section, plus the mass that is being accumulated inside should be equal to the mass that leaves.

This principle is expressed in the following equation in its Cartesian form for three-dimensional flows:

$$\frac{\partial u}{\partial x} + \frac{\partial v}{\partial y} + \frac{\partial w}{\partial z} = 0 \quad (4)$$

Where u, v, w are the local velocity components for the location (x, y, z) and time (t).

The second equation is the momentum equation also known as the Navier-Stokes Equations. This equation is an adaptation for fluids of Newton's second law.

$$\sum F_x = m a_x \qquad (5)$$

In the case of fluids the F_x term is represented by body and surface forces. The first one refers to external forces such as gravity and electromagnetic. The

second type refers to the normal and tangential stresses caused by pressure and viscosity. The former formula need to be applied to the three Cartesian coordinates. But, since the purpose of this section is only to explain the concept behind the equation, it is only going to be consider a two-dimensional flow for the sake of simplicity. Therefore, the momentum equation in its Cartesian form for a two dimensional flow is:

$$\frac{\partial u}{\partial t} + u\frac{\partial u}{\partial x} + v\frac{\partial u}{\partial y} = -\frac{1}{\rho}\frac{\partial p}{\partial x} + v\frac{\partial^2 u}{\partial x^2} + v\frac{\partial^2 u}{\partial y^2} \quad (6)$$

Where $\frac{\partial u}{\partial t}$ is the local acceleration, $u\frac{\partial u}{\partial t} + v\frac{\partial u}{\partial y}$ is the advection, $\frac{1}{\rho}\frac{\partial p}{\partial x}$ is the pressure gradient, and $v\frac{\partial^2 u}{\partial x^2} + v\frac{\partial^2 u}{\partial y^2}$ is the diffusion. Where the terms advection and diffusion respectively mean the motion of a substance as a whole, and the movement of particles from a concentrated zone to a less concentrated one.

The third equation is the energy equation. This is based on the first law of thermodynamics which states that energy cannot be created nor destroyed. In fluids the energy is composed by the internal energy, the kinetic energy, and the gravitational potential energy. The simplified energy equation for a two-dimensional flow is:

$$\frac{\partial T}{\partial t} + u\frac{\partial T}{\partial x} + v\frac{\partial T}{\partial y} = \frac{k}{\rho C_p}\frac{\partial^2 T}{\partial x^2} + \frac{k}{\rho C_p}\frac{\partial^2 T}{\partial y^2} \quad (7)$$

Where $\frac{\partial T}{\partial t}$ represents the local acceleration, $u\frac{\partial T}{\partial x} + v\frac{\partial T}{\partial y}$ is the advection, and $\frac{k}{\rho C_p}\frac{\partial^2 T}{\partial x^2} + \frac{k}{\rho C_p}\frac{\partial^2 T}{\partial y^2}$ is the diffusion.

2.2.3 Scallop Theorem

The Scallop theorem formulated by Purcell in 1977 [48]. This theorem explains that, since at low Re (Re << 1) the inertial forces become negligible, and only the viscous forces remain, the time becomes irrelevant. Moreover, in the equations that describe the motion of fluids called the Navier-Stoke equations the term for time disappears from the equation. As a consequence, swimming by reciprocal motion becomes impossible. In order to swim at low Re, it is necessary to perform a movement that is asymmetric in time. This concept

may explain why propellers become less efficient as the Re decreases, and how would a propeller behave at low Re.

2.3 Micro-swimmers

Preliminary calculations show that thanks to the high viscosity of oil, the robot designed here will potentially have a Re < 500. This Re is considerably higher than what is normally considered a low Re (Re << 1), but it is equally lower than the Re of a macro-swimmer in water (Re >> 1000). As a result, it may be necessary to study both to have a complete picture of the field. The physics of swimming at high Re are well known because is how macroscopic everyday swimming works. Nevertheless, swimming at low Re is slightly different as previously pointed out. The most common type of creatures that can swim at low Re are microorganisms. Because of their small size and velocity, microorganisms experience Re < 0.01 [49]. Therefore, studying microorganisms may help to understand the effect of a highly viscous fluid in the swimming performance.

2.3.1 Biological background

An object must measure around 100 μm to be visible to the naked eye [50]. Most microorganism are so diminutive that in most cases they are impossible to see without specialised equipment, such as a microscope. The ability of microorganisms to detect and move towards certain stimuli is called taxis [51]. This stimuli can be light (phototaxis), magnetic fields (magnetotaxis), and chemical gradients (chemotaxis) [50]. To move towards the stimuli, a wide variety of microorganisms use filaments called cilia and flagella. Microorganisms with flagella have a motor that allows them to rotate the flagella in the form of a helix (figure 2.15). Moreover, other microorganisms with flagella can use it to create a sinusoidal wave. Such is the case of the sperm. On the other hand, the motion of cilia has two phases. Firstly, the filament moves in one direction while being completely straight. Then, the filament bends while moving in the opposite direction [52]. The three

previously mentioned methods create a nonreciprocal motion that allows them to propel themselves at low Re.

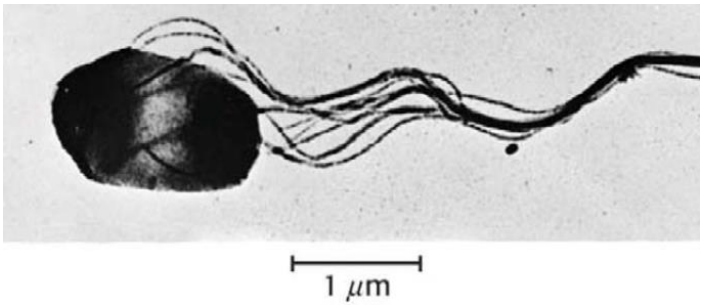

Figure 2.15 Photo of a microorganism with a helical flagella (from [52]).

2.3.2 Swimming micro-robots

Micro-robots inspired by microorganisms are currently being developed for targeted drug delivery inside the human body. The reason behind this is because when drugs are passive delivery to the desired organ, other organs get damaged because some particles of the drug accumulate on them [51]. A way to reduce this damage is by developing micro-robots that actively deliver the drugs to the desired organ [51]. These robots achieve propulsion by a combination of a locomotion method and an actuation method. The locomotion method is the one used to break the time-symmetry to swim at low Reynolds number, usually inspired by microorganisms. However, since these robots are too small to carry actuators like motors, an external actuation method is needed to generate motion. There are four actuation methods to travel through the body at a low Reynolds number, which are: magnetic actuation, microorganism-based actuation, acoustic actuation, and chemical reaction-based actuation [51]. In magnetic actuation (figure 2.16), the micro-robot contains a permanent magnet, and when it is placed in a magnetic field, this will provoke a movement on the robot [49]. Microorganism-based actuation involves using a swimming microorganism as an actuator to deliver the drugs that is controlled [51]. The ability of the microorganism to detect and move towards certain stimuli is called taxis, and by controlling such stimuli it is possible to control the motion of the organism [51]. In acoustic actuation, when

an acoustic wave is generated this one generates a pressure gradient that exerts a force on the micro-robot propelling it [51]. In chemical reaction-based actuation a catalyst metal in conjunction with its surroundings triggers a chemical reaction that propels the robot [51]. Nonetheless, an in-pipe "swimming" robot should be large enough to carry its own actuators. Thus, it may be better to focus on the locomotion methods.

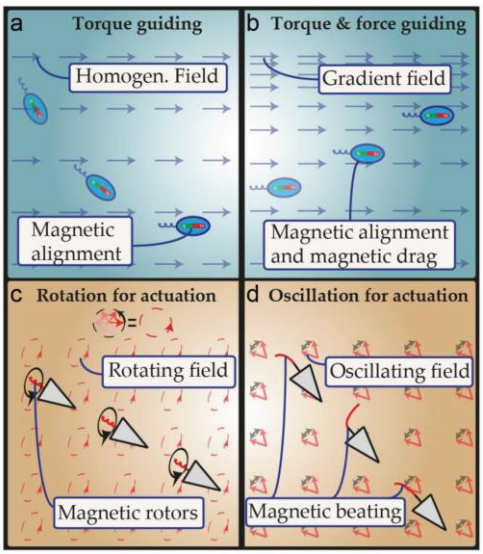

Figure 2.16 Effects on robots caused by the magnetic fields (from [49]).

An example of a swimming micro-robot inspired by sperms can be seen in [53]. To generate propulsion, a magnetic field exerts a torque on the head of the robotic sperm, generating a bending moment on the robot, which in turn creates travelling waves on the flexible tail. A similar approach can be seen in helical micro-robots. Just as in sperm-like robots, these robots consists of a head with a permanent magnet and a tail. The tail has a helical shape, and when the rotating magnetic field makes the head rotate, the tail rotates and achieves helical propulsion [54] [55] [56]. This tail can be rigid as in [54] [55]. In [55] the idea of adding a second helical tail was analysed (figure 2.17). The double tail is expected to increase the velocity and efficiency of the micro-robot.

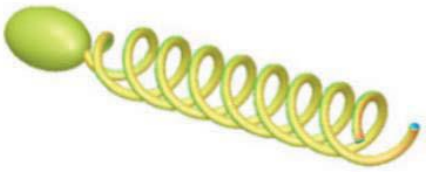

Figure 2.17 Helical micro-robot with two helixes (from [55]).

An example of a soft helical tail can be seen in [56]. When the robot is not in motion the tail stays straight, but when the robot starts to rotate the tail begins to twist and forms a helical shape. However, as the rotation frequency increases the pitch length near to the body starts to decrease (figure 2.18a), which decreases the velocity in this point. And since the velocity of the rest of the tail is greater, the pitch length of the rest of the tail decreases until a stable point is reached (figure 2.18b). If this trend continues the pitch length becomes zero, and the tail forms a cylindrical structure (figure 2.18c), where the robot cannot propel itself anymore. Nevertheless, if the trend continues even after stopping, the pitch length continues to decrease until it becomes negative. Then, the end of the tail forms a semi-helical structure at the opposite side of the micro-robot, propelling it in the opposite direction.

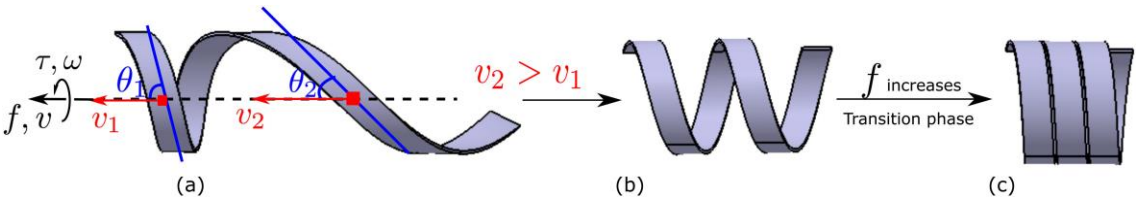

Figure 2.18 Contraction of the helical tail caused by the increase in frequency (from [56]).

There are micro-robots with undulatory locomotion, for example the robot in [57]. The micro-robot has a rigid body that consist of four sections interconnected by joints (figure 2.19). In the front section is the head which is a straight line shape with a U-shape at an extreme. The next two sections of the body have the same shape as the front one, but the extremes have joints to interconnect them. And at the end is a section that acts as the caudal fin, which is a straight line with a joint at one end. In the head of the front section

is located a magnet that, when an oscillating magnetic field is applied, makes the head oscillate. When the front section oscillates the “U” shape at the end collides with the head of the next section, transmitting the undulation, which keeps being transmitted until it reaches the caudal fin. The direction of the swimming is in the central line of the oscillation of the head. Thus, by controlling the magnets the robot performs an undulatory motion.

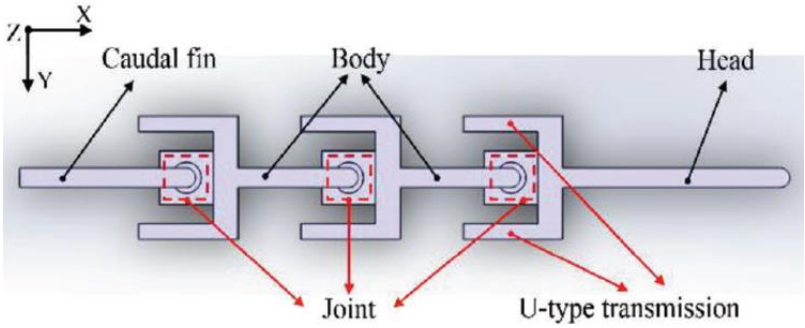

Figure 2.19 Different sections of the rigid body micro-robot (adapted from [57]).

The micro-robots that showed an undulatory locomotion could be compared with undulatory snake-like robots. As was previously pointed out, this type of robot typically requires a large number of actuators to generate the motion, the control of the entire system is more complex, and the power efficiency is lower [12]. The helix propeller method was the most utilized in literature for micro-robots. For our purposes, it has the advantage of being relatively easy to replicate in a larger scale by using DC motors to generate the rotation. Nevertheless, it is worth noticing that all these robots where tested in controlled environments where there was no flow. Hence, it is difficult to predict how their performance would be affected inside a pipeline transporting oil. Moreover, the hydrodynamics of a self-propelled macro-robot in a highly viscous fluid inside a pipe are relatively unknown. However, through CFD simulations and experiments may be possible to progress in our understanding of it. Therefore, the next step is to analyse the properties of the flow around a robot inside an oil pipeline. In Chapter 3 of this thesis, CFD simulations will be carried out and compared against previous investigations to find an appropriate methodology. Then, chapters 4 and 5 will utilise such methodology

to simulate several geometries for the robot's body inside pipelines of different diameters, fluids of various viscosities, and different proximities to the walls.

2.4 Computational fluid dynamics

Computational Fluid Dynamics (CFD) is a branch of Fluid Mechanics that analyse fluids in motion by solving the governing equations of fluid dynamics through numerical methods. This section will be a brief introduction to CFD. Such knowledge will be necessary to comprehend the work done in this project, since CFD was the method utilised to analyse the flow around the objects inside the pipelines. The information on this chapter is from the book "Computational Fluid Dynamics A Practical Approach" by Tu, J. [47].

2.4.1 What is Computational Fluid Dynamics (CFD)?

When trying to solve problems in the area of fluid dynamics there are three different methods that can be applied. The first method is analytical fluid dynamics, where the equations are manually solved. This is the simplest method, but at the same time, it only works for simple problems. Secondly, experimental fluid dynamics, where expected conditions are simulated in a controlled environment to observe the results. This method is accurate but expensive, because special installations need to be built and the necessary instrumentation needs to be bought. The third method is computational fluid dynamics (CFD), where the required equations to solve fluid dynamics problems are transformed into a computer program. Then, this program simulates and solves the problem.

CFD has several advantages when compared with the other two methods. For example, it allows to solve problems with a higher complexity than with the analytical method. Also, CFD can usually solve simple problems cheaper and faster than the experimental approach. However, the required time to solve a problem is conditioned by the hardware and the complexity of the problem. Therefore, as the complexity increases, it might be the case that the simulations require more time than the experiments. Moreover, there will

always be a discrepancy between the simulations and the actual fluid behaviour due to numerical errors. Nonetheless, CFD has the advantage of being able to simulate situations that would be impossible to replicate in a laboratory.

Procedure

CFD software follows a standard procedure to carry out simulations. It is composed of three stages: pre-process, solver, and post-process. At the same time, these three stages are composed of six steps: geometry creation, mesh creation, selection of physics and fluid properties, specification of boundary conditions, initialization and solution control, and monitoring convergence. It is important to notice that the basic idea behind each step is the same independently of the problem that is to be solved. However, the actual procedure to carry out each step depends on the problem. For example, the geometry that needs to be created to solve a problem of flow in a pipe is not the same than the one for a mixer.

The first stage is the pre-process, which has the objective of setting up the problem. The first step of this stage is the geometry creation. In this step all the necessary geometries for the problem are created. Examples of this are pipes, tanks, turbines, mixers or the wing of a plane. An example of a pipe with an object inside can be seen in figure 2.20a. The second step of pre-process is the mesh generation. The purpose of a mesh is to simplify the problems by dividing the geometry in small cells. Then, the properties of the flow in each cell are found individually. The higher the number of cell in a mesh, the higher the accuracy of the solution, and required time to obtain it. Thus, designing the perfect mesh is a trade-off between accuracy and time. In the figure 2.20b can be seen an example of a mesh. The third step of the pre-process is to select the physics and fluid properties. Here the properties of the fluid (viscosity, density, etc.) need to be specified. The final step of the pre-process is to specify the boundary conditions. These boundaries have the purpose of simulating the physical properties of the problem. Examples of this are: the inflow boundary used to specify from where the flow will enter the system; the

outflow boundary used to specify from where the flow will leave; the wall boundaries used to specify walls that the fluid cannot pass through.

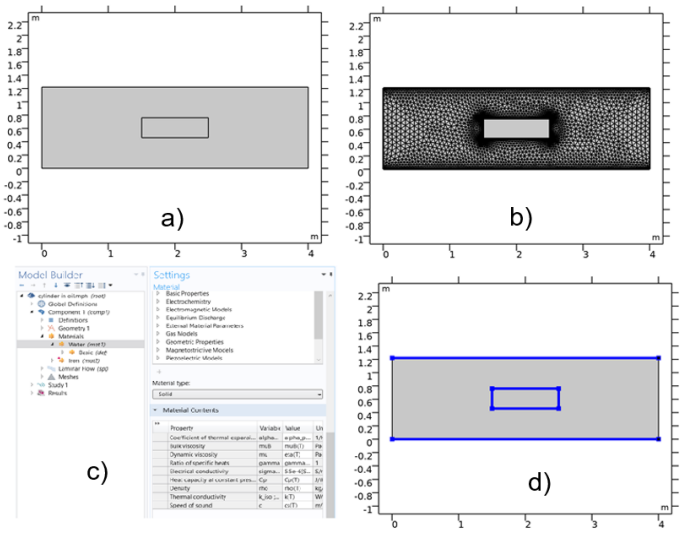

Figure 2.20 These images were taken in the software COMSOL Multiphysics. a) Example of a 2D geometry. b) Example of a mesh. c) Example of the setup of the fluid properties. d) Example of the setup of wall boundaries.

The solver stage has the purpose of finding the solution of the problem with specified conditions. This stage has two steps. The first step of the solver is the initialization and solution control. In this step the initial conditions of the simulations are set up. For example: initial velocity, pressure, and temperature. Then, the discretization or interpolation scheme is chosen. The scheme can be of first or second order, and the higher the order the more precise it is. This scheme is the method used by the numerical solution technique which is commonly the finite volume method. The second step of the solver is to monitor the convergence.

CFD uses an iterative method to solve the algebraic equations. While these equations are being solved, errors are being generated. As the process continues, these errors are reduced and, when these fall under certain tolerance, the solution has converged.

Finally, once the solution has been found, the results are presented in the form of various graphs. This is the post-process and these graphs are automatically generated by the software. An example can be seen in figure 2.21.

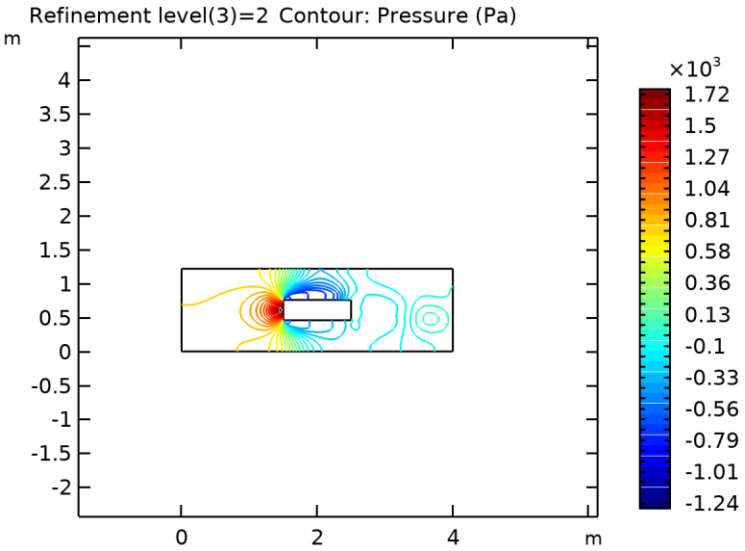

Figure 2.21. Example of a contour plot representing pressure done in the software COMSOL Multiphysics.

Chapter 3 Computational Fluid Dynamics Methods

The purpose of this project is to model a robot with an ellipsoidal body inside oil pipelines of different diameters and fluid viscosities. Thus, it is essential to create a model whose results can be corroborated against experimental and numerical data. Such results will give confidence that the initial scenario of this research is valid and can serve as a baseline for simulations in later stages of the project. Therefore, the objective of this chapter is to test the theory explained in Subchapter 2.4, in order to determine the mesh, boundary conditions, and solver settings that will be used during the studies in chapters 4 and 5.

This project is essentially the study of a bluff body inside a pipeline. Due to its simplicity and similarity to the object studied in this project, a sphere was selected as the body that could more accurately serve as an initial guess. This geometry can be elongated in subsequent studies to resemble the desired geometry of an ellipsoid. Additionally, it was decided to start with a validation case with a low Reynolds number of 400 because, in this range, the flow is laminar. This simplifies the turbulence model required for the simulations and can be further developed upon later.

Subchapter 3.1 will describe the first validation model, which will be a sphere inside a tank. This will serve to test the mesh and settings to resolve the flow and forces around the sphere and compare them against experimental data. Subsequently, Subchapter 3.2 will explain the second validation case, which aims to place the previously studied sphere inside a pipe with slip boundary condition on the pipe walls to test the boundary conditions and meshes in this scenario and prove their validity. Then, Subchapter 3.3 will explore the effects of activating the no-slip boundary condition on the pipe walls which and bring the validation case to a more realistic scenario. Finally, Subchapter 3.4 will

summarise the findings of this chapter and explain the methods that will be used in the following chapters.

3.1 Validation study 1: Sphere inside a rectangular tank

For the purpose of this project, it is important to create a model that can accurately simulate and capture the flow and forces around a bluff body. Ideally, this model should be grounded on experimental data to make sure that the physics match those of the real world. This validation study is based on the experimental studies that investigated the flow patterns around a sphere at low Reynolds numbers [58]. Therefore, this section aims to test boundary conditions, solver settings and meshes to observe how accurately these replicate experimental results.

The experimental work done in [58] aimed to provide and insight into the properties of sphere wakes in still surroundings at sphere Reynolds numbers (Re_s) from 30 to 4000. Figure 3.1 shows the experimental set up. It consists of a rectangular windowed tank of 0.415 m x 0.535 m x 910 m filled to a depth of 0.875 m with a water-glycerine mixture, a poly carb sphere with a diameter of 0.01 m mounted on a stainless-steel wire, and a laser Doppler velocimetry (LDV) fixed at a height of 0.45 m to measure axial velocity profiles. Additionally, a fluorescent dye was injected to trace the fluid motion.

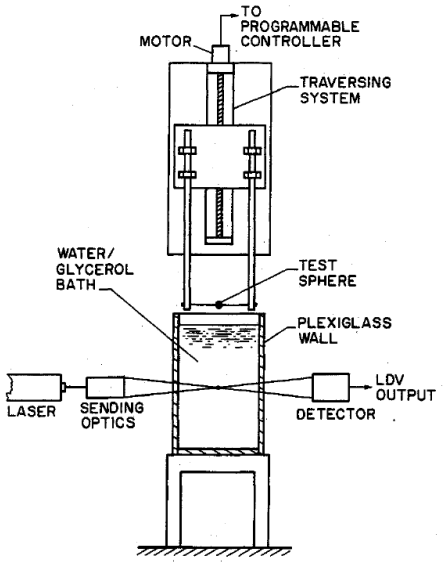

Figure 3.1Experimental set up used in [58].

Each experimental run commenced with the motorized towing system accelerating the sphere to the desired velocity prior to entering the bath at a sufficient distance from the tank walls to minimize the effects of boundary interactions on the wake. This velocity ranged from 0.147 m/s to 0.408 m/s depending of the desired Re and was maintained constant while the sphere transverse the bath. The kinematic viscosity of the water-glycerol mixture ranged from 1.02×10^{-6} m^2/s to 4.2×10^{-5} m^2/s. These two parameters, the towing velocity and kinematic viscosity, were varied to ensure the coverage of the desired range of Reynolds numbers. A list of the tested Reynolds numbers, velocities and kinematic viscosities can be seen in table 3.1.

The following simulations replicate the set up for the Re_s of 400 to compare the drag coefficient (C_d) and streamwise velocity against the results obtained in experimental studies [58]. The C_d was compared against the results for Re_s = 400, but the streamwise velocity was compared against the results for Re_s = 280. This case was utilised a numerical study [59] for their numerical validation case. By comparing the results of the present study against the case for Re_s = 280, it was possible to compare the results of the second validation case against both experimental and numerical data.

Re	Kinematic viscosity (m^2/s)	Velocity (m/s)
35	4.2×10^{-5}	0.147
60	4.2×10^{-5}	0.252
90	3.78×10^{-5} – 4.1×10^{-5}	0.34 – 0.369
170	2.4×10^{-5} – 2.8×10^{-5}	0.408 – 0.476
280	1.01×10^{-5} – 1.17×10^{-5}	0.283 – 0.328
400	1.02×10^{-5}	0.408
960	4.8×10^{-6}	0.461
4000	1.02×10^{-6}	0.408

Table 3.1 Experimental parameters [58].

3.1.1 Geometry

Figure 3.2 shows a CAD replica of the experimental set up used in [58]. The 3D model was created using the Ansys design modeller and it consisted of a rectangle of 0.415 m x 0.535 m x 0.875 m, 0.875 m being the height at which the tank utilised in the experiments was filled up to, and a sphere of diameter 0.01 m placed at a height of 0.45 m in the centre of the tank.

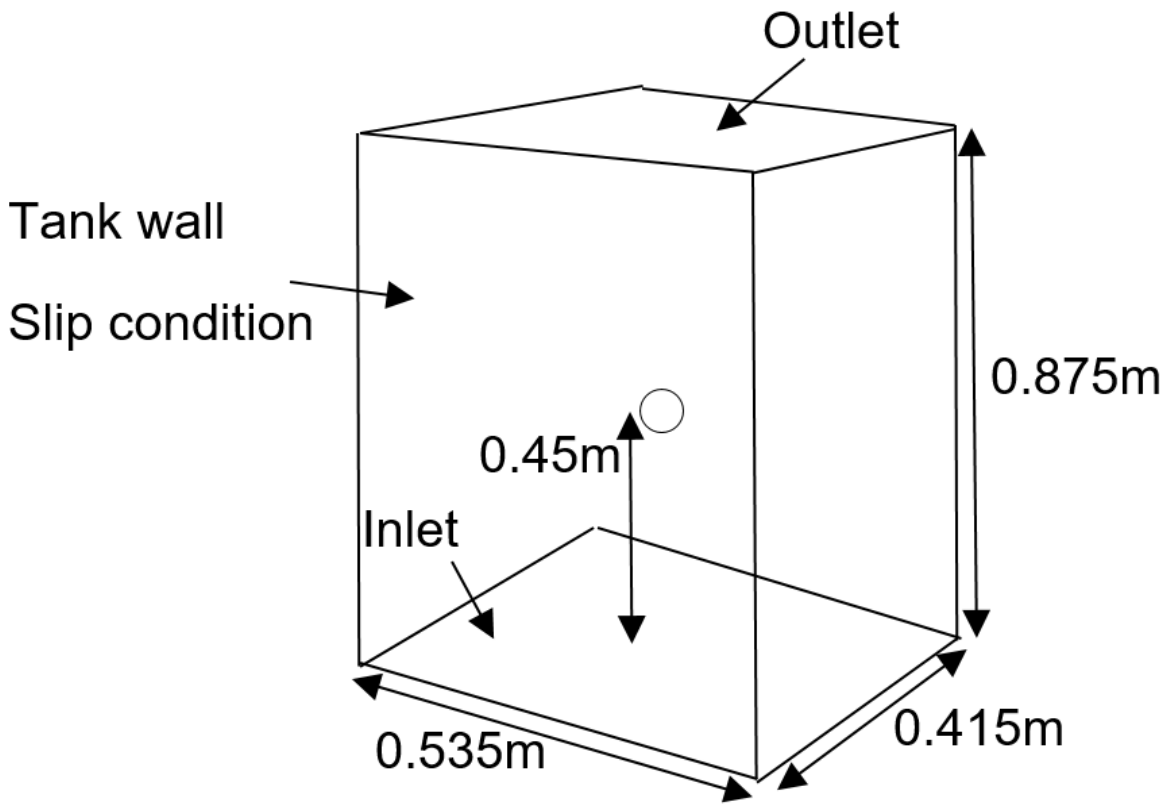

Figure 3.2 Geometry and boundary conditions.

3.1.2 Mesh design

The meshes for this study were created using Ansys Fluent meshing. Although, this software cannot create completely structured meshes, it has the advantage of offering a considerable grade of automation in the process of creating and refining a mesh. As a result, the software can create multiple meshes with acceptable quality in a relatively short amount of time, which was necessary for the studies conducted in future chapters.

As can be seen in figures 3.3 and 3.4, the mesh was a hexcore mesh consisting of unstructured surface meshes on the faces, that transition into an inflation layer in the case of the sphere, and two unstructured layers of tetrahedral elements in the case of the tank faces. Both transition into a structured hexahedral mesh in the rest of the geometry. Furthermore, a refinement region was created to achieve a higher resolution on the wake to capture the boundary layers, separation, and recirculation. Additionally, in order to test the extent to which the grid affects the results, three meshes (T1, T2, and T3) of varying resolutions were created to conduct a mesh sensitivity study. A detailed account of the different mesh parameters can be seen on table 3.2.

Mesh	Tank element size (m)	Sphere element size (m)	First cell height (m)	Growth ratio	Layers	Cell count
T1	0.00845	0.000169	0.0003	1.0338	7	883,470
T2	0.0065	0.00013	0.0003	1.026	7	1,535,183
T3	0.005	0.0001	0.0003	1.02	8	2,581,299

Table 3.2. Mesh parameters.

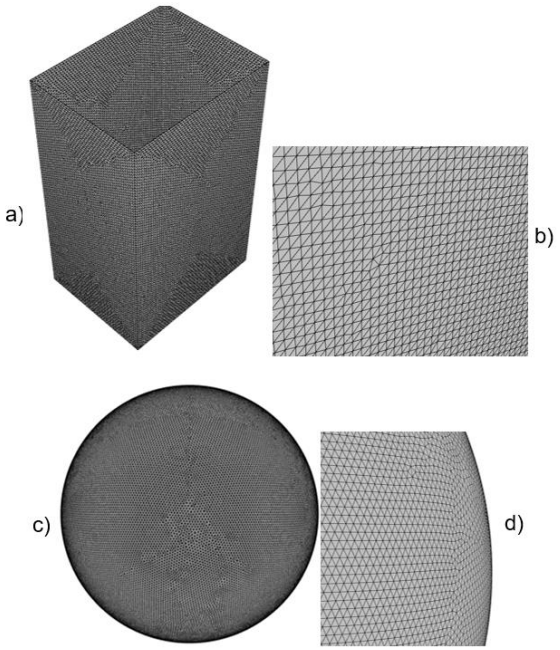

Figure 3.3 Surface mesh. a) Tank surface mesh; b) close up of tank surface mesh; a) sphere surface mesh; b) close up of sphere surface mesh.

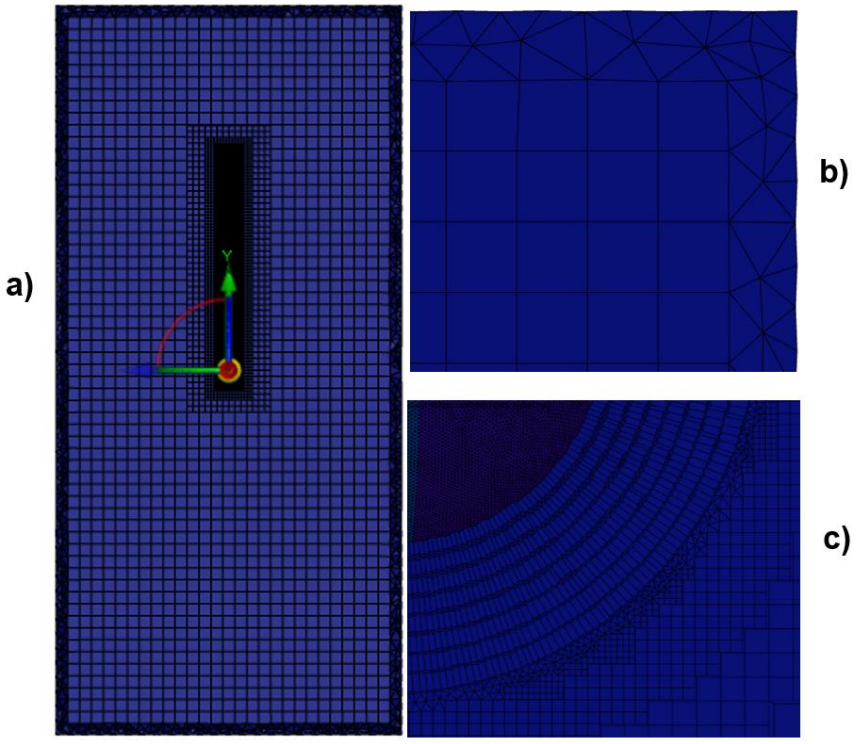

Figure 3.4 a) volume mesh; b) unstructured layers on tank walls; and c) sphere inflation layer.

3.1.3 Boundary conditions and settings

In order to simplify the simulation, certain considerations were made. Firstly, since the sphere is considerably smaller than the tank, it can be assumed that this last one's walls have no effect on the flow around the aforementioned. Secondly, if the relative velocity is maintained, it is of no importance whether it is the sphere or the fluid what moves. As a result, it is possible to replicate the conditions of the flow surrounding the sphere by making the fluid move while maintaining the sphere fixed in its position.

To achieve a Re_s of 400, an inlet with a uniform velocity of 0.408 m/s was chosen for the bottom face. This is the same value used in the experiments in [58], with the difference that, in the experiments, the sphere was the one moving at 0.408 m/s. A fluid density and viscosity of 1156.6 kg/m^3 and 0.011797 Pa·s were used to replicate the kinematic viscosity of $1.02x10^{-5}$ m^2/s utilised in the same studies [58]. Additionally, an outlet with a gauge pressure of 0 Pa was used for the top face, slip boundary conditions were used on the side faces, and a no-slip boundary condition was used on the sphere. A list of the boundary conditions and solver settings can be seen in table 3.3.

The simulation of flow past a sphere at a Re_s = 400 requires the utilisation of a transient solver to simulate the complex flow patterns. However, in an attempt to reduce the computational cost of the CFD studies conducted in the next chapters of this work, the steady-state solver was tested. The laminar viscous model was utilised, and the velocity-pressure coupling, pressure, and momentum discretization schemes were SIMPLE, second order, and second order upwind respectively. Although, second order discretization schemes are less stable, their higher accuracy makes them a more suitable option.

Additionally, even though, in the case of the gradient discretization scheme the Green-Gauss cell-based is better for structured meshes, and the node-based is better for unstructured ones, the later one was selected for this validation case. The reason for this is because it is expected that, in future chapters, the complexity of the models and the number of cells will considerably increase. A possible counter measure is to slice the geometry in two on the XY plane and utilise a symmetry boundary condition on the resulting

face, effectively cutting the number of cells in approximately half. However, in this scenario, the main zone of interest, which is the centre of the pipe, ends on the unstructured mesh layers of this symmetry plane. Thus, it is expected that the Green-Gauss node-based method will produce more accurate results.

Boundary condition / properties	**Details**
Solver	Steady-state
Viscous model	Laminar
Inlet	Inlet velocity of 0.408 m/s
Outlet	0 Pa
Walls (tank)	Slip boundary condition
Walls (sphere)	No-slip boundary condition
Density	1156.6 kg/m^3
Viscosity	0.011797 Pa·s
Pressure-Velocity coupling	SIMPLE
Discretization	Green-Gauss node based, second order for pressure, and second order upwind for momentum.

Table 3.3. Simulation settings.

3.1.4 Analysis

This section presents a detailed comparison between the results obtained from the computational fluid dynamics simulations conducted in the present study and the experimental data provided in previous experimental studies [58]. The primary focus is on examining key parameters of streamwise velocity and drag coefficients.

Flow pattern

Figures 3.5 and 3.6, show a comparison of the flow pattern and recirculation region obtained from the three meshes of the sensitivity study. Unfortunately, it is impossible to visually compare the flow pattern against the experimental results because no image of the Re_s of 400 was provided. Moreover, due to the utilisation of a steady-state solver, the vortex shedding expected for Re_s > 280 cannot be observed. But it can be seen that the wake presents the asymmetric pattern expected from theory for Re_s > 200 [58]. Additionally, figure 3.6 shows the recirculation region caused by the flow around filling in after passing by the sphere. This region seems to be sensitive to the mesh resolution since meshes T1 and T2 show a shorter recirculation region.

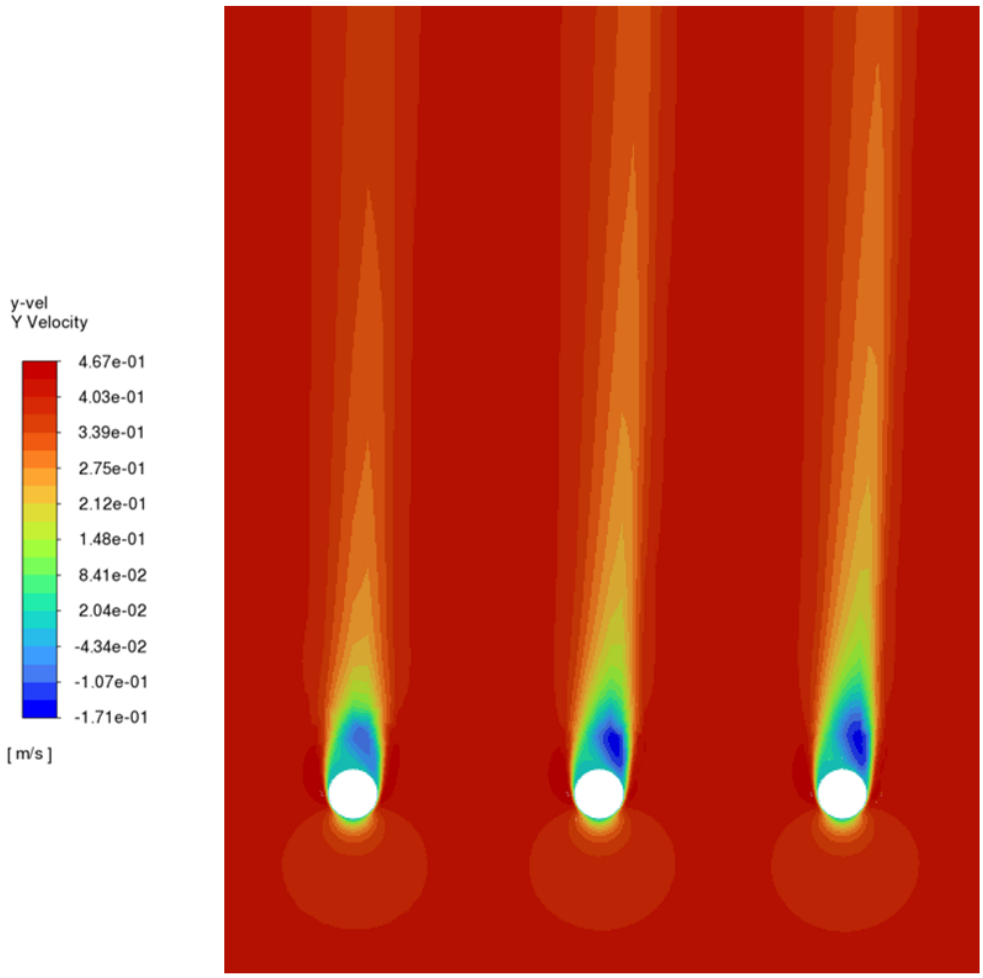

Figure 3.5 Flow velocity in y-axis of the mesh sensitivity study. From left to right: T1, T2, T3.

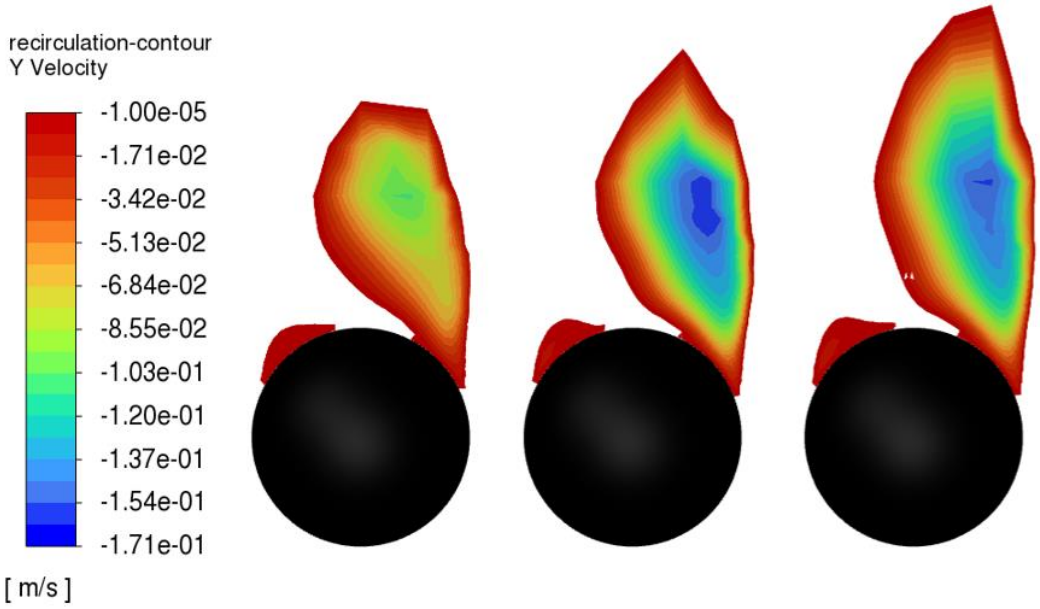

Figure 3.6 Recirculation region of the mesh sensitivity study. From left to right: T1, T2, T3.

Streamwise velocity

The streamwise velocity (u/U_∞) refers to the centreline flow velocity taken from the rear stagnation point (x/d = 0.5) of the sphere up to a distance of 25d (d being the diameter of the sphere) divided by the free stream velocity of 0.408 m/s. The region from where the streamwise velocity was taken can be seen on figure 3.7. The data from the experimental studies was obtained through the tool plot digitizer which allows to upload the image of a plot, and extract the values of the points in such plot. A comparison of the results is shown in figure 3.8. The present study shows that the valley that appears immediately after the sphere, which represents the recirculation region, is less pronounced and recovers faster when compared with the experimental data. Which means that model utilised is predicting a shorter recirculation region. Despite this, the data from the present study shows a great agreement with the experimental data despite this last one being for a Re_s of 280 with a higher kinematic viscosity and sphere velocity.

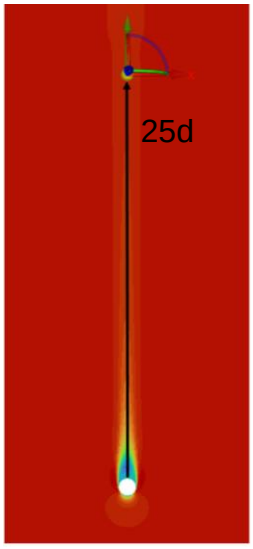

Figure 3.7 The black line indicates from where the streamwise velocity was taken.

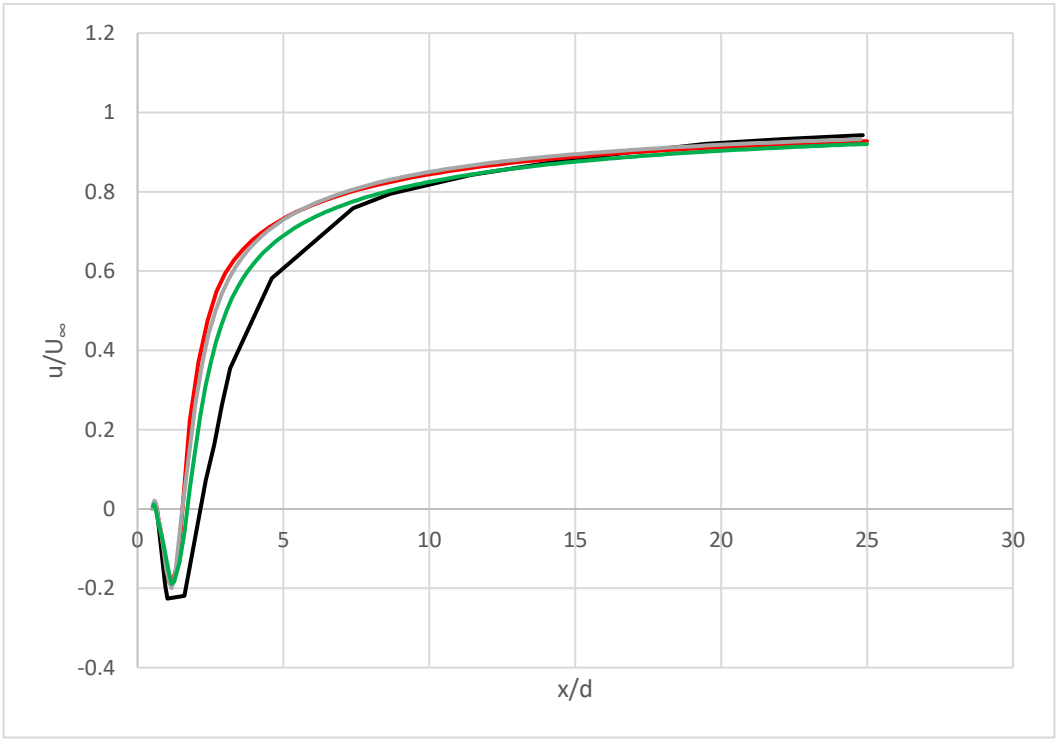

Figure 3.8 Streamwise velocity comparison [black line: experimental data from [58] for Re_s = 280; red line: present study with mesh T1 for Re_s = 400; grey line: present study with mesh T2 for Re_s = 400; green line: present study with mesh T3 for Re_s = 400].

Drag coefficient

The final parameter to be compared is the drag coefficient (C_d) which, in the present study, was calculated with the equation 8 [60].

$$C_d = \frac{F_D}{0.5\rho A U^2} \quad (8)$$

Where F_D is the drag force obtained through the CFD simulations, ρ is the fluid density, and A is the cross-section area of the sphere, and U is the free stream velocity.

On the other hand, in [58] the drag forces were not measured, and C_d was calculated with the Re utilising equation 9.

$$C_D = \frac{24(1+\frac{Re^{2/3}}{6})}{Re} \quad (9)$$

The values of the C_d obtained through simulations in the present study are shown in table 3.4. The three values C_d obtained in the mesh sensitivity study show an acceptable proximity to the values calculated in [58]. This serves to prove the validity of the methods and meshes.

Case	Cell count	C_d
Re_s = 400 (exp.) [58]	None	0.603
T1	883,470	0.666
T2	1,535,183	0.661
T3	2,581,299	0.643

Table 3.4 Drag coefficient.

3.1.5 Conclusion

Despite the overall good correlation with the streamwise velocity, the drag coefficient obtained from the simulations is slightly higher than the experimental value. This discrepancy may arise from several factors: (1) the steady-state solver cannot fully capture the flow properties; (2) the grid

resolution near the sphere's surface, since, although the three meshes utilised in the mesh sensitivity study reported similar values for C_d, the finest mesh, T3, reported a smaller C_d than T1 and T2; (3) subtle differences in the boundary conditions between the simulations and experiments such as the small disturbances caused by the wire where the sphere is mounted; (4) differences in the methodology to calculate the C_d. In [58] the C_d was calculated with Re utilising equation 9, while in the present study the C_d was calculated by measuring the drag force through CFD simulations and using equation 8.

Despite the mentioned minor discrepancies, the present study successfully utilised CFD simulations to replicate the experimental work done in [58]. Through the usage of such simulations, the flow characteristics around a sphere moving through a water-glycerol mixture inside a rectangular windowed tank at a Reynolds number of 400 were modelled. The simulations proved to have an acceptable degree of accuracy capturing the wake structure, streamwise velocity profiles, and drag coefficient to compare it against experimental data. Therefore, demonstrating the robustness of the CFD model employed.

3.2 Validation study 2: pipe with slip condition

This validation case aims to replicate the numerical work done in [59] which aimed to provide and insight into the properties of the flow around a sphere in a pipe at low Re and different blockage ratios (BR) [59]. Their study conducted three types of simulations based on three Reynolds numbers. Fixed pipe Reynolds number (Re_p) and varying sphere Reynolds number (Re_s); fixed Re_s and varying Re_p; and a fixed Reynolds number of the gap (Re_g) between the sphere and the pipe wall, and a varying Re_p. However, for this study is of particular interest the validation study where they compared the results of their numerical simulations against the experimental studies mentioned in the previous subchapter, since it presented a close agreement between their numerical predictions and experimental data [58].

The validation study done in [59] consists of a stationary sphere within a pipe with a uniform velocity inlet. A diagram of their model can be seen in figure 3.9 where: D is the pipe diameter; Lu is the distance from the inlet to the centre of the sphere; and Ld is the distance from the centre of the sphere to the outlet. Additionally, d is the sphere diameter; r is the sphere radius; and R is the pipe radius. Moreover, a slip condition was used on the pipe walls. Thus, there is no interference from the pipe boundary layer with the flow around the sphere. And three parameters were utilised to compare their study against [58]: streamwise velocity, pressure distribution, and drag coefficient.

The simulations in this validation case replicated the validation study done in [59] for a Re_s of 400. Three meshes of several resolutions were used in order to conduct a mesh independence study. The streamwise velocity, pressure distribution, and drag coefficient were extracted and compared against the aforementioned numerical and experimental studies [58, 59]. This has the objective to assess the accuracy of the computational fluid dynamics (CFD) simulations. As a result, demonstrating that, if a slip condition is used on the pipe walls and these are at a distance where they do not interfere with the flow around the sphere, the geometry has no effect on the results. Thus, serving as a connection between the experimental work used in the previous validation study and the third validation study discussed in the next subchapter.

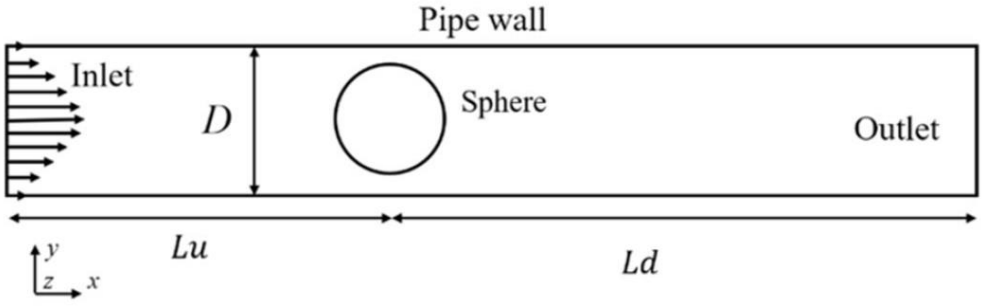

Figure 3.9 Diagram of the model used in the validation study done by [59].

3.2.1 Geometry

Figure 3.10 shows the diagram of the CAD model utilised in this validation study. The 3D model was created using the Ansys design modeller and it consists of a flow domain in the shape of a cylindrical pipe with a sphere placed along the axis of the pipe. The pipe has a D = 14d; the distance from the inlet to the centre of the sphere is Lu = 5D; and the distance from the centre of the sphere to the outlet is Ld = 7.5D. Additionally, the blockage ratio is BR ≈ 0.071. Those dimensions were utilised in [59], as according to the work done in [61], if the flow regime is laminar and a parabolic equation is used at the inlet, those distances are enough for the forces on the sphere surface to converge. Table 3.5 contains a list of the dimensions utilised for the validation case.

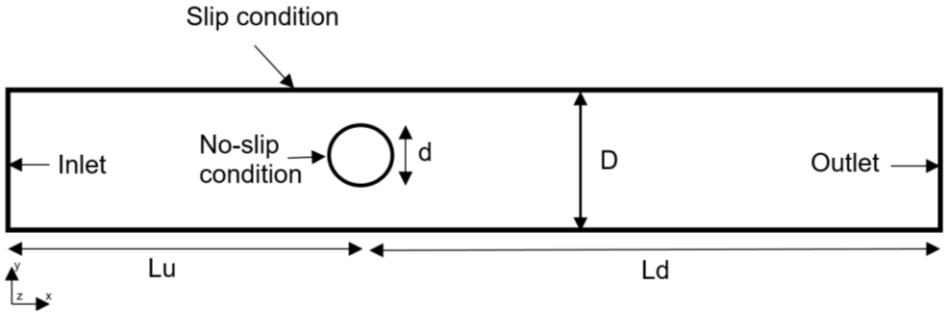

Figure 3.10 Diagram of the CAD model and boundary conditions.

Dimension	Length (m)
D	0.14
d	0.01
Lu	0.7
Ld	1.05
BR	0.071

Table 3.5 List of dimensions.

3.2.2 Mesh design

Similarly to the previous validation case, the software Ansys Fluent meshing was utilised to create three meshes (P1, P2, and P3) to conduct a mesh sensitivity study to ensure that the results were independent of the mesh size. Table 3.6 shows a list of the mesh parameters. Similarities with the mesh in the previous validation study are: the utilisation of an unstructured mesh with hexahedral elements; the element sizes of the three sphere surface meshes; an inflation layer applied on the sphere; since a slip condition was applied to the pipe wall, no inflation layers were utilised on those faces; a refinement region with a finer resolution was applied on the centre line of the pipe to capture the complex flow features around the sphere and in the wake region.

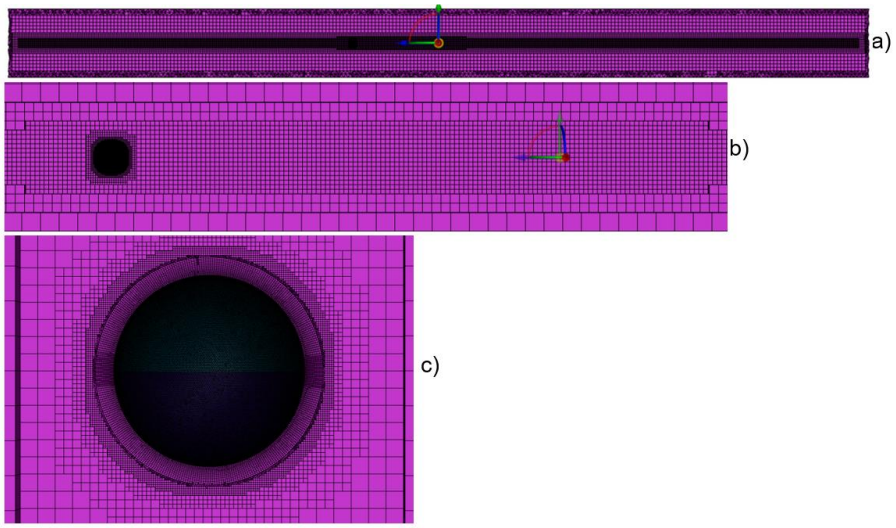

Figure 3.11 Volume mesh.

Mesh	Pipe element size (m)	Sphere element size (m)	Sphere first cell height (m)	Sphere growth ratio	Sphere layers	Cell count
P1	0. 014872	0.000169	4.225×10^{-5}	1.0845	13	904,790
P2	0.01144	0.00013	4.225×10^{-5}	1.065	14	1,438,404
P3	0.0088	0.0001	4.225×10^{-5}	1.05	15	2,223,853

Table 3.6 Mesh properties.

3.2.3 Boundary conditions and settings

The parameters and boundary conditions in the validation case were carefully defined to obtain a Re_s of 400. At the inlet of the pipe, a uniform velocity profile of 2 m/s was imposed. A pressure-outlet boundary condition was set to a gauge pressure of 0 Pa. The fluid density and viscosity were 2000 kg/m^3 and 0.1 Pa·s respectively. No-slip boundary conditions was applied on the surface of the sphere and a slip boundary condition on the pipe walls, to avoid the formation of a boundary layer that could interfere with and distort the flow around the sphere. Finally, this simulations utilised the same solver setting used in the previous validation case. A list of the boundary conditions and settings can be seen in table 3.7.

Boundary conditions / properties	**Details**
Solver	Steady-state
Viscous model	Laminar
Inlet (velocity)	2 m/s
Outlet	0 Pa
Walls (pipe)	Slip boundary condition
Walls (sphere)	No-slip boundary condition
Density	2000 kg/m^3
Viscosity (Pa·s)	0.1
Pressure-Velocity coupling	SIMPLE
Discretization	Green-Gauss node based, second order for pressure, and second order upwind for momentum.

Table 3.7 Simulation settings.

3.2.4 Analysis

This section presents a detailed comparison between the results obtained from the computational fluid dynamics simulations conducted for this validation study and the data obtained from numerical and experimental studies [58, 59]. The primary focus is on examining the flow patterns, streamwise velocity, pressure distribution, and drag coefficient.

Flow pattern

Figures 3.12 and 3.13, show a comparison of the flow pattern and recirculation region obtained from the three meshes of the sensitivity study. Similarly to the previous validation study, the wake is asymmetric as expected for $Re_s > 200$, and the length of the recirculation region is sensitive to the mesh resolution. However, in this case the side of the wake is different for each mesh of the sensitivity study. P1 has a centred wake with a mild inclination down and a less intense recirculation region; P2 has a wake on the upper side of the sphere; and P3 has a wake on the bottom side of the sphere. The differences seen in P1 may be because, being the coarsest mesh, it is incapable of properly detecting the flow intricacies. As for the difference in the recirculation region location for P2 and P3, it may be caused by the recirculation region instabilities for $Re_s > 280$ reported in literature [58].

Figure 3.12 Flow velocity in x-axis of the mesh sensitivity study. From top to bottom: P1, P2, P3.

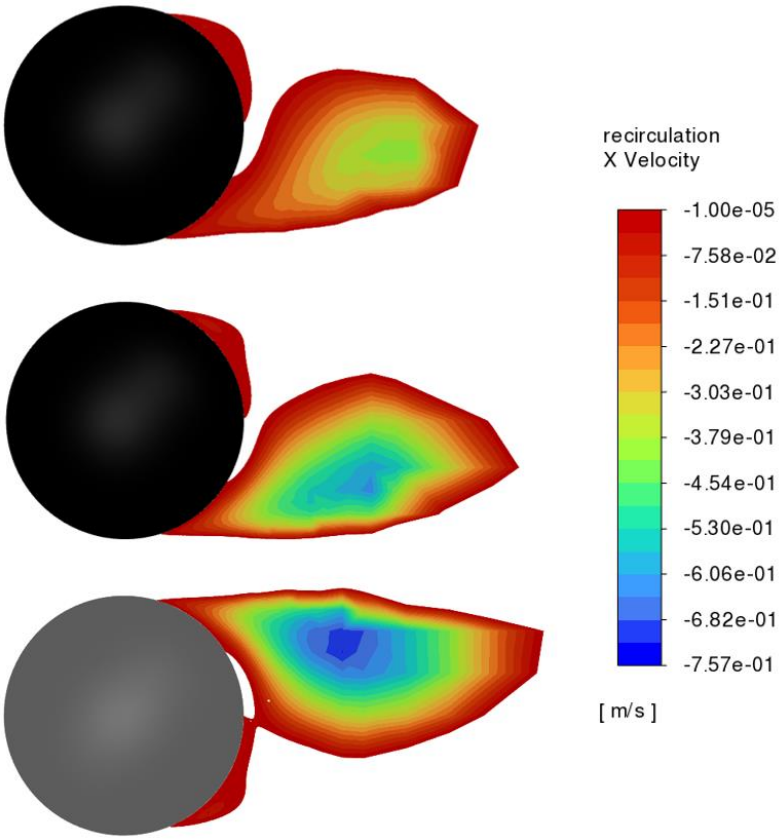

Figure 3.13 Recirculation region of the mesh sensitivity study. From top to bottom: P1, P2, P3.

Streamwise velocity

The streamwise velocity ($u/U\infty$) was taken from the rear stagnation point (x/d = 0.5) of the sphere up to a distance of 25d. Figure 3.14 shows a comparison of the numerical data obtained in this study, the numerical data presented in [59] for Re_s = 300, and the experimental data from [58] for Re_s = 280 (both obtained through plot digitizer). The data from the present study shows an identical behaviour than the data from the previous study validation. Which means that, for a BR ≈ 0.071 and a slip boundary condition, the geometry did not have an effect on the streamwise velocity.

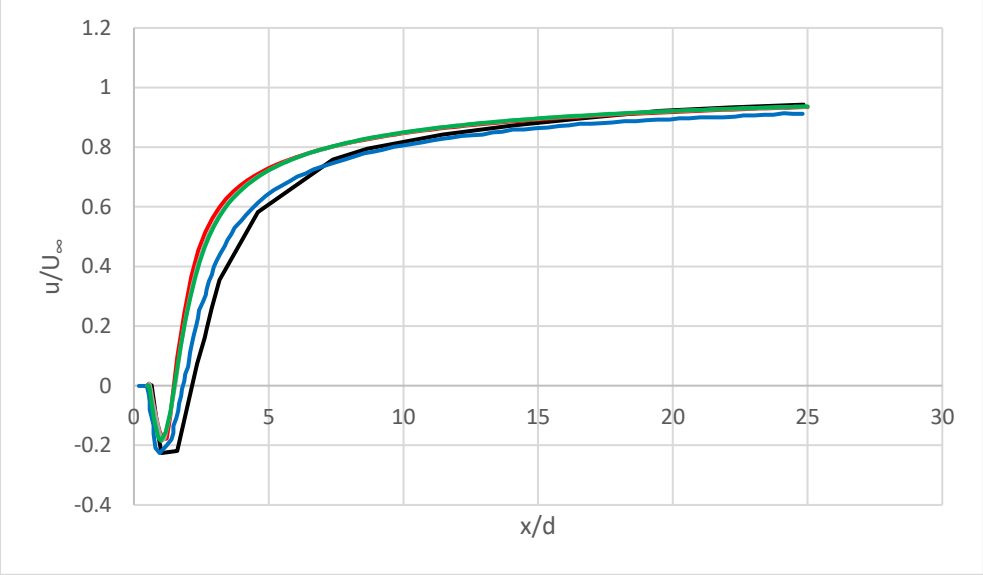

Figure 3.14 Streamwise velocity comparison [black line: experimental data from [58] for Res = 280; blue line: numerical data from [59] for Re_s = 300; red line: present study with mesh P1 for Res = 400; grey line: present study with mesh P2 for Res = 400; green line: present study with mesh P3 for Res = 400].

Pressure distribution

As was previously mentioned, the flow past a sphere with a Re_s > 280 presents and asymmetrical wake which becomes more pronounced when the Re_s increases. Figure 3.15 shows the pressure coefficient on the surface of the sphere. By comparing against the flow pattern in figure 3.13, it can be seen that the area with the highest pressure on the rear side matches the location

of the recirculation region. Thus, the pressure distribution varies depending on the side where is calculated. Figure 3.16 shows a comparison of the pressure distribution taken from the top and bottom, and the data from [59].

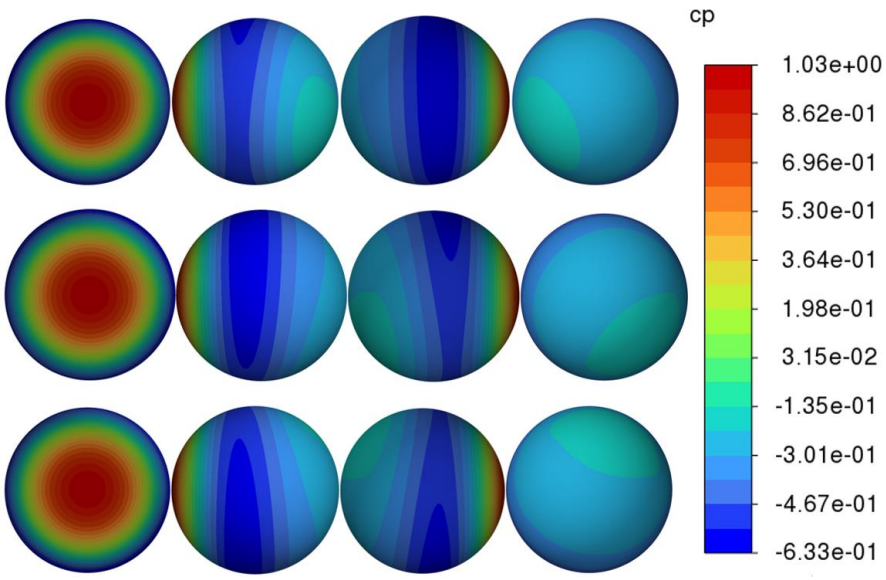

Figure 3.15 Pressure coefficient on the sphere surface. From top to bottom: P1, P2, P3. From left to right: front view, right view, left view, rear view.

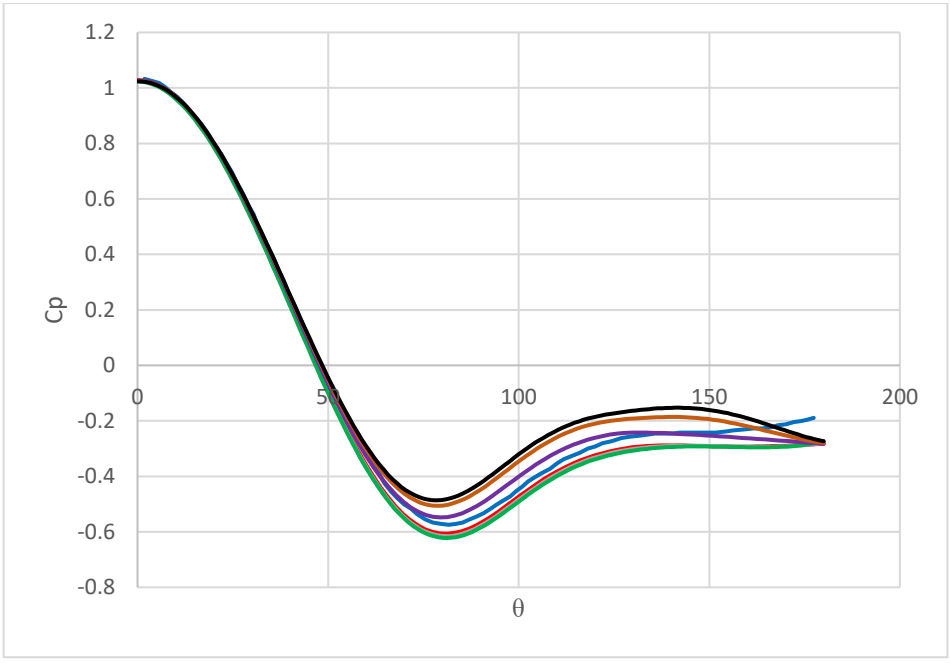

Figure 3.16 Pressure distribution [blue line: data from [59]; red line: P1; grey line: P2; green line: P3; purple line: P1 taken from the side of the recirculation region; orange line: P2 taken from the side of the recirculation region; purple line: P3 taken from the side of the recirculation region].

Drag coefficient

The values of the C_d obtained through simulations in the present study are shown in table 3.8. The three values of C_d for P1, P2, and P3 show a greater correlation with data provided in [58] and [59] for a Re_s of 400. However, these differences are not significant. They may be caused by differences in the mesh, since the mesh of this study 2 has a refinement region with a higher resolution along the centreline of the pipe.

Case	Cell count	C_d
Re_s = 400 (exp.) [58]	None	0.603
Re_s = 400 (num.) [59]	Unknown	0.599
T1	883,470	0.666
T2	1,535,183	0.661
T3	2,581,299	0.643
P1	904,790	0.639
P2	1,438,404	0.631
P3	2,223,853	0.630

Table 3.8 Drag coefficient.

3.2.5 Conclusion

The CFD simulations presented in this study successfully replicated the flow characteristics around a sphere in a pipe flow at a Reynolds number of 400, with a focus on the streamwise velocity, pressure distribution, and drag coefficient. The findings show an acceptable correlation with the numerical and experimental data reported in [58, 59]. However, the drag coefficient predicted by the simulations was found to be slightly higher than that reported in the original validation cases at Re_s = 400. This discrepancy, although minor, suggests that the drag force prediction is sensitive to numerical parameters such as mesh resolution, and boundary conditions.

3.3 Validation study 3: Pipe with no-slip condition

This study aims to observe effect that the boundary layer on the pipe wall has on the flow around the sphere. The activation of the no-slip boundary condition on the pipe wall means that there are two Reynolds numbers. The sphere Re (Re_s) and the pipe Re (Re_p). In this case, Re_p is 5600 and Re_s is 400. This creates the unknown of whether the viscous model should be selected based on Re_p or Re_s. As a result, this study aimed to test three viscous models: K-ω SST, Transition SST, and laminar. Therefore, defining the viscous model that should be used in the simulations of the studies in chapters 4 and 5 of this thesis.

3.3.1 Geometry, mesh design, boundary conditions, and settings

This study utilises the same parameters for geometry, mesh, boundary condition and solver settings than validation study 2. There are three differences: (1) the application of the no-slip boundary condition on the pipe wall; the inclusion of an inflation layer on the pipe wall; (3) the utilisation of the k-ω SST model for the mesh sensitivity study.

As mentioned, the application of a no-slip condition on the pipe wall meant that the Reynolds number of the pipe (Re_p) had to be taken into account. Since the Re_p is of 5600, if the viscous model for the initial mesh sensitivity study was selected based on Re_p a turbulence model had to be utilised. The three meshes for this sensitivity study (P4, P5, and P6) were created with the same parameters than the meshes in the previous validation study (P1, P2, and P3). After conducting the mesh sensitivity study, the viscous models Transition SST and laminar were tested utilising the mesh P5. Figure 3.17 shows the mesh, table 3.9 shows the parameters of the three meshes in the sensitivity study, and table 3.10 shows the boundary conditions and solver settings.

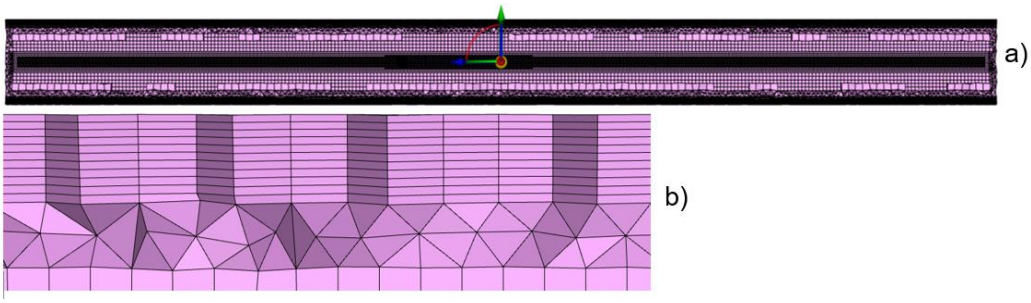

Figure 3.17 a) Volume mesh for the third validation study. b) Close up of the inflation layer on the pipe wall.

Properties	P4	P5	P6
Pipe: max. element size (m)	0. 01487	0.01144	0.0088
Pipe: first cell height (m)	0.001105	0.001105	0.001105
Pipe: growth ratio	1.0338	1.026	1.02
Pipe: infl. layers	30	39	50
Sphere. max. element size (m)	0.000169	0.00013	0.0001
Sphere: first cell height (m)	4.225×10^{-5}	4.225×10^{-5}	4.225×10^{-5}
Sph. growth ratio	1.0845	1.065	1.05
Sph. Infl. layers	7	7	8
Cell count	1,003,271	1,579,916	2,627,032

Table 3.9 Mesh properties.

Boundary condition / properties	Details
Solver	Steady-state
Viscous model	K-ω SST, Transition SST, and Laminar
Inlet	2 m/s
Outlet	0 Pa
Walls (pipe)	No-slip boundary condition
Walls (sphere)	No-slip boundary condition
Density	2000 kg/m^3
Viscosity	0.1 Pa·s
Pressure-Velocity coupling	SIMPLE
Discretization	Green-Gauss node based, second order for pressure, and second order upwind for momentum.

Table 3.10 Simulation settings.

3.3.2 Analysis

This section presents a detailed comparison between the results obtained from the computational fluid dynamics simulations conducted for this validation study and the numerical and experimental data provided in [58, 59]. The primary focus is on examining the effect the boundary layer has on the flow around the sphere. In addition, the viscous model that should be used, flow patterns, streamwise velocity, pressure distribution, and drag coefficient.

Flow pattern

Figures 3.18 and 3.19 show a comparison of the flow pattern and recirculation region obtained from the mesh and viscous model sensitivity study. The three simulations of the mesh sensitivity study show a similar pattern among them. With the finest mesh, P6, showing a slightly larger recirculation region. When compared with the previous study without the pipe wall boundary condition, the simulations with k-ω SST show a more symmetric wake. With exception for the laminar model, which shows a minor downward inclination. Finally, when compared with the k-ω SST, the Transition SST seems to predict a more negative velocity for the x-component of the recirculation region.

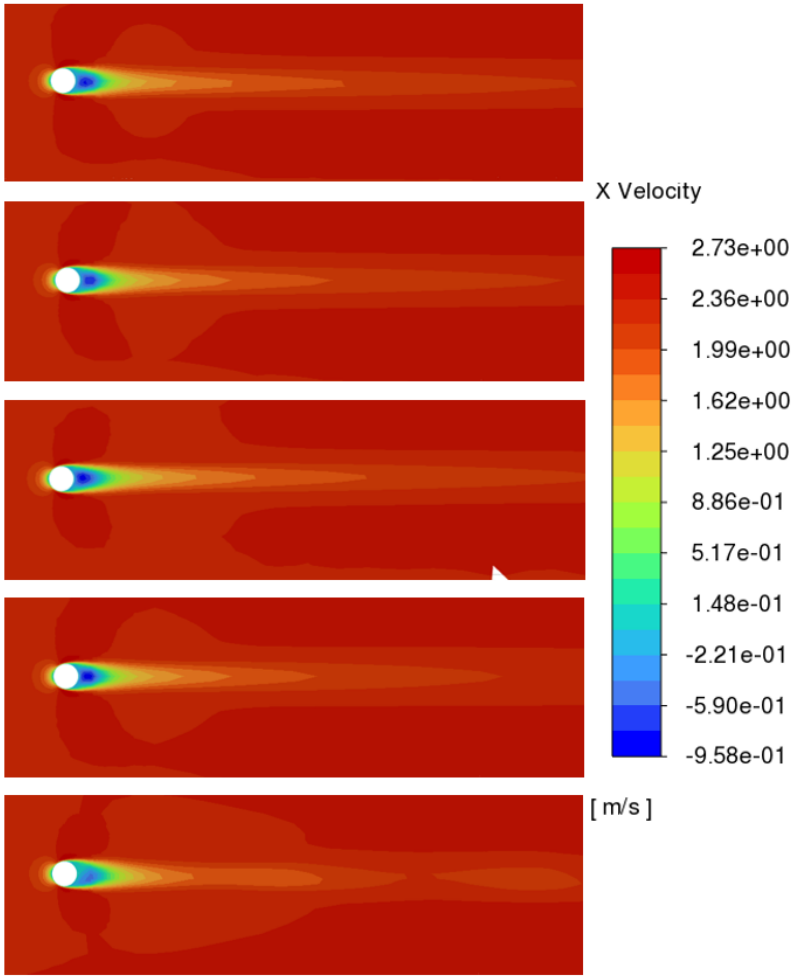

Figure 3.18 Flow velocity in x-axis. From top to bottom: P4 k-ω SST, P5 k-ω SST, P6 k-ω SST, P5 Transition SST, P5 laminar.

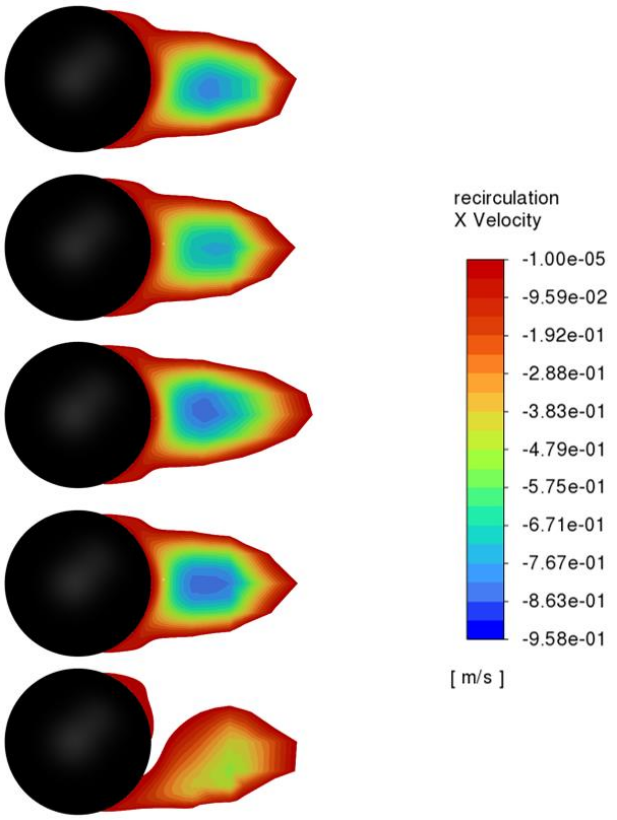

Figure 3.19 Recirculation region of the mesh sensitivity study. From top to bottom: P4 k-ω SST, P5 k-ω SST, P6 k-ω SST, P5 Transition SST, P5 laminar.

Streamwise velocity

In previous studies, the streamwise velocity was the mean velocity. However, because of the activation of the no-slip boundary condition, the velocity profile inside the pipe has a flatted parabolic shape. Since the sphere is relatively small compared to the pipe. The velocity utilised for the free stream velocity was the maximum velocity at an upstream reference point.

Identically to previous studies, the streamwise velocity (u/U_∞) was taken from the rear stagnation point (x/d = 0.5) of the sphere up to a distance of 25d. Figure 3.20 shows a comparison of the numerical data obtained in this study, the numerical data presented in [59] for Re_s = 300, and the experimental data from [58] for Re_s =280. The data from the present study shows an identical behaviour to the validation study 2. With the exception of the simulation conducted with the laminar model. The overall shape of this data follows a

similar pattern to the results from the k-ω SST and Transition SST, but the curve follows an undulatory trajectory when the velocity of the wake approaches the freestream velocity. It seems that it could be possible to utilise the laminar model to solve these type of simulations. However, special methods would need to be applied to deal with the numerical noise.

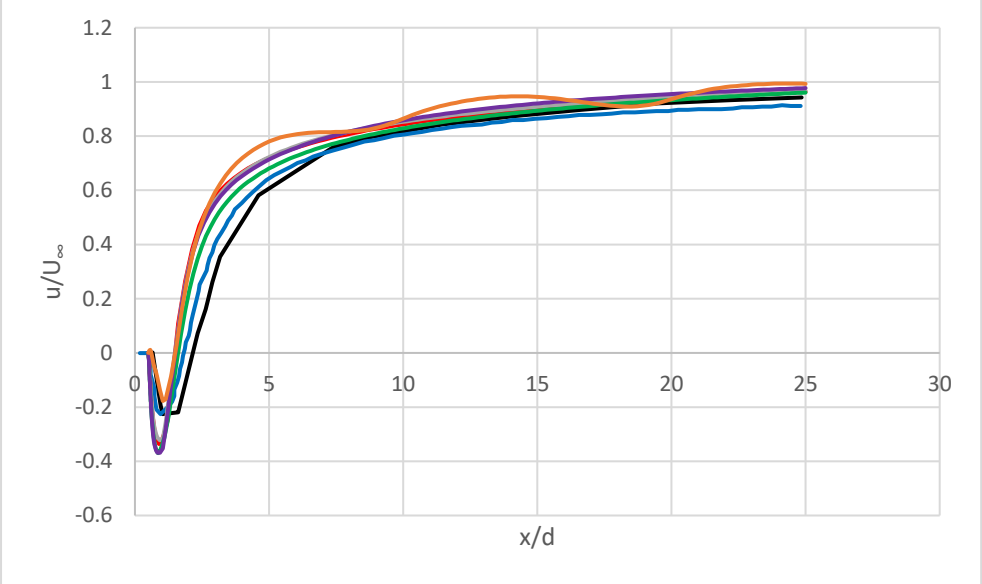

Figure 3.20 Streamwise velocity comparison [black line: experimental data from [58] for Re_s = 280; blue line: numerical data from [59] for Re_s = 300; red line: present study P4 k-ω SST for Re_s = 400; grey line: present study P5 k-ω SST for Re_s = 400; green line: present study P6 k-ω SST for Re_s = 400; purple line: present study P5 Transition SST for Re_s = 400; orange line: present study P5 laminar for Re_s = 400;].

Pressure distribution

Mesh P6 is the closes to the values reported in [59], closely followed by P5 and P4. The laminar flow show a pressure distribution close to P2 and P3, but it predicts an asymmetric distribution of the C_p on the back of the sphere, while the other viscous models show a more centred location. Although, the flow visualization shows a symmetric wake for the turbulence models, the C_p contour plot on the surface of the sphere (figure 3.21) indicates that the wake may have a minor inclination. Additionally, when compared to the other models, the Transition SST predicts a greater pressure drop (figure 3.22).

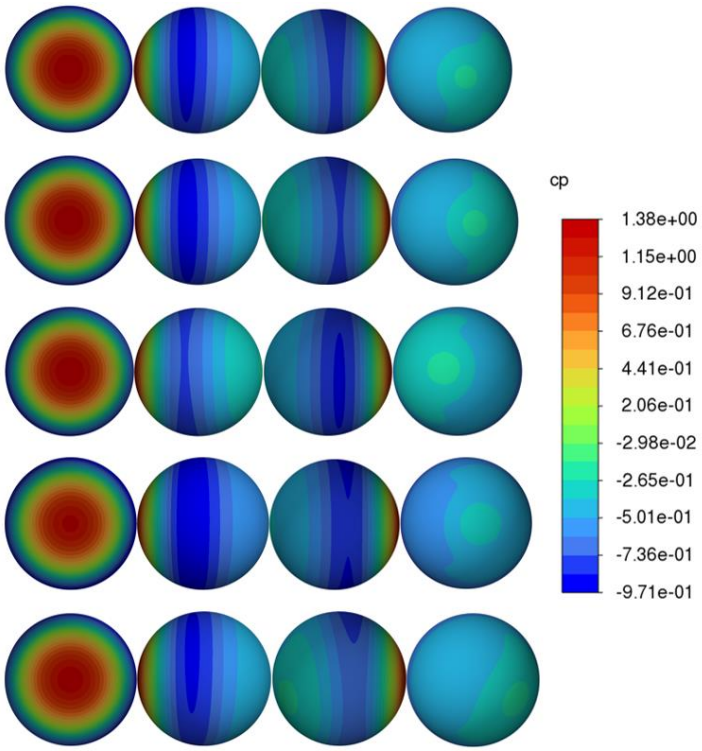

Figure 3.21 Pressure coefficient on the sphere surface. From top to bottom: P4 k-ω SST, P5 k-ω SST, P6 k-ω SST, P5 Transition SST, P5 laminar. From left to right: front view, right view, left view, rear view.

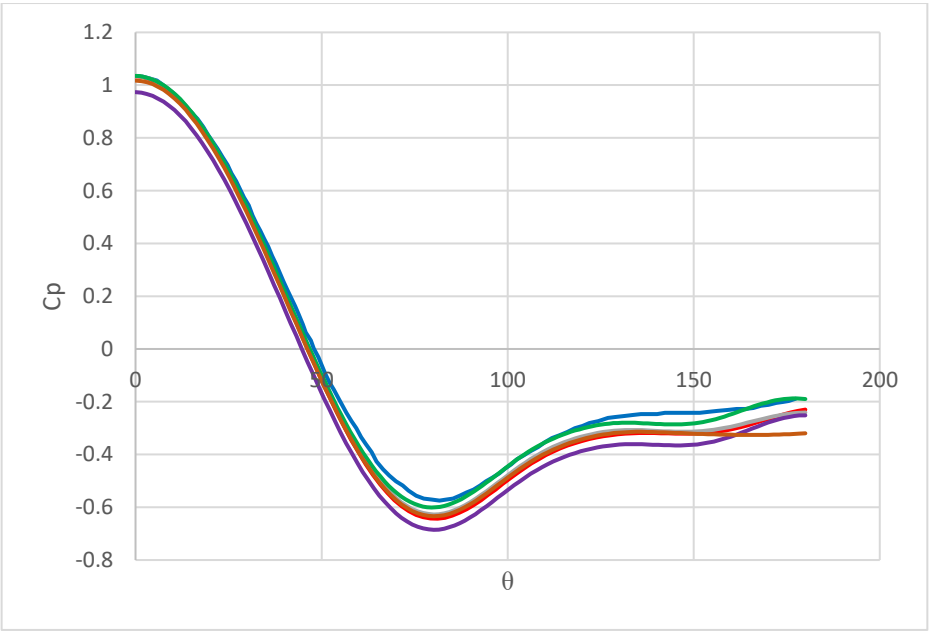

Figure 3.22 Pressure distribution [blue line: data from [59] Re_s=300; red line: P4 k-ω SST Re_s=400; grey line: P5 k-ω SST Re_s=400; green line: P6 k-ω SST Re_s=400; purple line: P5 Transition SST Re_s=400; orange line: P5 laminar Re_s=400].

Drag coefficient

The values of the C_d obtained through simulations in the present study are shown in table 3.11. The three values of C_d for the meshes P4, P5, and P6 are close to the values presented in [58] and [59] for a Re_s of 400. Moreover, they show a marginally greater correlation than the meshes P1, P2, and P3 from the previous validation study. Despite the meshes on the sphere's surface and refinement region having the same element sizes. Therefore, the minor difference in C_d may be caused by the presence of the boundary layer on the pipe wall, and its interaction with the flow around the sphere.

Both the Laminar and Transition SST models predicted a marginally more accurate value than the simulations done with the same mesh and the k-ω SST model. The simulation with the laminar viscous model presented periodic oscillations in the output value of the drag force. Thus, the drag force was calculated by averaging the value for the last 500 iterations.

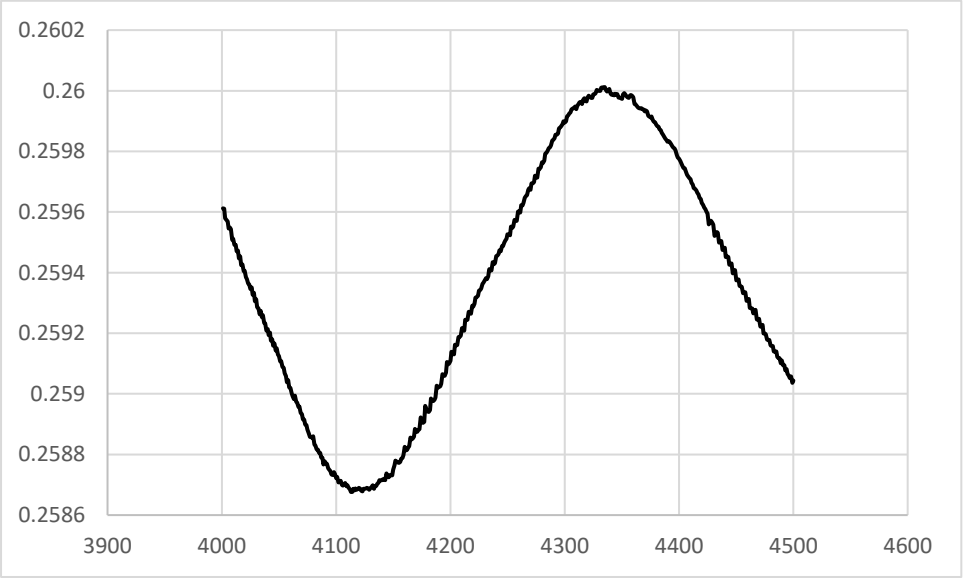

Figure 3.23 Last 500 iterations of the drag force value calculated with the laminar model.

Case	Cell count	C_d
Re_s = 400 (exp.) [58]	None	0.603
Re_s = 400 (num.) [59]	Unknown	0.599
P4 k-ω SST	1003271	0.627
P5 k-ω SST	1579916	0.630
P6 k-ω SST	2627032	0.617
P5 Transition SST	1579916	0.624
P5 Laminar	1579916	0.623

Table 3.11 Drag coefficient.

3.3.3 Conclusion

The validation study 3 was a direct continuation of the work done in the validation study 2. This study aimed to replicate the confined conditions of a sphere inside a pipe with a no-slip condition on the pipe walls. The activation of the no-slip condition causes the creation of a boundary layer on the pipe walls, which in turn increases the complexity of the flow around the sphere by interacting with it. Furthermore, the application of the no-slip condition caused the apparition of a second Reynolds number that could be considered. The sphere Re (Re_s) was 400, while the pipe Re (Re_p) was 5600. These Re implied different flow regimes. Thus, another objective of this validation study was to test three viscous models: k-ω SST, Transition SST, and Laminar.

The Laminar model presented issues with numerical noise for the streamwise velocity and drag coefficient. This last one had to be calculated by averaging the value of the last 500 iterations. As for the k-ω SST and Transition SST models, they did not present issues with numerical noise. The pressure distribution calculated by the Transition SST deviated noticeably from the other models. On the other hand, it obtained a C_d marginally closer to the expected value from literature than the k-ω SST.

Furthermore, by observing the results of the simulations it can noted that, despite the presence of a boundary layer on the pipe wall, the drag force acting on the sphere was not too dissimilar from the one obtained in validation study 2. Two particularities of this study should be mentioned. Firstly, because of the short distance from the inlet to the sphere, the flow was not fully developed when it reached the sphere. As a result, the flattened parabolic flow profile expected from a turbulent flow did not appeared. Secondly, the blockage ratio was BR $\approx$ 0.071. Thus, it might be the case that, because of the considerable difference between the sphere and the pipe diameters, there was not enough interaction.

3.4 Discussion and conclusion

The purpose of the chapter was to create the foundation on which the Computational Fluid Dynamics simulations of the future chapter were built upon. In particular, it had the objective of finding suitable boundary conditions and settings to analyse the drag coefficient and pressure distribution. Since these are key parameter for optimizing the design of the robot's body. By accurately measuring and minimizing drag, it is possible to reduce the robot's energy consumption and enhance its efficiency.

Firstly, Validation study 1 replicated the experimental set up used in [58] to ensure that future simulations were grounded on experimental data. Then, Validation study 2 utilised the boundary conditions proposed in [59] to simulate a sphere inside a pipe flow. Finally, utilising an identical geometry than Validation study 2, Validation study 3 aimed to observe the effect of the pipe boundary layer on the flow around the sphere, as well as evaluating multiple viscous models to determine their impact on the drag coefficient and pressure distribution.

The three validation studies predicted values of C_d for a Re_s = 400 marginally higher than the reference data. Considering that, the utilised boundary conditions coincided with the ones proposed in [59], and several viscous models were tested, it seems to be the case that these discrepancies in the drag coefficient are caused by the mesh quality. Although, the meshes utilised

for this study were designed to be within the recommended quality guidelines, due to the software selection, it was necessary to utilised unstructured meshes in areas closer to the sphere surface. Conversely, the reference numerical study employed a completely structured mesh. The structured mesh probably provided a superior accuracy in capturing the flow dynamics in the areas close to the sphere.

Despite these discrepancies, the results of Validation case 3, which has a blockage ratio BR $\approx$ 0.071, showed good agreement with the validation studies. This indicating that the boundary layer formed on the pipe wall had a negligible effect on the flow around the sphere due to the significant difference between the sphere and pipe diameters. However, the incomplete flow development before reaching the sphere could have affected the pressure distribution and drag coefficient. To address this, simulations in future chapters the distance from the inlet to the sphere was increased. Nonetheless, the findings in study 3 connected validation studies 1 and 2 to the simulations that were carried out in the next chapter of this thesis. Such simulations modelled spheres inside pipes of varying diameters and blockage ratios.

3.4.1 Future simulation settings

The k-ω SST turbulence model demonstrated the ability to predict drag and pressure distribution around the sphere with acceptable accuracy. Thus, it was chosen to be used in the simulation in future chapters. The majority of the simulations in the two subsequent chapters have Re_p in the turbulent regime. Additionally, k-ω SST showed to be capable of predicting the C_d with an acceptable accuracy for a sphere with a Re_s in the laminar regime. Additionally, the selected settings for future work include the k-ω SST turbulence model, Green-Gauss node-based gradients, SIMPLE algorithm for pressure-velocity coupling, and second-order discretization schemes for both pressure and momentum.

Simulation settings	Details
Solver	Steady state
Viscous model	K-ω SST
Pressure-Velocity coupling	SIMPLE
Discretization	Green-Gauss node based, second order for pressure, and second order upwind for momentum.
Boundary conditions	Velocity-inlet, pressure-outlet, no-slip boundary condition on the sphere and pipe wall, symmetry

Table 3.12 Selected setting for the simulations to be conducted in chapters 4 and 5.

Chapter 4 Effects of the Pipe Diameter and Dynamic Viscosity

This chapter aims to explain a series of Computational Fluid Dynamics (CFD) simulations conducted to explore the fluid-structure interactions between a spherical object and the surrounding fluid within the constrained environment of a pipe. The objective of these simulations was to analyse the flow characteristics and resulting forces on a sphere as it navigates through pipes of varying diameters and fluid viscosities. This approach allows for a systematic investigation of how changes in these parameters influence the flow patterns, pressure distributions, and drag forces acting on the sphere, providing insights into the behaviour of spherical objects in confined fluid environments, which is an essential step for the purpose of developing an inspection robot for oil pipelines.

4.1 Geometry design

The 3D models used in the CFD simulations were designed to represent the flow environment of a spherical robot inside cylindrical pipes of varying diameters. Five distinct pipe geometries were created, each with an internal diameter of 1.0668 m (42 in), 0.9144 m (36 in), 0.762 m (30 in), 0.6096 m (24 in), and 0.508 m (20 in), respectively. All pipes have a length of 20 meters, providing a sufficient domain for the fluid flow to develop fully before and after interaction with the robot’s body which was modelled as a sphere with a diameter of 0.2 m. A representation of the geometry can be seen in figure 4.1.

Pipe name	Pipe diameter (in)	Pipe diameter (m)	Blockage ratio
D1	42	1.0668	0.187
D2	36	0.9144	0.219
D3	30	0.762	0.262
D4	24	0.6096	0.328
D5	20	0.508	0.394

Table 4.1 List of diameters.

In order to ensure an accurate simulation of the flow, the same approach was followed as in the validation studies, and the length of each pipe was divided into two segments. The first segment, extending 11 meters from the inlet to the centre of the sphere, was designed to allow the flow to achieve a fully developed profile before encountering the robot. However, in many practical applications the entrance effects become negligible after a distance of approximately 10D (D is the pipe diameter) [60]. Then, the second segment, extending 9 meters from the centre of the sphere to the outlet, was created to ensure that the downstream effects of the sphere on the fluid flow could be captured without interference from boundary conditions.

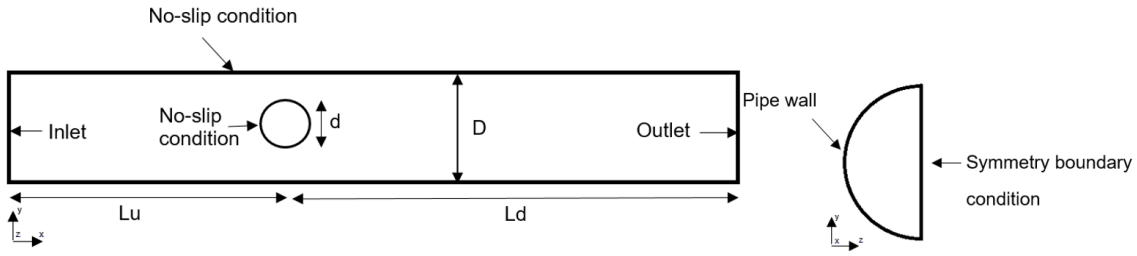

Figure 4.1 3D model of the flow domain.

Furthermore, in order to reduce computational time and resources requirements, the pipe geometry was cut in half longitudinally, and only the left side was modelled. This allowed for the application of a symmetry boundary

condition along the longitudinal plane, effectively reducing the computational domain by half.

Variable	Symbol	Dimensions (m)
Pipe diameter	D	1.0668, 0.9144, 0.762, 0.6096, 0.508
Sphere diameter	d	0.2
Distance from the inlet to the centre of the sphere	Lu	11
Distance from the centre of the sphere to the outlet	Ld	9

Table 4.2 List of dimensions.

The selection of the robot's size was based on preliminary calculations aimed at determining the necessary thrust for the robot to maintain a static position against the flow. Utilising the equation 8 for the drag force [60]:

$$F_D = C_d A \frac{\rho V^2}{2} \quad (8)$$

For a sphere in a laminar regime of Re ≤ 2x10^5 it is possible to assume a $C_d \approx 0.5$ [60]. Assuming a fluid density of 800 kg/m^3, a flow velocity of 1 m/s, and using the sphere diameter of 0.2 m, then F_D = 6.283 N. It is important to mention that the reasons for the selection of the fluid density and flow velocity will be explained in the boundary conditions section of this chapter.

Following these calculations, an extensive search was conducted for commercially available components that met the required specifications, resulting in the choice of the smallest feasible size for the robot. This is only taking into account the basic a components a robot would need to propel itself

against the current and carry out a basic inspection. The components were: an underwater motor with a thrust of 9.8 N, voltage of 11.1 V, torque 0.25 N·m; 2 LiPo batteries with 11.1 V and 6500 mAh; a commercial hydrophone; an Arduino UNO; and a 6-axis motion tracking accelerometer & gyroscope. It is important to mention that the underwater motor would be located outside the robot. Therefore, its dimensions were not taken into account for this preliminary geometry design. Also, these components are not ideal for the final robot. However, they work as an initial guess for the geometry design of this CFD study.

4.2 Mesh design

Utilising the software Ansys Fluent meshing, the required meshes for this study were designed to capture the complex fluid dynamics around the sphere while ensuring computational efficiency and accuracy. To determine the optimal mesh, a mesh independence study was conducted using the pipe with the largest diameter (D1) and the lowest viscosity μ6 (explained in boundary conditions section). Three different meshes were tested to ensure that the simulation results, particularly the forces and flow patterns around the sphere, were independent of the mesh resolution.

4.2.1 Mesh Independence Study

The mesh independence study involved creating three meshes with different levels of refinement, particularly on the sphere's surface to accurately capture the pressure and shear forces. The list of meshes and their parameters can be seen in table 4.3.

Mesh properties	A1	A2	A3
Pipe element size (m)	0.042	0.0546	0.07098
Pipe first cell height (m)	$6.5x10^{-5}$	$6.5x10^{-5}$	$6.5x10^{-5}$
Pipe growth ratio	1.116	1.151	1.197
Pipe inflation layers	53	43	36
Wake element size (m)	0.008	0.0104	0.0135
Sphere element size (m)	0.002	0.0026	0.00338
Sphere first cell height (m)	$5x10^{-5}$	$5x10^{-5}$	$5x10^{-5}$
Sphere growth ratio	1.117	1.1521	1.1977
Sphere inflation layers	28	24	20
Cell count	3222246	1701658	899900

Table 4.3 Mesh independence study: fine mesh A1; medium mesh A2; and coarse mesh A3.

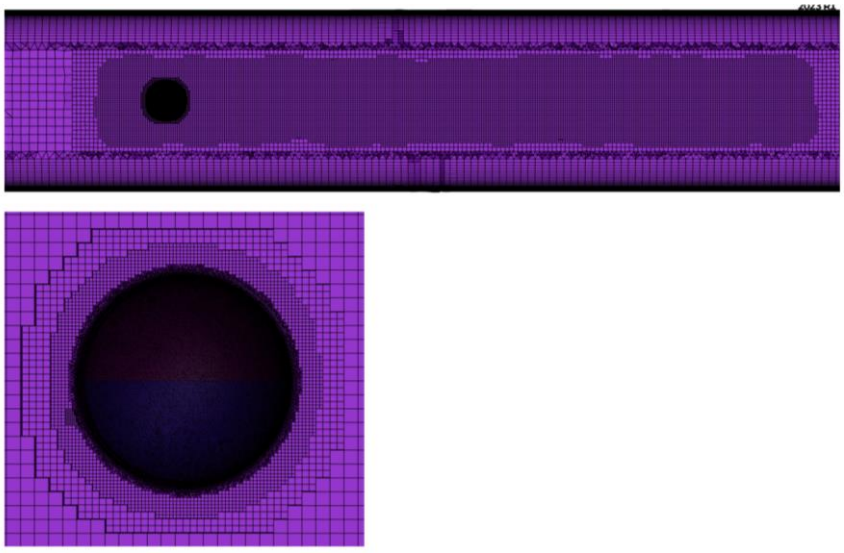

Figure 4.2 Mesh A1.

After running simulations with each mesh, the results were analysed using the drag coefficient to assess the impact of mesh resolution. The comparison showed that A2 provided results that were within an acceptable margin of error when compared to A1. Furthermore, it required significantly lower computational requirements with the simulation running in half the time than with A1. Therefore, mesh A2 was selected as the optimal mesh configuration for subsequent simulations.

Mesh	C_d
A1	0.256
A2	0.252
A3	0.261

Table 4.4 Drag coefficients of the mesh independence study with pipe D1.

4.2.2 Mesh Design for Different Pipe Diameters

Once the optimal mesh resolution was established for the largest pipe, the meshes for the five remaining pipes were designed utilising its parameters as a guide. Since the sphere's size will remain the same across all pipes, the same mesh resolution was applied to all the cases. On the other hand, to ensure uniform mesh quality for the pipes of different diameters, the element size on the pipe's surface was scaled proportionally to each pipe's diameter. This was done in order to maintain the same number of elements along the pipe perimeter.

Additionally, the inflation layer mesh was also modified for each pipe diameter. Since every pipe was going to be used to conduct simulations with a wide range of viscosities and Re, the meshes needed to have a first cell height small enough to have a $y+ \approx 1$ for the highest Re, while at the same time having an inflation layer tall enough to capture the boundary layer for the lowest Re. The first cell height was selected for the case with the highest Re and together with the growth ratio were kept constant across all meshes. However, the number

of layers and the total height of the inflation layer were scaled according to the pipe diameter. The total height of the inflation layers across all pipes was of approximately D/5.6.

4.3 Boundary conditions and solver settings

The boundary conditions for the CFD simulations were selected based on the work done in the validations studies in Chapter 3. Figure 4.1 shows a representation of the pipe including the boundary conditions. The same conditions were applied to the simulations of all the pipe diameters. The solely exception being the dynamic viscosity, which will be varied to analyse its effect on the forces and flow around the sphere.

A velocity inlet boundary condition was applied at the entrance of the pipe. The inlet velocity was set to 1 m/s, a value chosen after discussions with a pipeline operator since, according to the contact, it is an approximate value for the flow velocity for subsea pipelines. Then, at the outlet of the pipe, a pressure outlet boundary condition was applied, with the pressure set to 0 Pa (gauge pressure). Additionally, a symmetry boundary condition was applied along the longitudinal plane of the pipe, where the pipe was cut in half. This condition assumes that the flow on one side of the plane is a mirror image of the flow on the other side, effectively reducing the computational domain without affecting the results. Finally, a no-slip boundary condition was applied to the pipe walls and the surface of the sphere.

In the same consultation process with the pipeline operator, it was mentioned that, in the case of subsea pipelines between 20 to 42 inches, viscosity can range from 0.00125 to 0.0025 Pa·s. However, these values are not representative of transportation conditions in different regions. As pointed out by Munoz J. A. D. [62], different countries have their own recommendations about the maximum viscosities for the transportation of crude oil by pipeline. As mentioned in the same paper, for diluted extra heavy crude oil, countries as Canada and Venezuela recommend maximum viscosities of up to 0.35 Pa·s and 0.4 Pa·s respectively [62].

Therefore, to evaluate the impact of fluid viscosity on the flow dynamics around the spherical robot, six different viscosities were selected. The lowest was 0.001003 Pa·s, the viscosity of water at 20 °C, and 0.4 Pa·s was selected as the highest viscosity, the maximum recommended viscosity for the transportation of crude oil by pipeline as found in literature[62]. The remaining four values were obtained through an equation for exponential growth between the two aforementioned values. Finally, the fluid density was set to 800 kg/m^3, a value selected through the same consultation process used to determine the inlet velocity and viscosity, and was kept constant through all the simulations.

Viscosity name	**Viscosity (Pa·s)**
μ1	0.4
μ2	0.120756
μ3	0.036455
μ4	0.011005
μ5	0.003322
μ6	0.001003

Table 4.5 List of viscosities.

As shown in tables 4.6 and 4.7, this simulation covered a wide range of both Re_s and Re_p. In the validation study in Chapter 3, the K-ω SST turbulence model proved being capable of predicting the forces acting on a sphere with an acceptable precision for a Re_s = 400. Thus, the following settings were chosen: steady-state simulation, K-ω SST turbulence model, SIMPLE, Green-Gauss node based, second order for pressure, and second order upwind for momentum. A complete list of the boundary conditions and settings is in table 4.8.

Viscosity	20in / 0.508 m	24in / 0.6096 m	30in / 0.762 m	36in / 0.9144 m	42in / 1.0668 m
μ1	1016	1219	1524	1828	2133
μ2	3365	4038	5048	6057	7067
μ3	11148	13377	16722	20066	23410
μ4	36927	44312	55391	66469	77547
μ5	122320	146785	183481	220177	256874
μ6	405184	486221	607776	729332	850887

Table 4.6 Re_p for the combinations of viscosities and pipe diameters.

Viscosity (Pa·s)	Re_s
μ1	400
μ2	1324.987
μ3	4388.98
μ4	14538.36
μ5	48157.866
μ6	159521.436

Table 4.7 Reynolds number for the sphere for different viscosities.

Boundary condition / properties	Details
Solver	Steady-state
Viscous model	K-ω SST
Inlet (velocity)	1 m/s
Outlet (Pressure)	0 Pa
Walls (pipe)	No-slip boundary condition
Walls (sphere)	No-slip boundary condition
Density (kg/m^3)	800
Viscosities (Pa·s)	0.4, 0.120756, 0.036455, 0.011005, 0.003322, 0.001003
Pressure-Velocity coupling	SIMPLE
Discretization	Green-Gauss node based, second order for pressure, and second order upwind for momentum.

Table 4.8 Boundary conditions and settings.

4.4 Analysis

This section presents the results of the CFD simulations, with a particular focus on the effects of varying pipe diameters and fluid viscosities on the drag force experienced by the spherical robot and the pressure distribution around it. The analysis aims to elucidate the key fluid dynamics phenomena that influence the robot's performance in different flow conditions.

4.4.1 Effect of pipe diameter on drag coefficient and pressure distribution

The simulations revealed a clear relationship between pipe diameter and the drag coefficient (C_d) of the spherical robot. As the pipe diameter increases, the C_d of the robot decreases. Figure 4.3 shows how all the viscosities present a similar decrease of C_d. Additionally, it can be seen that the higher the viscosity, the more pronounced the decrease of C_d is with the increase of the pipe diameter.

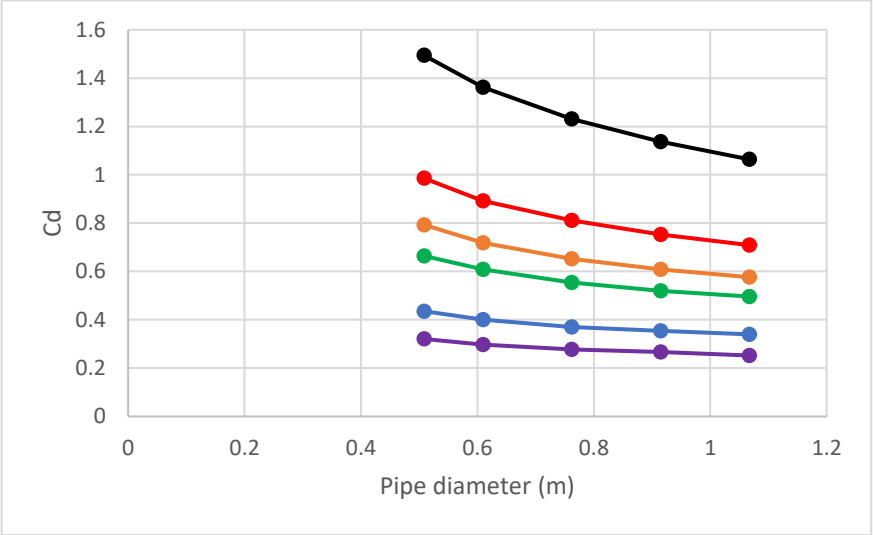

Figure 4.3 Effect of the pipe diameter on the pressure coefficient [black line: μ1; red line: μ2; orange line: μ3; green line: μ4; blue line: μ5; purple line: μ6].

The total drag force is composed of the pressure drag plus the viscous drag. Figures 4.4 and 4.5 show how the portion these forces make of the total drag force evolve with the change in diameter. Overall, both remain quite stable with the change in diameter. Except for a minor decrease in the pressure drag as the pipe diameter increases, while the viscous drag shows the opposite behaviour.

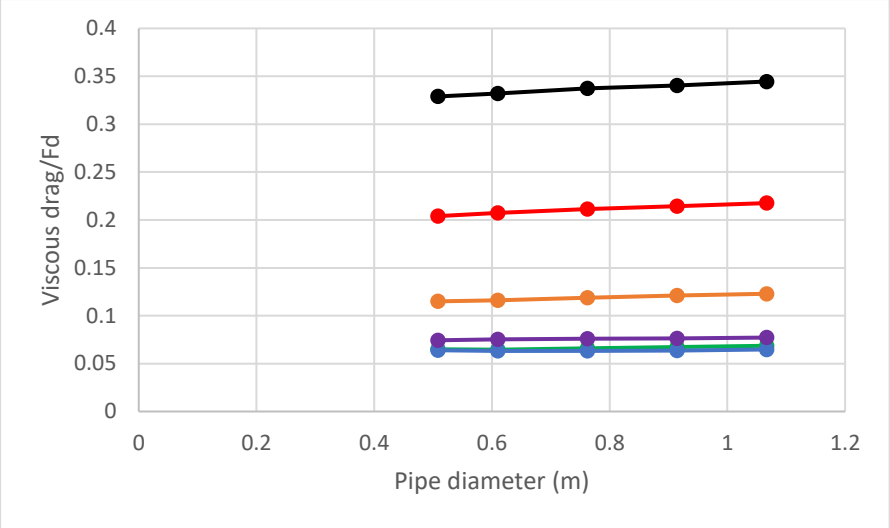

Figure 4.4 Effect of the pipe diameter on the portion of the total drag force the viscous drag represents [black line: μ1; red line: μ2; orange line: μ3; green line: μ4; blue line: μ5; purple line: μ6].

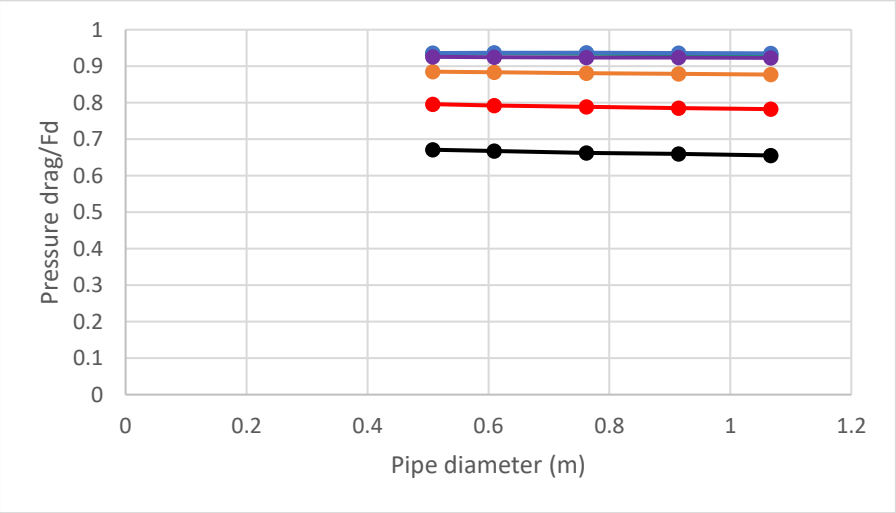

Figure 4.5 Effect of the pipe diameter on the portion of the total drag force the pressure drag represents [black line: μ1; red line: μ2; orange line: μ3; green line: μ4; blue line: μ5; purple line: μ6].

The decrease of C_d with the increase of the diameter could be attributed to the reduction of the blockage ratio, and thus, increment of the cross-sectional area available for the fluid to flow around the sphere. This results in a reduction in flow velocity and pressure gradients near the sphere's surface. This can be observed in figure 4.6, which shows how the x-component of the velocity increases with the decrement of the pipe diameter.

As a result, for the smallest pipe diameter D5, the drag force is significantly higher due to the restricted flow area, which causes the fluid to accelerate as it moves around the robot. This acceleration leads to an increase in pressure, especially in the region directly upstream of the sphere (figure 4.7). The high-pressure region at the front of the sphere, combined with a low-pressure region at the rear, contributes to the drag force.

As the pipe diameter increases, the flow has more space to circumvent the sphere, leading to a more gradual pressure gradient and reduced pressure differential between the front and rear of the robot. This reduction in pressure differential implies a lower drag force for larger pipe diameters.

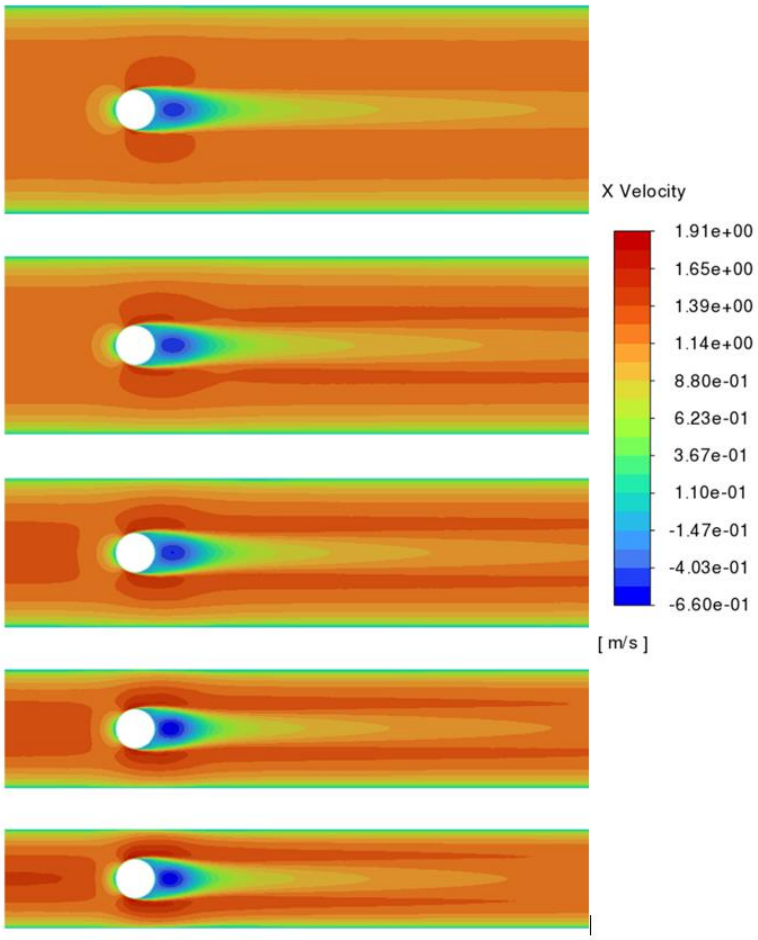

Figure 4.6 Flow velocity x-component comparison for the different diameters with a viscosity μ2. From top to bottom: D1, D2, D3, D4, D5.

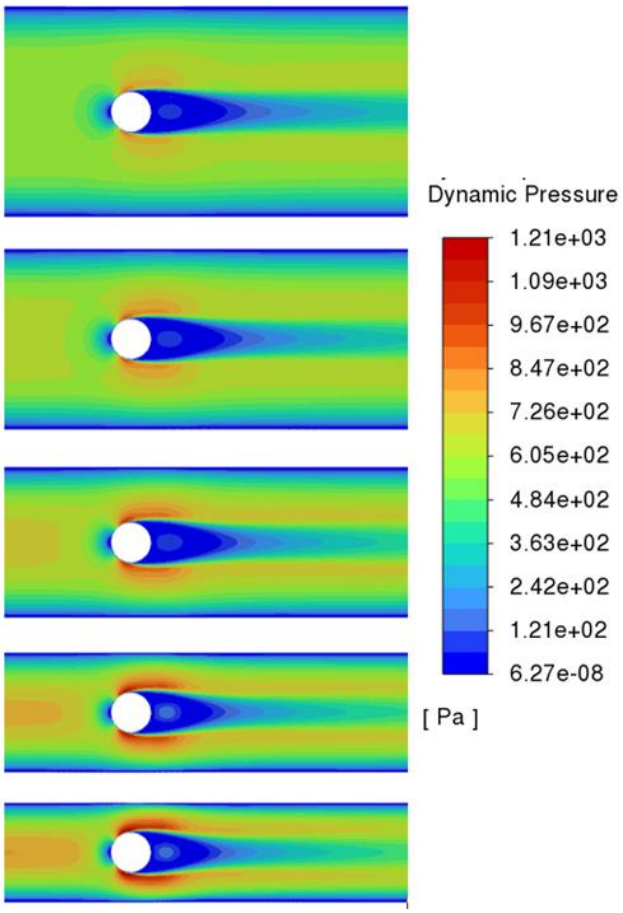

Figure 4.7 Dynamic pressure comparison for the different diameters with a viscosity μ2. From top to bottom: D1, D2, D3, D4, D5.

4.4.2 Effect of fluid viscosity on drag coefficient and pressure distribution

As seen in figure 4.8, across all pipe diameters, higher fluid viscosities result in an increase in the drag coefficient on the sphere. This increment of the drag forces could be attributed to the viscous forces acting on the sphere's surface. Figures 4.9 and 4.10 show how the portions the viscous and pressure drag forces make of the total drag force evolve with the change in viscosity. Contrary to the increase in pipe diameter, the increase in viscosity has a more noticeable effect on these forces. While the pressure drag for μ1 (the highest viscosity) is approximately three times the pressure drag for μ6 (the lowest viscosity), the viscous drag for μ1 is approximately nineteen times the viscous drag for μ6. Table 4.9 shows the values of pressure and viscous drag for the pipe D1 across all the viscosities.

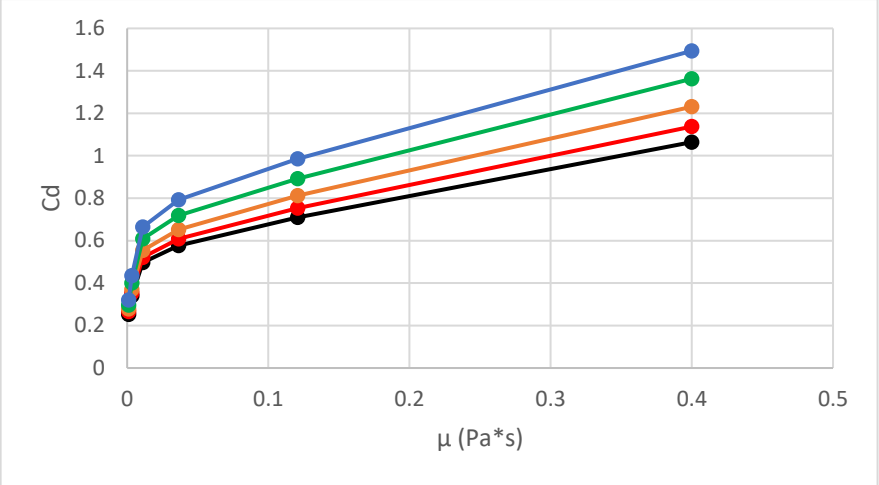

Figure 4.8 Effects of the viscosity on the drag coefficient.

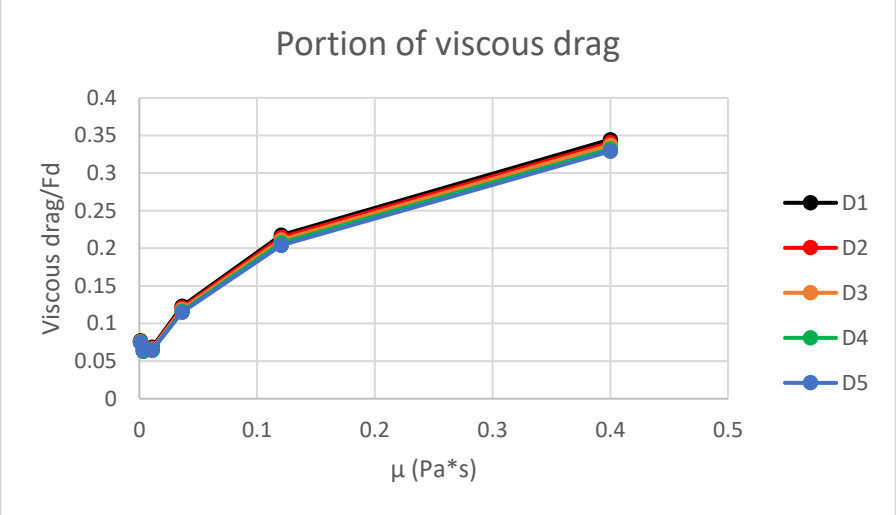

Figure 4.9 Portion of the viscosity drag in the drag force.

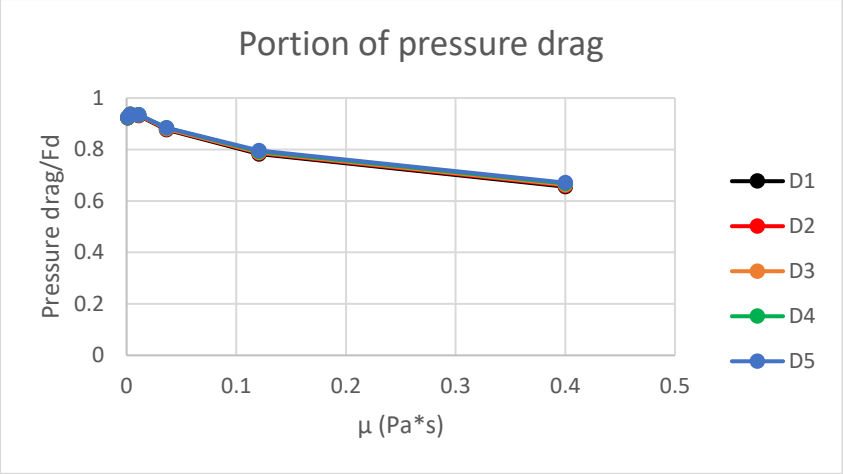

Figure 4.10 Portion of the pressure drag in the drag force.

Viscosity	Pressure drag (N)	Pressure drag/F_d (N)	Viscous drag (N)	Viscous drag/F_d (N)	Total drag (N)
μ1	4.382	0.655	2.304	0.344	6.686
μ2	3.485	0.782	0.969	0.218	4.455
μ3	3.176	0.877	0.445	0.123	3.622
μ4	2.904	0.931	0.214	0.069	3.118
μ5	1.997	0.935	0.138	0.065	2.135
μ6	1.463	0.923	0.122	0.077	1.585

Table 4.9 Pressure and viscous drag values across all viscosities for pipe D1.

Low viscous fluids flow easier around the object. This results in a smoother pressure distribution around the sphere and a lower drag force (see table 4.9). In general, the pressure differential between the front and rear of the sphere becomes less pronounced with lower viscosities. Although, as can be seen in figure 4.11, the viscosity with the smallest differential between the front and back of the sphere is μ4.

Additionally, figure 4.11 shows how for higher viscosities the resulting pressure distribution around the sphere is more gradual. Moreover, the pressure recovery in the wake region is shown to be slower for higher viscosities, which

correlates with higher drag forces for high viscosities, and lower drag forces for lower viscosities.

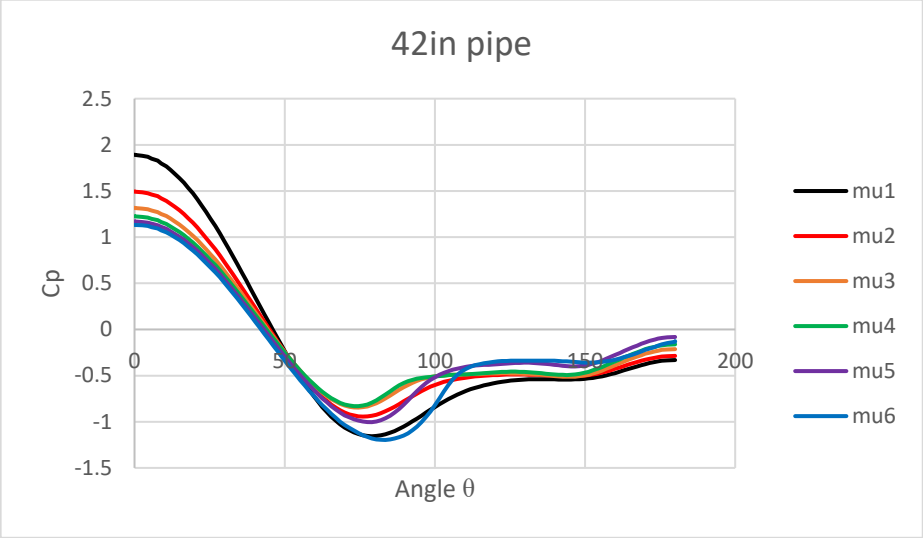

Figure 4.11 Pressure distribution across all viscosities within a pipe of diameter 1.0668 m.

4.5 Discussion and conclusion

This chapter presented an analysis of the fluid dynamics surrounding a spherical object inside pipes of varying diameters and fluid viscosities. The primary objectives were to evaluate the impact of these variables on the drag force exerted on the robot and to assess the resulting pressure distribution, with the objective of informing design decisions to optimize the performance of a robot for pipeline inspections.

The simulations demonstrated that both pipe diameter and fluid viscosity significantly influence the drag force and pressure distribution experienced by a spherical robot. Particularly, a decrement of the pipe diameter was associated with an increment of the drag forces. This was because, as the blockage ration increases, the fluid around the spherical robot accelerates, which leads to a steeper pressure gradients around the sphere. Conversely, larger pipe diameters allow the flow to pass the robot more easily, reducing drag forces and creating a more gradual pressure distribution.

Moreover, this study also showed the effect the viscosity has on the drag forces. Higher viscosities lead to an increase in the pressure and viscous drag, with a considerably more noticeable effect on the second one.

In conclusion, this study provided valuable insights into the fluid dynamics affecting a spherical robot inside a pipe, with a focus on how variations in pipe diameter and fluid viscosity influence drag forces and pressure distributions. The results of this study indicate that, as the pipe diameter becomes smaller or the viscosity higher, a robot requires more thrust to maintain the same velocity. However, a potential method for reducing drag is to explore alternative geometries that are more streamlined than a sphere. Adopting a more streamlined shape could reduce flow separation, minimize the size of the wake, and ultimately decrease the drag force, thereby lowering the required thrust for propulsion.

Chapter 5 Effects of the Robot's Geometry and Vertical Position

The previous chapter investigated the fluid dynamics around a spherical robot within pipes of varying diameters and fluid viscosities, utilizing Computational Fluid Dynamics (CFD) simulations to monitor the impact on drag force and pressure distribution. The results indicated that smaller pipe diameters and higher fluid viscosities significantly increased drag. This in turn, increases the required thrust for the robot to maintain its position against the flow. A counter measure is to modify the geometry of the robot to a more streamlined shape to reduce drag and improve efficiency.

Therefore, this chapter explores the effect of modifying the robot's geometry to minimize drag in a pipe environment. In order to achieve this, the spherical robot was elongated to create three different ellipsoidal shapes, with the purpose of reducing flow separation and minimizing the wake size. The performance of the sphere and these new designs was evaluated utilising CFD simulations. These simulations were conducted for each shape within a pipe of a fixed diameter and fluid viscosity. The selected variables were D3 (30 in or 0.762 m) and μ4 (0.011 Pa·s) from the study conducted in the previous chapter. Since these variables are approximately in the middle of the range of the previous study, it is expected that they could provide a balanced perspective on the flow characteristics.

Since the environment inside an oil pipeline is a harsh one, the robot may not always be perfectly centred within the pipe due to operational constraints or flow-induced perturbations. Thus, in addition to analysing the sphere and ellipsoids at the pipe's central axis, this study examines the impact of the vertical position of the robot inside the pipe. Specifically, two vertical positions, 0.1 m and 0.2 m above the centre of the pipe, were tested.

The objectives of this study are: firstly, to analyse the effect elongating the robot into an ellipsoidal shape has on drag reduction; secondly, to assess how

varying the robot's position within the pipe affects the flow and forces acting on the robot. The results will provide critical insights into the optimal design for robotic systems intended for use in pipe environments.

5.1 Geometry design

As previously mentioned, the pipe D3 with a diameter of 0.762 m will be used for this study. The pipe has a total length of 20 m, with 11 m from the inlet to the robot's centre and 9 m from the robot's centre to the outlet. This setup ensures that the flow fully develops before interacting with the robot and provides sufficient downstream length to capture the effects of the robot on the flow field. The decision to maintain the same pipe dimensions ensures that any changes in flow behaviour can be attributed to the modifications in the robot's geometry and position rather than variations in the pipe configuration.

The robot's base diameter remains consistent with the previous study at 0.2 m. However, in this case, the object was elongated to create three extra shapes in the form of ellipsoids with lengths of 0.4 m (E1), 0.6 m (E2), 0.8 m (E3).

Geometry	Diameter (m)	Length (m)	L/d
E0 (sphere)	0.2	0.2	1
E1	0.2	0.4	2
E2	0.2	0.6	3
E3	0.2	0.8	4

Table 5.1 Ellipsoid dimensions.

Additionally, positional variations were introduced in order to simulate scenarios where the robot may not be perfectly centred. The ellipsoidal models were tested at three different vertical positions within the pipe to assess the impact of positioning relative to the pipe wall. At H0 the ellipsoid is centred

within the pipe (0 m height); At H1 the ellipsoid is offset by 0.1 m above the centre of the pipe; finally, at H2 the ellipsoid is offset by 0.2 m above the centre of the pipe.

5.2 Mesh design

5.2.1 Mesh independence study

To ensure the reliability of the CFD simulations, a mesh independence study was conducted for each of the three ellipsoids. Three meshes of varying resolutions were created for each of the three ellipsoidal shapes, resulting in the creation of nine distinct meshes. A list of these meshes can be seen in table 5.2. Moreover, the study was performed with the ellipsoids positioned at the centre of the pipe (0 m height), ensuring that the selected mesh would maintain an acceptable accuracy to computational cost ratio.

Each of these meshes was evaluated based on the resulting drag coefficient (table 5.3) and pressure distribution (figures 5.1, 5.2, and 5.3) around the ellipsoid. The results were compared to determine whether further mesh refinement led to significant changes in the simulation results. For each ellipsoid, the three meshes proved to have a similar level of accuracy. Thus, proving that the results were independent of the mesh. Despite the fact that, the third mesh for each ellipsoid proved have a similar accuracy with an even lower computational cost, the second mesh was chosen because it has the same resolution than the meshes utilised in the previous study. As a result, the second mesh (E1.2, E2.2, and E3.2) was selected to be used for the remaining simulations of this study.

Mesh	Pipe elem. size (m)	Pipe first cell height (m)	Pipe growth ratio	Pipe infl. layers	Wake elem. size (m)	Sphere elem. size (m)	Sphere first cell height (m)	Sphere growth ratio	Sphere infl. layers	Cell count
E1.1	0.042	6.5×10^{-5}	1.1164	46	0.008	0.002	5×10^{-5}	1.117	23	3245337
E1.2	0.0546	6.5×10^{-5}	1.15132	38	0.0104	0.0026	5×10^{-5}	1.1521	20	2352968
E1.3	0.07098	6.5×10^{-5}	1.196716	31	0.01352	0.00338	5×10^{-5}	1.19773	17	1276968
E2.1	0.042	6.5×10^{-5}	1.1164	46	0.008	0.002	5×10^{-5}	1.117	23	5175570
E2.2	0.0546	6.5×10^{-5}	1.15132	38	0.0104	0.0026	5×10^{-5}	1.1521	20	2806952
E2.3	0.07098	6.5×10^{-5}	1.196716	31	0.01352	0.00338	5×10^{-5}	1.19773	17	1524453
E3.1	0.042	6.5×10^{-5}	1.1164	46	0.008	0.002	5×10^{-5}	1.117	23	6050096
E3.2	0.0546	6.5×10^{-5}	1.15132	38	0.0104	0.0026	5×10^{-5}	1.1521	20	3272325
E3.3	0.07098	6.5×10^{-5}	1.196716	31	0.01352	0.00338	5×10^{-5}	1.19773	17	1767572

Table 5.2 Characteristics of the 9 meshes of the mesh independence study.

Mesh	Cells	C_d
E1.1	3245337	0.214
E1.2	2352968	0.216
E1.3	1276968	0.215
E2.1	5175570	0.19
E2.2	2806952	0.19
E2.3	1524453	0.189
E3.1	6050096	0.204
E3.2	3272325	0.204
E3.3	1767572	0.202

Table 5.3 Drag coefficient of the meshes from the mesh independence study.

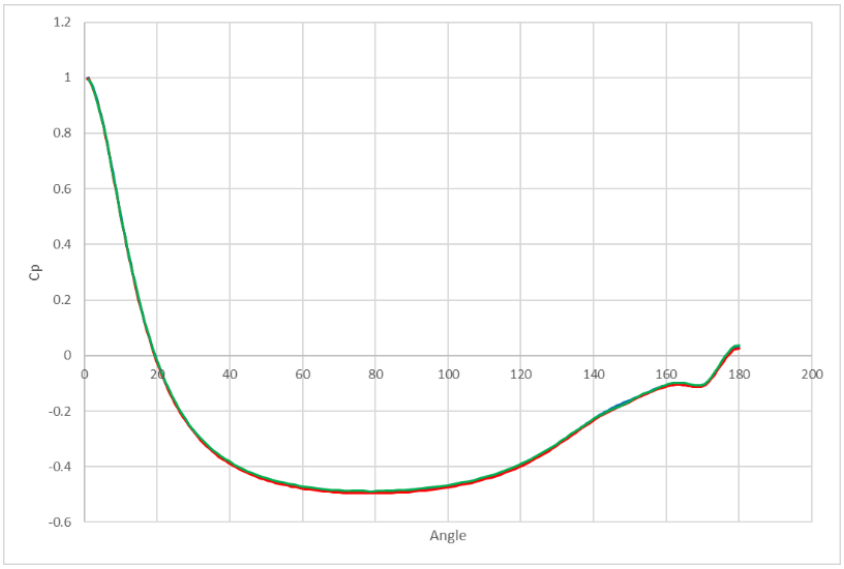

Figure 5.1 Drag coefficient comparison for the meshes E1.1, E1.2, and E1.3.

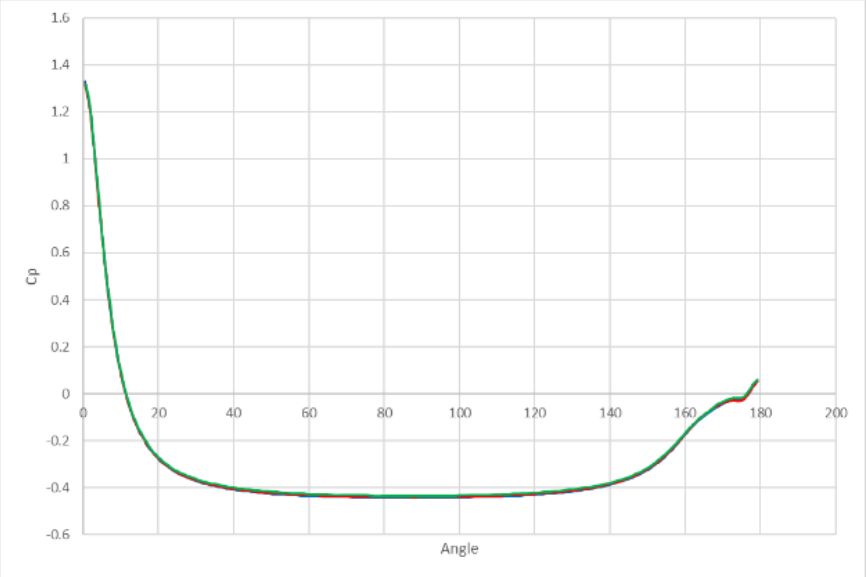

Figure 5.2 Drag coefficient comparison for the meshes E2.1, E2.2, and E2.3.

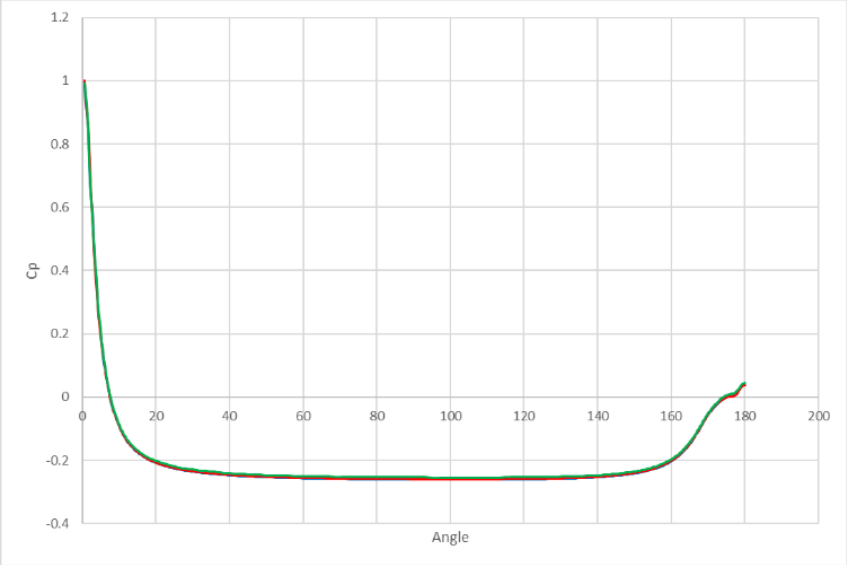

Figure 5.3 Drag coefficient comparison for the meshes E3.1, E3.2, and E3.3.

5.2.2 Mesh characteristics

The surface mesh for the selected meshes was used consistently for all vertical positions (0 m, 0.1 m, and 0.2 m) for each ellipsoid. This approach ensured that any differences in simulation outcomes would be attributed solely to changes in the robot's position relative to the pipe wall, rather than variations in mesh resolution.

To maintain consistent resolution across the different ellipsoids, the same element size, number of inflation layers, and first cell height, were used for each ellipsoid. That decision was taken because scaling the elements for the different lengths would have reduced the mesh resolution on particular areas of the ellipsoids, and potentially leading to less accurate simulation results. Therefore, the uniform element size ensured that the flow characteristics were captured with equal fidelity for all ellipsoids.

Finally, utilising the software Ansys Fluent Meshing, a hexcore mesh was automatically generated for each configuration, ensuring that the mesh quality metrics, such as skewness and orthogonality, remained within acceptable ranges.

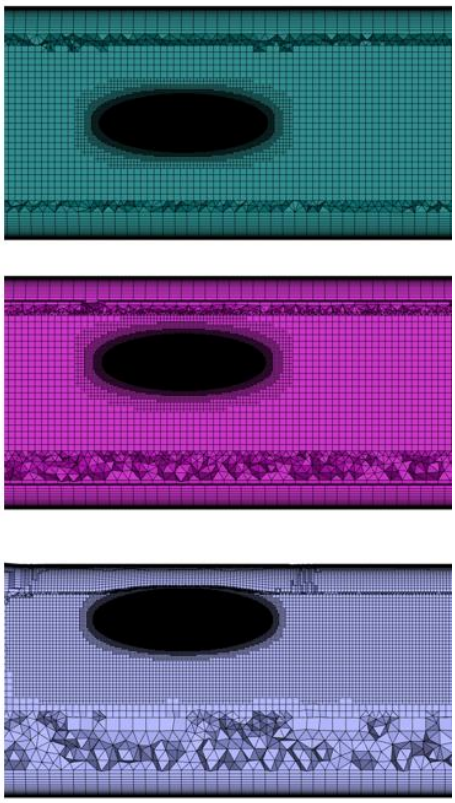

Figure 5.4 Meshes for L = 0.6m.

5.3 Boundary conditions, fluid properties, and solver settings

The boundary conditions and fluid properties for this study were set to be consistent with those used in the previous CFD analysis. This has two advantages: (1) ensures comparability of the results with the previous study; and (2) ensures that the differences in results are caused by the modified geometries and their positions within the pipe.

As in the previous study, a uniform velocity inlet condition of 1 m/s was applied at the pipe's entrance, and the outlet boundary condition was set to a pressure of 0 Pa, simulating an open-ended pipe. Then, a symmetry boundary condition was applied along the plane that cuts the pipe longitudinally. Finally, a no-slip boundary condition was imposed on the pipe walls and sphere/ellipsoid surface, ensuring that the fluid velocity at the wall surfaces was zero.

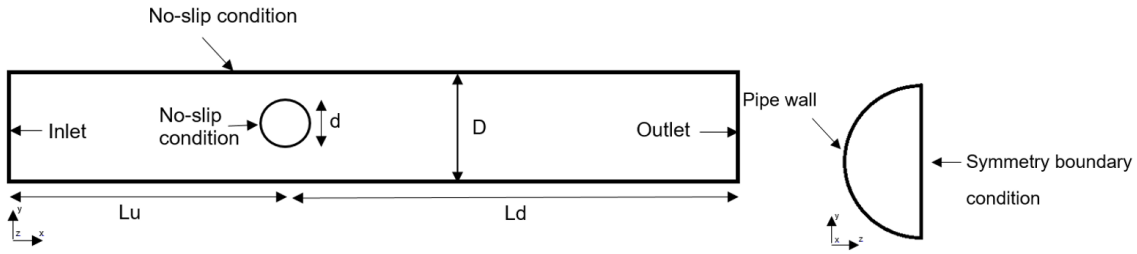

Figure 5.5 Diagram of the geometry.

For this study, only one fluid viscosity was used, corresponding to the fourth viscosity (μ4 = 0.011005 Pa·s) from the studies done in the previous chapter. This viscosity was selected as it roughly represents a median value among the previously tested viscosities, making it the most representative for the analysis. By using this intermediate viscosity, the study aims to provide insights that are broadly applicable across a range of fluid environments without the extremes of low or high viscosity dominating the results. Additionally, the same density used across all simulations in the previous chapter was also used for all the simulations in this study.

Boundary condition / properties	Details
Solver	Steady-state
Viscous model	K-ω SST
Inlet (velocity)	1 m/s
Outlet (Pressure)	0 Pa
Walls (pipe)	No-slip boundary condition
Walls (sphere / ellipsoid)	No-slip boundary condition
Density (kg/m^3)	800
Viscosities (Pa·s)	0.011005
Pressure-Velocity coupling	SIMPLE
Discretization	Green-Gauss node based, second order for pressure, and second order upwind for momentum.

Table 5.4 List of boundary conditions and solver settings.

5.4 Analysis

The Computational Fluid Dynamics simulations conducted in this study had the purpose of providing insights into how the robot's elongation and vertical position within the pipe could influence flow characteristics such as the drag, lift, and pressure distribution. This analysis examines these effects in detail, focusing on the relationships between the robot's length, its proximity to the pipe wall, and the resulting fluid dynamics.

5.4.1 Effects of the length

The elongation of the robot from a sphere to three different ellipsoidal shapes had a significant impact on the drag force experienced by the robot. As shown in figure 5.6, for the three tested vertical positions the C_d was reduced after modifying the sphere to a more streamlined shape. The major decrease in C_d

was from a length of 0.2 m (sphere) to 0.4 m, where there was a decrement of 61% (see table 5.5). Then, from a length of 0.4 m to 0.6 m was a decrement of 11.9%. Interestingly, the simulations predicted that going from a length of 0.6 m to 0.8 m increased the C_d in a 7.2%.

Length (m)	Vertical position (m)	C_d
0.2	0	0.555
0.4	0	0.216
0.6	0	0.19
0.8	0	0.204
0.2	0.1	0.55
0.4	0.1	0.218
0.6	0.1	0.193
0.8	0.1	0.206
0.2	0.2	0.521
0.4	0.2	0.237
0.6	0.2	0.209
0.8	0.2	0.219

Table 5.5 Drag coefficient per length and vertical position.

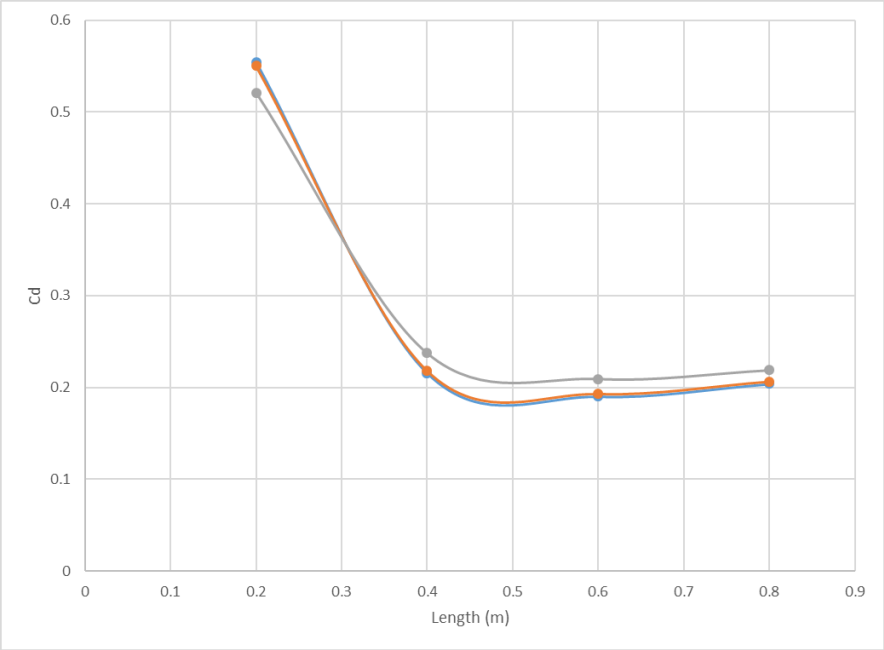

Figure 5.6 Effects of the robot's length in the drag coefficient [blue line: centre of the pipe; orange line: offset of 0.1 m; grey line: offset of 0.2 m].

The reduction in the drag force could be attributed to the more streamlined shape of the ellipsoids, which, promotes a delay flow separation, thereby reducing the size of the wake region behind the robot. As can be observed in figure 5.7, the spherical shape produces the earliest flow separation resulting in the largest wake. An increment from 0.2 m to 0.4 m has the major decrease in the wake size. Then, increasing the length from of 0.4 m to 0.6 m, and 0.6 m to 0.8 m, have a smaller but still noticeable effect on the wake size.

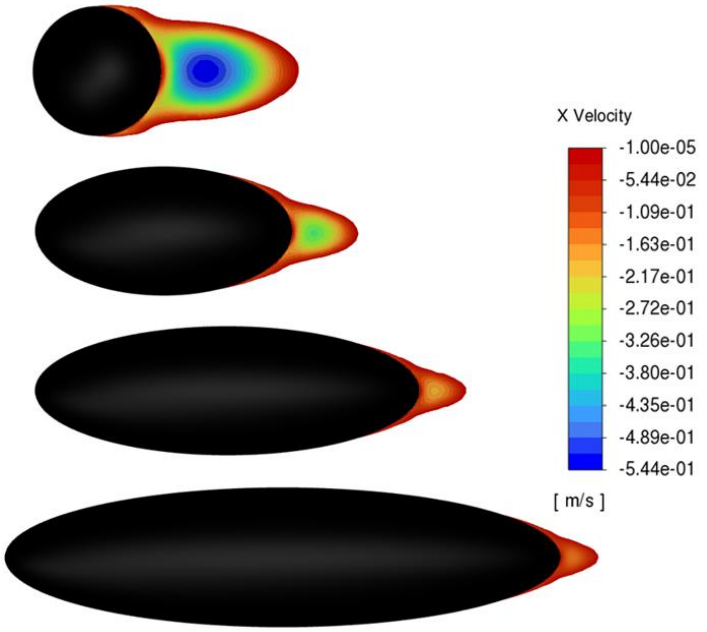

Figure 5.7 Effects of the robot's length in the recirculation region.

As for the lift coefficient (C_l), it shows to be affected by the increment in length at across all vertical positions. When the robot is place in the centre of the pipe, the sphere shows a C_l close to 0, but increasing the length to 0.4 m produces an increment in the C_l of the 12177%. Conversely, for the same vertical position of 0 m, the lengths to 0.6 m and 0.8 m show C_l close to 0. A similar pattern is observed for the remaining vertical positions. However, it is important to notice that, the C_l values predicted by the simulations are considerably small and negligible in most cases.

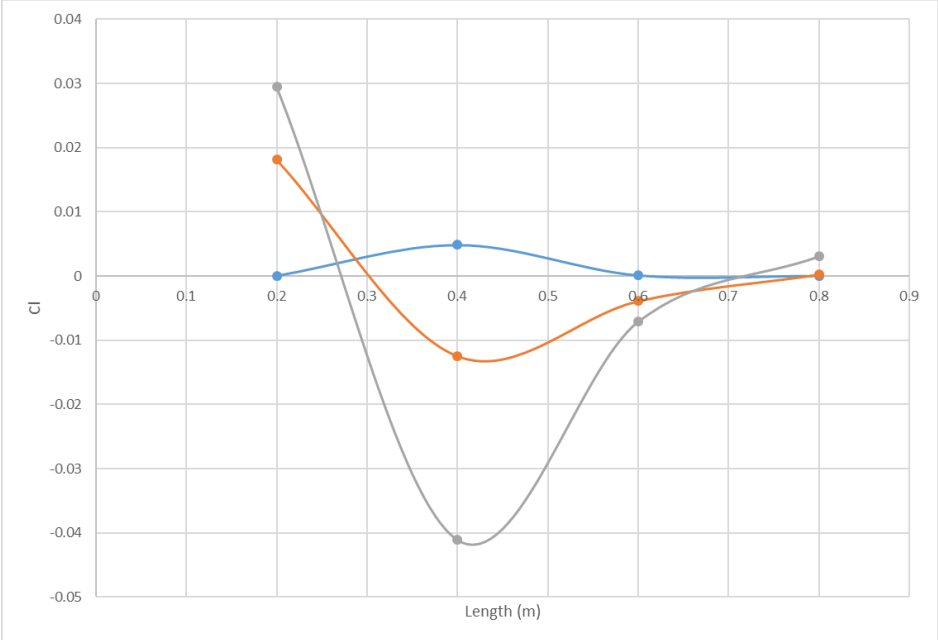

Figure 5.8 Effects of the robot's length in the lift coefficient. [blue line: centre of the pipe; orange line: offset of 0.1 m; grey line: offset of 0.2 m].

Length (m)	Vertical position (m)	Cl
0.2	0	3.997×10^{-5}
0.4	0	4.867×10^{-3}
0.6	0	1.031×10^{-4}
0.8	0	1.985×10^{-5}
0.2	0.1	0.018
0.4	0.1	-0.012
0.6	0.1	-0.003
0.8	0.1	2.191×10^{-4}
0.2	0.2	0.029
0.4	0.2	-0.041
0.6	0.2	-0.007
0.8	0.2	0.003

Table 5.6 Lift coefficient per length and vertical position.

Figures 5.9, 5.10, and 5.11 show how the pressure distribution from the top face of the sphere/ellipsoid is affected by the increment in length at different heights. The pressure distribution around the ellipsoids is shown to be more uniform compared to the spherical shape. Moreover, this effect is increases with the increment of the length. For the length of 0.8 m, the pressure drop remains almost constant along the length of the robot. Conversely, the spherical shape presents a considerably sharper pressure drop.

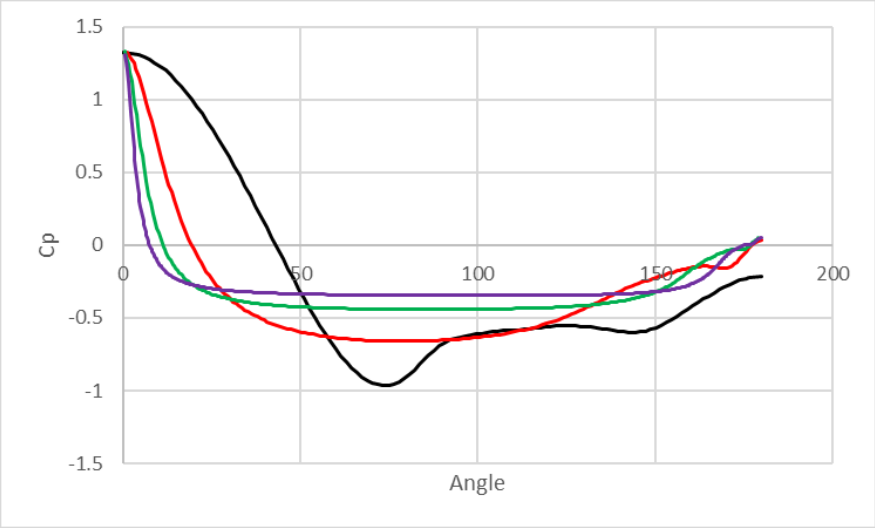

Figure 5.9 Effects of the length in the pressure distribution at the centre of the pipe [black line: sphere; orange line: length of 0.4 m; green line: length of 0.6 m; purple line: length of 0.8 m].

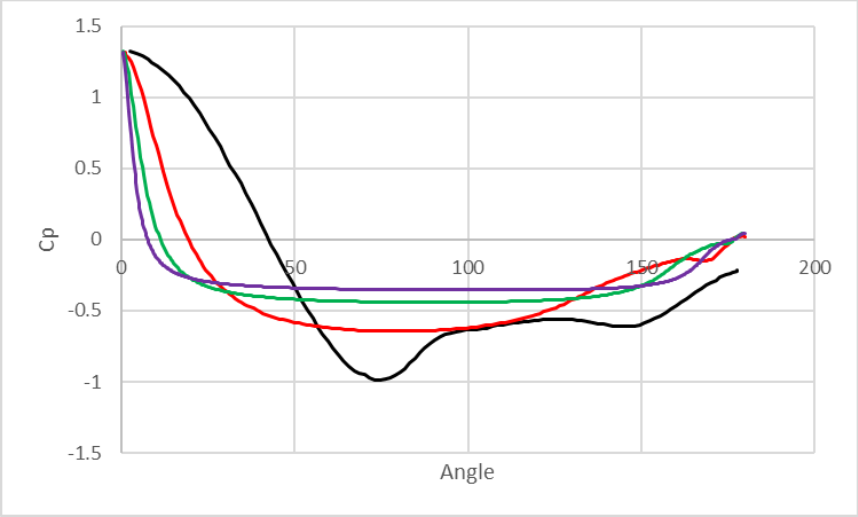

Figure 5.10 Effects of the length in the pressure distribution with an offset of 0.1 m [black line: sphere; orange line: length of 0.4 m; green line: length of 0.6 m; purple line: length of 0.8 m].

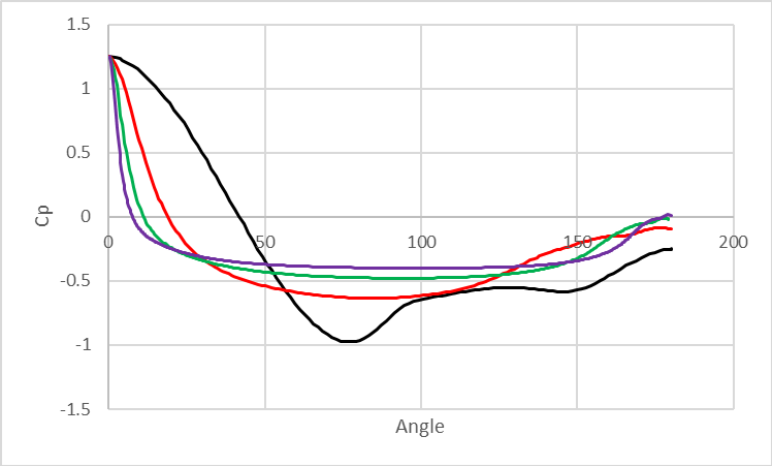

Figure 5.11 Effects of the length in the pressure distribution with an offset of 0.2 m [black line: sphere; orange line: length of 0.4 m; green line: length of 0.6 m; purple line: length of 0.8 m].

5.4.2 Effects of the vertical position

The vertical position of the robot within the pipe also plays a crucial role in determining the drag and lift forces. It is expected that moving the robot closer to the pipe wall would alter the symmetry of the flow, leading to significant changes in these forces, specially the C_l.

Figure 5.12 shows the effect the vertical position has on the sphere/ellipsoids. The vertical position produces a small increment in the C_d of the ellipsoids with the major one being at a height of 0.2 m. However, the increment in height seems to have the opposite effect on the sphere, which showed a decrease of the C_d.

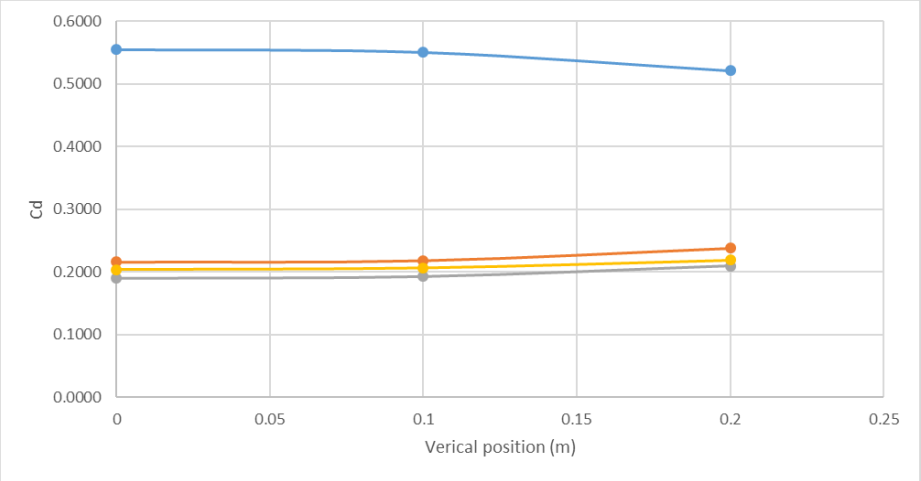

Figure 5.12 Effects of the vertical position in the drag coefficient [blue line: sphere; orange line: length of 0.4 m; grey line: length of 0.6 m; yellow line: length of 0.8 m].

When the robot was positioned at the centre of the pipe, the flow was symmetric around it, and this produced a balanced lift force. However, once the robot moves upwards, this symmetry is broken resulting in a slight increase in lift force, pushing the robot away from the wall in the case of the lengths 0.4 m and 0.6 m, and against the wall in the case of the 0.2 m and 0.8 m.

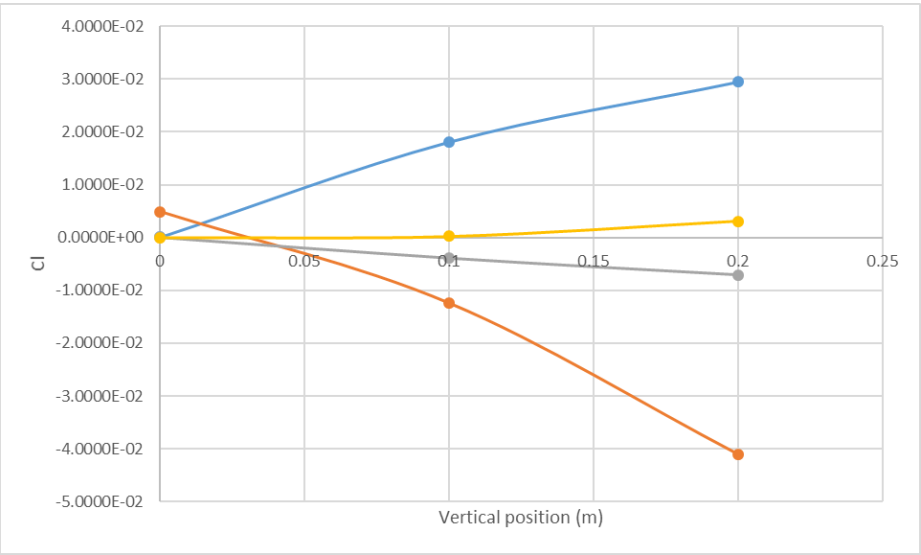

Figure 5.13 Effects of the vertical position in the lift coefficient [blue line: sphere; orange line: length of 0.4 m; grey line: length of 0.6 m; yellow line: length of 0.8 m].

The figures from 5.14 to 5.17 show the pressure distribution of the top and bottom faces across all the robot lengths when the vertical position is modified. It can be seen that the change in height does not seems to have noticeable effects on the pressure distribution for most heights. Only the vertical positon of 0.2 m seems to have a minor effect on the top side of the sphere/ellipsoid.

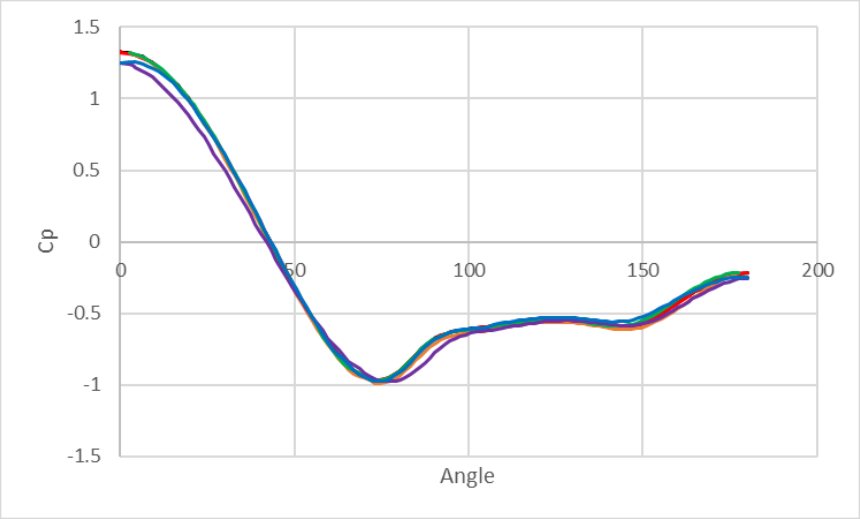

Figure 5.14 Effects of the vertical position on the pressure distribution for the sphere [black line: centre of the pipe, upper face; red line: centre of the pipe, lower face; orange line: height of 0.1 m, upper face; green line: height of 0.1 m, lower face; purple line: height of 0.2 m, upper face; blue line: height of 0.2 m, lower face].

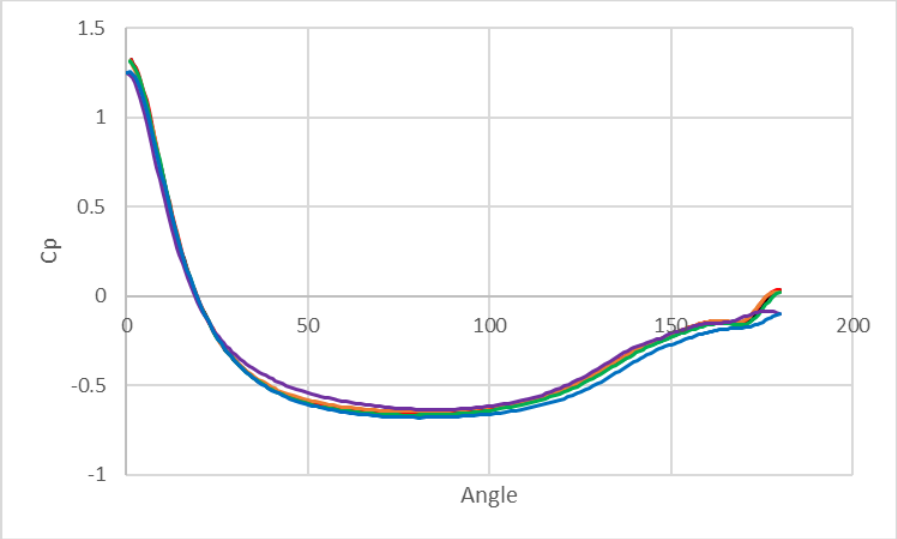

Figure 5.15 Effects of the vertical position on the pressure distribution for a body length of 0.4 m Effects of the vertical position on the pressure distribution for the sphere [black line: centre of the pipe, upper face; red line: centre of the pipe, lower face; orange line: height of 0.1 m, upper face; green line: height of 0.1 m, lower face; purple line: height of 0.2 m, upper face; blue line: height of 0.2 m, lower face].

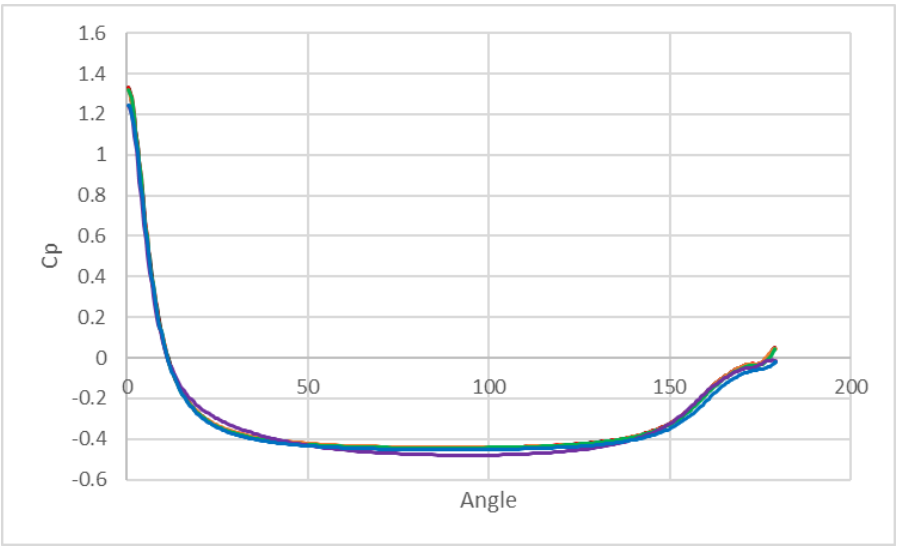

Figure 5.16 Effects of the vertical position on the pressure distribution for a body length of 0.6 m Effects of the vertical position on the pressure distribution for the sphere [black line: centre of the pipe, upper face; red line: centre of the pipe, lower face; orange line: height of 0.1 m, upper face; green line: height of 0.1 m, lower face; purple line: height of 0.2 m, upper face; blue line: height of 0.2 m, lower face].

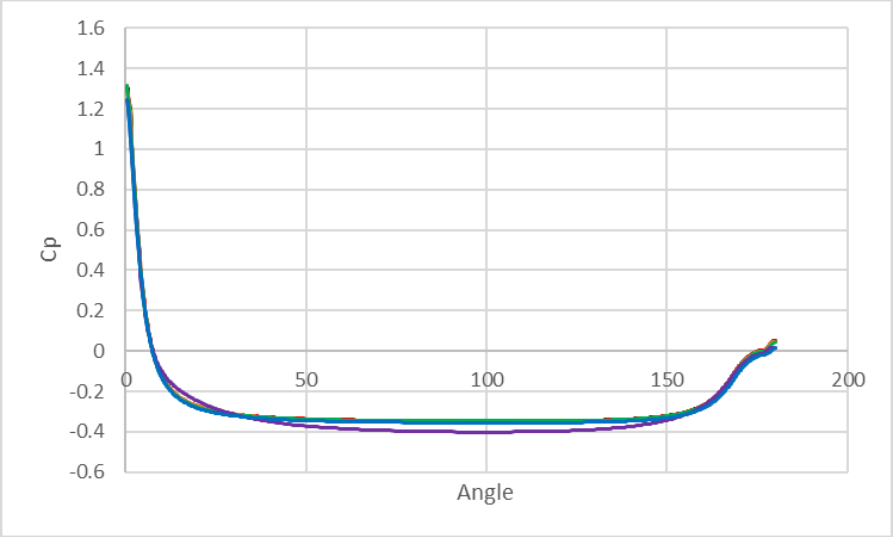

Figure 5.17 Effects of the vertical position on the pressure distribution for a body length of 0.8 m Effects of the vertical position on the pressure distribution for the sphere [black line: centre of the pipe, upper face; red line: centre of the pipe, lower face; orange line: height of 0.1 m, upper face; green line: height of 0.1 m, lower face; purple line: height of 0.2 m, upper face; blue line: height of 0.2 m, lower face].

5.5 Discussion and conclusion

This chapter aimed to expand upon the CFD analysis done in Chapter 4 by investigating the effects of robot geometry and positioning within a pipe, focusing on drag, lift, and pressure distribution. By elongating the spherical robot to create three distinct ellipsoidal shapes and examining their performance at various vertical positions within the pipe.

For this study, a 0.762 m diameter pipe and a single representative viscosity of 0.011005 Pa·s were selected. These values were representative of the intermediate conditions from the previous study. The spherical robot was elongated into three ellipsoidal shapes 0.4 m, 0.6 m, and 0.8 m. These three shapes, together with the initial sphere, were analysed at three different vertical positions within the pipe: 0 m (centred), 0.1 m above the centre, and 0.2 m above the centre.

The CFD simulations revealed that elongating the robot into an ellipsoidal shape significantly reduced the drag force, with the ellipsoid with a length of

0.6 m achieving the greatest reduction. This improvement in drag could be attributed to the minimized flow separation and reduction of the wake size.

The change of the vertical position within the pipe introduced additional complexity. When the robot was moved closer to the pipe wall, the flow symmetry was disrupted, leading to a minor increase in drag for the ellipsoids and an equally minor decrease for the sphere. Additionally, the change of the vertical position caused the apparition of lift forces that pushed away from the wall the ellipsoids with lengths 0.4 m and 0.6 m. Conversely, the sphere and the ellipsoid with a length of 0.8 m were pushed against the wall.

In conclusion, this study demonstrates that elongating the robot into an ellipsoidal shape offers considerable advantages in terms of drag reduction. Thus, reducing the required thrust for the robot to navigate inside the pipeline and improving its efficiency. However, the introduction of lift forces when the robot is positioned off-centre show the importance of taking into account the positioning and stabilization during the design process.

Chapter 6 Discussion and conclusion

6.1 Scope

The main objective of this MPhil was to understand the characteristics a robot should have to propel itself inside oil pipelines to carry out non-destructive inspection. Thus, this project was interested on the fluid dynamics involved in such situation, and the effects these would have on the design requirements for the robot. In particular, for the locomotion method. Since, as explained in Chapter 2, currently the main method to inspect the integrity of oil pipelines is through Pipeline Inspection Gauges (PIGs). Although, there is plenty of research and development for other types of robots to carry out such inspections, to the author's knowledge, there are no major studies done that investigate the possibility of designing a robot that navigates through oil pipelines without relying on the walls. Of course, in order to design such robot, the first step is to understand the environment it is ought to navigate through. Therefore, the purpose of this thesis was conduct a series of Computational Fluid Dynamics (CFD) simulations to understand the flow around a robot inside a pipe, and observe the effects this has on the forces acting on the robot. The following subchapters explore some of the major findings of this project.

6.2 Verification and validation

The purpose of the chapter was to test a range of Computational Fluid Dynamics methods in order to find the most suitable boundary conditions and settings for future chapters. Focusing on developing a methodology capable of predicting the drag coefficient and pressure distribution with an acceptable level of accuracy.

Validation study 1 utilised CFD simulations to replicate the results obtained in the experimental work conducted in [58]. Although such experiments were not

carried out inside a pipeline, this was an important step in order to connect future simulations with experimental data. Then, Validation study 2 replicated the validation study carried out in [59], where a sphere was simulated inside a pipe with a uniform flow and slip condition on the pie wall. Finally, utilising an identical geometry than Validation study 2, Validation study 3 aimed to connect the previous two validations cases with the simulations that would be conducted in later chapters. This was done by utilising a no-slip boundary condition on the pipe wall to observe the interaction between the pipe boundary layer and the flow around the sphere.

The three validation studies predicted values of C_d marginally higher than the referenced data. The suspected reason for that discrepancy is the mesh design. The numerical studies conducted in [59] were done with a fully structured mesh. On the other hand, the simulations done during the validation studies had regions where the mesh was unstructured. One of these regions surrounded the sphere. Thus, it may have affected the precision of the results.

Moreover, the blockage ratio in the Validation case 3 could have been too small to have an effect. Hence why the results showed a great agreement with the previous validation studies. Because the boundary layer of the pipe was not interacting with the sphere. Additionally, because study 3 was a direct continuation of study 2, it was conducted with the same geometry. This meant that, at the moment of applying a no-slip condition, the pipe did not have the length to allow the flow to fully develop.

6.3 Influence of the pipe diameter and viscosity

This chapter presented an analysis of the fluid dynamics around a sphere inside several pipes of varying diameters and fluid viscosities. The simulations demonstrated that the diameter of the pipe and the fluid viscosity have a significant influence on the drag force and pressure distribution.

When the pipe diameter decreases, there is an increment in the drag forces. This is caused by the reduction of the cross sectional area around the sphere. Therefore, the fluid around accelerates, which causes steeper pressure gradients around the sphere. Furthermore, this study also showed how the

viscosity affects the drag force. It was found that an increment of the viscosity leads to an increase in the pressure and viscous drag.

6.4 Influence of the robot's geometry and proximity to the walls

Chapter 5 investigated the effects of modifying the robot's geometry and position within a pipe. The spherical robot was elongated into three ellipsoidal shapes of 0.4 m, 0.6 m, and 0.8 m. The flow around these ellipsoids and sphere was analysed at three different vertical positions within the pipe: 0 m (centred), 0.1 m, and 0.2 m.

The results revealed that a more streamlined shape like an ellipsoid significantly reduces the drag force. However, the ellipsoid that presented the highest drag reduction was not the largest one, but the ellipsoid with a length of 0.6 m.

Furthermore, moving the robot to a position closer to the wall produced a minor increase in drag for the ellipsoids and an equally minor decrease for the sphere. Additionally, the change of the vertical position caused the ellipsoids with lengths 0.4 m and 0.6 m to be pushed away. However, it had the opposite effect on the sphere and the ellipsoid with a length of 0.8 m, which were pushed against the wall.

Chapter 7 References

1. Shukla, A. and H. Karki, *Application of robotics in offshore oil and gas industry-A review Part II.* Robotics and Autonomous Systems, 2016. **75**: p. 508-524.
2. Shukla, A. and H. Karki, *Application of robotics in onshore oil and gas industry-A review Part I.* Robotics and Autonomous Systems, 2016. **75**: p. 490-507.
3. Carvalho, A., J. Rebello, M. Souza, L. Sagrilo, and S. Soares, *Reliability of non-destructive test techniques in the inspection of pipelines used in the oil industry.* International journal of pressure vessels and piping, 2008. **85**(11): p. 745-751.
4. Kishawy, H.A. and H.A. Gabbar, *Review of pipeline integrity management practices.* International Journal of Pressure Vessels and Piping, 2010. **87**(7): p. 373-380.
5. Shi, Y., L. Hao, M. Cai, Y. Wang, J. Yao, R. Li, Q. Feng, and Y. Li, *High-precision diameter detector and three-dimensional reconstruction method for oil and gas pipelines.* Journal of Petroleum Science and Engineering, 2018. **165**: p. 842-849.
6. Canavese, G., L. Scaltrito, S. Ferrero, C. Pirri, M. Cocuzza, M. Pirola, S. Corbellini, G. Ghione, C. Ramella, and F. Verga, *A novel smart caliper foam pig for low-cost pipeline inspection—Part A: Design and laboratory characterization.* Journal of Petroleum Science and Engineering, 2015. **127**: p. 311-317.
7. International, N.A.o.E., *NACE SP0102-2010*. 2010: Houston, Texas. p. 44.
8. Jarvis, R., P. Cawley, and P. Nagy, *Current deflection NDE for the inspection and monitoring of pipes.* Ndt & E International, 2016. **81**: p. 46-59.
9. Zhang, H., S. Zhang, S. Liu, Y. Wang, and L. Lin, *Measurement and analysis of friction and dynamic characteristics of PIG's sealing disc passing through girth weld in oil and gas pipeline.* Measurement, 2015. **64**: p. 112-122.
10. Mills, G.H., A.E. Jackson, and R.C. Richardson, *Advances in the inspection of unpiggable pipelines.* Robotics, 2017. **6**(4): p. 36.
11. Shao, L., Y. Wang, B. Guo, and X. Chen. *A review over state of the art of in-pipe robot*. in *2015 IEEE International Conference on Mechatronics and Automation (ICMA)*. 2015. IEEE.
12. Shukla, A. and H. Karki. *A review of robotics in onshore oil-gas industry*. in *2013 IEEE International Conference on Mechatronics and Automation*. 2013. IEEE.
13. Ramella, C., G. Canavese, S. Corbellini, M. Pirola, M. Cocuzza, L. Scaltrito, S. Ferrero, C.F. Pirri, G. Ghione, V. Rocca, A. Tasso, and A. Di Lullo, *A novel smart caliper foam pig for low-cost pipeline inspection - Part B: Field test and data processing.* Journal of Petroleum Science and Engineering, 2015. **133**: p. 771-775.

14. Di Lullo, A., K. Hester, C. Passucci, L. Padula, and G. Biundo. *Instrumented Polly-Pigs for Low-Risk and Low-Cost Pipeline Internal Inspection: Field Experiences*. in *Offshore Mediterranean Conference and Exhibition*. 2017. Offshore Mediterranean Conference.
15. Jones, C. and R. Smith. *Cost Effective Smart Cleaning Pigs Enabling High Frequency Pipeline Inspection*. in *Offshore Technology Conference Asia*. 2018. Offshore Technology Conference.
16. Alnaimi, F.B.I., A.A. Mazraeh, K. Sahari, K. Weria, and Y. Moslem. *Design of a multi-diameter in-line cleaning and fault detection pipe pigging device*. in *2015 IEEE International Symposium on Robotics and Intelligent Sensors (IRIS)*. 2015. IEEE.
17. Bandala, A.A., J.M.Z. Maningo, A.H. Fernando, R.R.P. Vicerra, M.A.B. Antonio, J.A.I. Diaz, M. Ligeralde, and P.A.R. Mascardo. *Control and Mechanical Design of a Multi-diameter Tri-Legged In-Pipe Traversing Robot*. in *2019 IEEE/SICE International Symposium on System Integration (SII)*. 2019. IEEE.
18. Qu, Y., P. Durdevic, and Z. Yang, *Smart-spider: Autonomous self-driven in-line robot for versatile pipeline inspection.* Ifac-papersonline, 2018. **51**(8): p. 251-256.
19. Kim, H.M., Y.S. Choi, H.M. Mun, S.U. Yang, C.M. Park, and H.R. Choi. *2-2D differential gear mechanism for robot moving inside pipelines*. in *2015 IEEE/RSJ International Conference on Intelligent Robots and Systems (IROS)*. 2015. IEEE.
20. Chattopadhyay, P., S. Ghoshal, A. Majumder, and H. Dikshit, *Locomotion Methods of Pipe Climbing robots: A Review.* Journal of Engineering Science & Technology Review, 2018. **11**(4).
21. Abidin, A.S.Z., M.F.A.M. Pauzi, M.M. Sadini, M.H. Zaini, S.C. Chie, S. Mohammadan, A. Jamali, R. Muslimen, M.F. Ashari, and M.S. Jamaludin, *Development of track wheel for in-pipe robot application.* Procedia Computer Science, 2015. **76**: p. 500-505.
22. Ou, C.-W., C.-J. Chao, F.-S. Chang, S.-M. Wang, J.-N. Lee, R.-D. Hung, B. Chiu, K.-Y. Cho, and L.-T. Hwang. *Design of an adjustable pipeline inspection robot with three belt driven mechanical modules*. in *2017 IEEE International Conference on Mechatronics and Automation (ICMA)*. 2017. IEEE.
23. Minder, J. *Robotic Crawler ILI of Unpiggable 10" Natural Gas Pipeline in an Urban Area*. in *CORROSION 2018*. 2018. NACE International.
24. Roslin, N.S., A. Anuar, M.F.A. Jalal, and K.S.M. Sahari, *A review: Hybrid locomotion of in-pipe inspection robot.* Procedia Engineering, 2012. **41**: p. 1456-1462.
25. Gargade, A.A. and S.S. Ohol, *Development of Actively Steerable In-pipe Inspection Robot for Various Sizes*, in *Proceedings of the Advances in Robotics*. 2017. p. 1-5.
26. Ren, T., Y. Zhang, Y. Li, and L. Xian, *DEVELOPMENT OF AN ACTIVE HELICAL DRIVE SELF-BALANCING IN-PIPE ROBOT BASED ON COMPOUND PLANETARY GEARING.* International Journal of Robotics and Automation, 2019. **34**(3).
27. Lu, Y., J. Yu, C. Sui, and J. Han. *Design of in-pipe 3SPR/3RPS parallel manipulator and its kinestatics analysis*. in *2015 IEEE International*

Conference on Cyber Technology in Automation, Control, and Intelligent Systems (CYBER). 2015. IEEE.

28. Yu, X., Y. Chen, M.Z. Chen, and J. Lam. *Development of a novel in-pipe walking robot*. in *2015 IEEE International Conference on Information and Automation*. 2015. IEEE.
29. Koh, D.C., A.G. Dharmawan, H.H. Hariri, G.S. Soh, S. Foong, R. Bouffanais, H.Y. Low, and K.L. Wood. *Design and analysis of a miniature two-wheg climbing robot with robust internal and external transitioning capabilities*. in *2019 International Conference on Robotics and Automation (ICRA)*. 2019. IEEE.
30. Mahon, S.T., A. Buchoux, M.E. Sayed, L. Teng, and A.A. Stokes. *Soft robots for extreme environments: Removing electronic control*. in *2019 2nd IEEE International Conference on Soft Robotics (RoboSoft)*. 2019. IEEE.
31. Verma, M.S., A. Ainla, D. Yang, D. Harburg, and G.M. Whitesides, *A soft tube-climbing robot.* Soft robotics, 2018. **5**(2): p. 133-137.
32. Zhang, Z., X. Wang, S. Wang, D. Meng, and B. Liang, *Design and modeling of a parallel-pipe-crawling pneumatic soft robot.* IEEE Access, 2019. **7**: p. 134301-134317.
33. Fekrmandi, H., J. Hillard, and W. Staib. *Design of a bio-inspired crawler for autonomous pipe inspection and repair using high pressure cold spray*. in *31st florida conference on recent advances in robotics, FCRAR2018*. 2018.
34. Singh, A., E. Sachdeva, A. Sarkar, and K.M. Krishna. *COCrIP: Compliant OmniCrawler in-pipeline robot*. in *2017 IEEE/RSJ International Conference on Intelligent Robots and Systems (IROS)*. 2017. IEEE.
35. Rollinson, D. and H. Choset, *Pipe network locomotion with a snake robot.* Journal of Field Robotics, 2016. **33**(3): p. 322-336.
36. Trebuňa, F., I. Virgala, M. Pástor, T. Lipták, and Ľ. Miková, *An inspection of pipe by snake robot.* International Journal of Advanced Robotic Systems, 2016. **13**(5): p. 1729881416663668.
37. Prada, E., M. Valášek, I. Virgala, A. Gmiterko, M. Kelemen, M. Hagara, and T. Lipták. *New approach of fixation possibilities investigation for snake robot in the pipe*. in *2015 IEEE international conference on mechatronics and automation (ICMA)*. 2015. IEEE.
38. Trebuňa, F., I. Virgala, M. Kelemen, and T. Lipták, *Locomotion of snake robot through the pipe.* Journal of Automation and Control, 2015. **3**(3): p. 135-139.
39. Bando, Y., H. Suhara, M. Tanaka, T. Kamegawa, K. Itoyama, K. Yoshii, F. Matsuno, and H.G. Okuno. *Sound-based online localization for an in-pipe snake robot*. in *2016 IEEE International Symposium on Safety, Security, and Rescue Robotics (SSRR)*. 2016. IEEE.
40. Selvarajan, A., A. Kumar, D. Sethu, and M.A. bin Ramlan. *Design and Development of a Snake-Robot for Pipeline Inspection*. in *2019 IEEE Student Conference on Research and Development (SCOReD)*. 2019. IEEE.
41. Carnie, G., A. Prathuru, and X. Meng. *In-Line Robot for Asset Pipeline Inspection*. in *SPE Offshore Europe Conference and Exhibition*. 2019. Society of Petroleum Engineers.

42. Cetinsoy, E. and H. Esgin. *Design of an ex-proof untethered in-pipe inspection robot*. in *2018 IEEE International Conference on Automation, Quality and Testing, Robotics (AQTR)*. 2018. IEEE.
43. Doyle, M.J., X. Xu, Y. Gu, F. Perez-Diaz, C. Parrott, and R. Groß. *Modular hydraulic propulsion: A robot that moves by routing fluid through itself*. in *2016 IEEE International Conference on Robotics and Automation (ICRA)*. 2016. IEEE.
44. Wu, Y., A. Noel, D.D. Kim, K. Youcef-Toumi, and R. Ben-Mansour. *Design of a maneuverable swimming robot for in-pipe missions*. in *2015 IEEE/RSJ International Conference on Intelligent Robots and Systems (IROS)*. 2015. IEEE.
45. Wu, Y., D. Chatzigeorgiou, K. Youcef-Toumi, and M. Zribi. *Modeling and parameter estimation for in-pipe swimming robots*. in *2015 American Control Conference (ACC)*. 2015. IEEE.
46. Massey, B.S., *Mechanics of Fluids*. 1989: Van Nostrand Reinhold.
47. Tu, J., G.H. Yeoh, and C. Liu, *Computational Fluid Dynamics: A Practical Approach*. First ed. 2007: Elsevier Science. 480.
48. Purcell, E.M., *Life at low Reynolds number.* American journal of physics, 1977. **45**(1): p. 3-11.
49. Bente, K., A. Codutti, F. Bachmann, and D. Faivre, *Biohybrid and bioinspired magnetic microswimmers.* Small, 2018. **14**(29): p. 1704374.
50. Parker, N., *Microbiology*. Revision MB-2016-002(05/18)-BB. ed. 2016, Place of publication not identified: OpenStax CNX.
51. Jang, D., J. Jeong, H. Song, and S.K. Chung, *Targeted drug delivery technology using untethered microrobots: A review.* Journal of Micromechanics and Microengineering, 2019. **29**(5): p. 053002.
52. Elgeti, J., R.G. Winkler, and G.J.R.o.p.i.p. Gompper, *Physics of microswimmers—single particle motion and collective behavior: a review.* 2015. **78**(5): p. 056601.
53. Khalil, I.S., A. Fatih Tabak, A. Klingner, and M. Sitti, *Magnetic propulsion of robotic sperms at low-Reynolds number.* Applied Physics Letters, 2016. **109**(3): p. 033701.
54. Mahdy, D., A. Mohamed, A. Klingner, A. Tammam, A. Wahdan, M. Serry, and I.S. Khalil. *Experimental characterization of helical propulsion in Newtonian and viscoelastic mediums*. in *2017 IEEE International Conference on Manipulation, Manufacturing and Measurement on the Nanoscale (3M-NANO)*. 2017. IEEE.
55. Yuan, F., M.S. Hasan, and H. Yu. *Design and Modelling of a Micro Swimming Robot*. in *2019 International Conference on Advanced Mechatronic Systems (ICAMechS)*. 2019. IEEE.
56. Xu, T., J. Yu, C.-I. Vong, B. Wang, X. Wu, and L. Zhang, *Dynamic morphology and swimming properties of rotating miniature swimmers with soft tails.* IEEE/ASME Transactions on Mechatronics, 2019. **24**(3): p. 924-934.
57. Liao, P., L. Xing, S. Zhang, and D. Sun, *Magnetically driven undulatory microswimmers integrating multiple rigid segments.* Small, 2019. **15**(36): p. 1901197.
58. Wu, J.-S. and G.M.J.A.j. Faeth, *Sphere wakes in still surroundings at intermediate Reynolds numbers.* 1993. **31**(8): p. 1448-1455.

59. Yin, G. and M.C.J.P.o.F. Ong, *On the wake flow behind a sphere in a pipe flow at low Reynolds numbers.* 2020. **32**(10).
60. Yunus, A.C., *Fluid Mechanics: Fundamentals And Applications (Si Units)*. 2010: Tata McGraw Hill Education Private Limited.
61. Krishnan, S. and A.J.E.A.o.C.F.M. Kaman, *Effect of blockage ratio on drag and heat transfer from a centrally located sphere in pipe flow.* 2010. **4**(3): p. 396-414.
62. Muñoz, J.A., J. Ancheyta, L.C.J.E. Castañeda, and Fuels, *Required viscosity values to ensure proper transportation of crude oil by pipeline.* 2016. **30**(11): p. 8850-8854.